

**FACULTY
OF MATHEMATICS
AND PHYSICS**
Charles University

DOCTORAL THESIS

Michal Vraštil

**Study of dark energy and modified
gravity and their influence
on the cosmological parameters
of the universe**

Institute of Physics of the Czech Academy of Sciences

Supervisor of the doctoral thesis: RNDr. Michael Prouza, Ph.D.

Study programme: Theoretical Physics, Astronomy
and Astrophysics

Prague 2020

I declare that I carried out this doctoral thesis independently, and only with the cited sources, literature and other professional sources.

I understand that my work relates to the rights and obligations under the Act No. 121/2000 Sb., the Copyright Act, as amended, in particular the fact that the Charles University has the right to conclude a license agreement on the use of this work as a school work pursuant to Section 60 subsection 1 of the Copyright Act.

In Prague 17.8.2020

.....

I would like to thank my supervisor Michael Prouza for his support during my whole studies. My thanks belong to many great people in the Argonne National Laboratory who helped me made this project possible and my visits there wonderful. In particular, I would like to mention Salman Habib who stood at the beginning of our project and who introduced me to the exciting field of the chameleon gravity. And last but not least I would like to thank my wife, family and friends for their support during the time of the writing.

Title: Study of dark energy and modified gravity and their influence on the cosmological parameters of the universe

Author: Michal Vraštil

Institute: Institute of Physics of the Czech Academy of Sciences

Supervisor: RNDr. Michael Prouza, Ph.D., Institute of Physics of the Czech Academy of Sciences

Abstract: Discovery of the accelerated expansion of the Universe poses a major theoretical puzzle. Although the assumption of a non-zero cosmological constant provides a minimal extension of general relativity that is consistent with observational data, many theories of modified gravity have been suggested as possible alternatives due to the serious problem connected with the cosmological constant. Numerical predictions of structure formation for these models in the fully non-linear regime are very expensive and it is difficult, if not impossible, to explore such a huge space of models and parameters using high-resolution N -body simulations. Even in the mildly nonlinear regime, perturbative methods can become extremely complex. We explore whether simplified dynamical approximations, applicable for a certain set of cosmological probes, can be used to investigate models of modified gravity with acceptable accuracy in the latter instance. For the case of chameleon gravity, we found that it is screened away on scales smaller than that of galaxy clusters. On large cosmological scales, we found that approximate methods can be used to explore the region around the baryon acoustic oscillation scale, $k \sim 0.1 \text{ hMpc}^{-1}$ but not much further.

Keywords: dark energy, modified gravity, N -body simulations, cosmology, approximate methods

Contents

List of Symbols

Symbol	Definition
G	gravitational constant; $G = 6.67 \times 10^{-11} \text{m}^{-3}\text{kg}^{-1}\text{s}^{-2}$
M_{pl}	reduced Planck mass; $M_{\text{pl}} \equiv \sqrt{\hbar c/8\pi G} = 2.4357 \times 10^{18} \text{ GeV}$
$g_{\mu\nu}$	metric tensor
a	cosmic scale factor
t	cosmic time
η	conformal time
z	redshift
D	growth function
Λ	cosmological constant
H	Hubble parameter; H_0 denotes Hubble constant (present value)
\mathcal{H}	conformal Hubble quantity
h	Hubble constant; $H_0 \equiv 100h \text{ km s}^{-1}\text{Mpc}^{-1}$
ρ	energy-density
p	pressure
w	equation of state parameter
Ω_b	baryon density parameter
Ω_m	matter density parameter
Ω_γ	radiation density parameter
Ω_Λ	cosmological constant density
Ω_{tot}	total density parameter
n_s	scalar spectral index
σ_8	matter fluctuation amplitude at $8h^{-1}\text{Mpc}$
ϕ_G	gravitational potential
χ	chameleon field (potential)
$P(k)$	matter power spectrum
$\xi(r)$	two-point correlation function

Introduction

Since the twentieth century, astronomers have accumulated conclusive evidence that the content of the Universe is mostly of unknown origin and that the ordinary matter, baryonic matter, constitutes a tiny fraction of the energy density of the Universe – only 5%. The remaining bulk of the Universe is composed of 70% of dark energy causing the accelerated expansion of the Universe, whereas 25% is in a form of a dark matter causing the formation of the structures in the Universe. Dark energy ~~ranks as is~~ one of the most important discoveries in cosmology, with ~~profound major~~ implications for astronomy and fundamental physics.

With the measurement of an accelerated rate of expansion of the Universe, various alternatives to standard Einstein’s theory of gravity have been suggested to explain the acceleration, attempting to bypass problems connected to the cosmological constant. These theories usually add some new degrees of freedom, either in a form of new fields or by modifying existing fields.

There are many different ways how to study the dark energy (or modified gravity), e.g. through a growth of structures on large scales and consequent formation of cluster and galaxies on smaller scales, bending of light in the Universe, or baryonic oscillations in the early Universe.

Predictions of structure formation and other observables cannot be obtained analytically even for the standard theory of gravity, let alone for highly non-linear equations of modified gravity. One must employ numerical methods such as N -body simulations or perturbative methods. What is possible to study numerically in the fully non-linear regime for standard gravity can be very expensive for modified gravity, and it is difficult, if not impossible, to explore such a huge space of models and parameters using high-resolution N -body simulations. Even in the mildly non-linear regime, perturbative methods can become extremely complex.

Due to the numerical difficulties connected with highly non-linear equations of modified gravities, one must often look for new ways how to address these problems. We explore whether simplified dynamical approximations, applicable for a certain set of cosmological probes, can be used to investigate models of modified gravity with acceptable accuracy in the latter instance.

For our purposes, from many different models of modified gravity, we chose to explore and test these simplified methods on the Hu-Sawicki $f(R)$ model. $f(R)$ gravity represents a broad class of theories. It can be considered as the simplest example of an extended theory of gravity. $f(R)$ gravity can be also studied from a different point of view than a modification of gravity. We can see this extra degree of freedom as a new scalar field, chameleon field, with strong non-standard gravitation coupling to other fields. The chameleon field has a mass-dependent on surrounding density and can, therefore, escape standard Solar system tests through this so-called chameleon mechanism. We will study this mechanism on galaxy scales, cluster scales, and mainly on large cosmological scales.

All theoretical predictions which can be obtained analytically or numerically through simulations need to verify by real-life experiments. Present-day experiments such as DES, BOSS, or Planck place constraints on modified gravities

and so far no extension of Einstein’s gravity has been confirmed but many alternatives remain viable. But a new era of next-generation experiments is coming in the next decade, such as the Vera C. Rubin Observatory, Euclid, or W-FIRST.

The ~~Vera C. Rubin Observatory, previously referred to as the Large Synoptic Survey Telescope (LSST), is a ground-based telescope being built in northern Chile. Thanks to a large aperture, wide-field survey telescope, and 3200 Megapixel camera it will image faint astronomical objects across the sky. The LSST will rapidly scan the sky, charting objects that change or move: from exploding supernovae to potentially hazardous near-Earth asteroids. The LSST will produce a very deep survey and its images will trace billions of remote galaxies, providing multiple probes of the dark matter and dark energy.~~

~~The~~-thesis is organized as follows: in chapter 1 we review basics of the evolution of the Universe; in chapter 2 we describe various theories of dark energy and modified gravity while focusing on the chameleon theory. We study the non-linear behavior of the chameleon field numerically in systems exhibiting spherical symmetry in section 2.3, which is something not studied previously. In chapter 3 we describe different techniques when dealing with large cosmological simulations, how we adapted them in our own code for N -body simulations, and our contributions to a publicly available software CCL which compute basic cosmological observables. In chapter 4 we introduce different approximations, those we use in our simulations, and also approximations that are used by other codes or have been studied in the past. Unlike previously studied cases of Einstein-de Sitter universes we adapted these approximations to general Λ CDM cosmologies. In chapter 5 we describe original results of our cosmological N -body simulations using approximate schemes. In this chapter, we also study the chameleon gravity behavior on cosmological scales. In ~~we review present-day and future experiments designed to study our Universe. In~~ the end, in ?? we discuss possible future applications of implemented techniques and ways to further improve them.

Units and conventions

Throughout this work, we use units such that $c = \hbar = k_B = 1$, where c is the speed of light, \hbar is reduced Planck’s constant, and k_B is Boltzmann’s constant. We list frequently used symbols after the Table of Contents. We adopt the metric signature $(-, +, +, +)$. The Greek indices such as μ and ν run from 0 to 3 whereas the Latin indices such as i and j run from 1 to 3. When referring to present values of quantities we use subscript 0, e.g. H_0 to denote the present value of the Hubble parameter.

1. Cosmological Evolution

In this chapter we briefly describe the evolution of the Universe. For more comprehensive lectures see e.g. [Ref:Weinberg, 2002col.luc..cosmology](#) or [2010deto.book.....A](#). We begin with basic equations for the evolution and apply them to cosmological scales. We describe background evolution and formation of structures in the Λ CDM model and we briefly mention non-linear cosmological perturbations. At the end of the chapter, we introduce some basic cosmological observables that are often used to put observational constraints on dark energy.

1.1 Background evolution

The standard cosmological model is based on the *cosmological principle*, first clearly formulated in [1687pnpm.book.....N](#). The cosmological principle states that the Universe is homogeneous and isotropic on sufficiently large scales (~~beyond those traced by the large-scale structure of the distribution of galaxies~~). The cosmic microwave background (CMB) observations strongly support this statement as photons from different parts of the Universe are coming with almost identical temperatures. ~~This isotropy, however, However, the isotropy~~ does not imply homogeneity. The *Copernican Principle* states that the observer is not in a special place or time. With the observed isotropy, the Copernican Principle implies the Cosmological Principle. The observed inhomogeneities and irregularities on local scales come from gravitational instability and do not violate these principles.

1.1.1 Friedmann equations

The homogeneous and isotropic space-time is described by the Friedmann-Lemaître-Robertson-Walker (FLRW) metric given by

$$ds^2 = g_{\mu\nu}dx^\mu dx^\nu = -dt^2 + a^2(t) \left[\frac{dr^2}{1-Kr^2} + r^2(d\theta^2 + \sin^2\theta d\phi^2) \right], \quad (1.1)$$

where $g_{\mu\nu}$ is a metric tensor, $a(t)$ is a scale factor with cosmic time t and $K = +1, -1, 0$ is a curvature that corresponds to closed, open, and flat geometries. The scale factor can be arbitrarily rescaled and we adopt the common normalization $a_0 = 1$. We can also transform metric (1.1) to a more convenient form by setting $r = \sin \chi$ ($K = +1$), $r = \chi$ ($K = 0$), and $r = \sinh \chi$ ($K = -1$). The FLRW metric is then given by

$$ds^2 = -dt^2 + a^2(t) [d\chi^2 + f_K^2(\chi) (d\theta^2 + \sin^2\theta d\phi^2)], \quad (1.2)$$

where

$$f_K(\chi) = \begin{cases} \sin \chi & (K = +1), \\ \chi & (K = 0), \\ \sinh \chi & (K = -1). \end{cases} \quad (1.3)$$

By allowing taking the limit $K \rightarrow 0$ we can rewrite $f_K(\chi)$ in a unified way

$$f_K(\chi) = \frac{1}{\sqrt{-K}} \sinh(\sqrt{-K}\chi). \quad (1.4)$$

In addition to the cosmic time t , we also introduce the work, we use also the conformal time η defined by as

$$\eta \equiv \int a^{-1} dt. \quad (1.5)$$

The dynamical From the Einstein equations of motion in the expanding Universe can be derived from the Einstein equations resulting in one can derive the Friedmann equations

$$H^2 = \frac{8\pi G}{3}\rho - \frac{K}{a^2} + \frac{\Lambda}{3}, \quad (1.6)$$

$$\ddot{a} = -\frac{4\pi G}{3}(\rho + 3p) + \frac{\Lambda}{3}, \quad (1.7)$$

$$\dot{\rho} = -3H(\rho + p), \quad (1.8)$$

where the overdot denotes a time derivative with respect to t , $H \equiv \dot{a}/a$ is the Hubble parameter, Λ the cosmological constant (more details in subsection 2.1.1), $\rho(t)$ is energy-density and p pressure. We will be also using the conformal Hubble quantity

$$\mathcal{H} \equiv \frac{1}{a} \frac{da}{d\eta} = Ha. \quad (1.9)$$

These three equations are not independent and we need to also specify the equation of state, $\rho = \rho(p, t)$. The first equation is usually also written in the form

$$\Omega_m + \Omega_\gamma + \Omega_K + \Omega_\Lambda = 1, \quad (1.10)$$

where

$$\Omega_m \equiv \frac{8\pi G \rho_m}{3H^2}, \quad \Omega_\gamma \equiv \frac{8\pi G \rho_\gamma}{3H^2}, \quad \Omega_K \equiv -\frac{K}{a^2 H^2}, \quad \Omega_\Lambda \equiv \frac{\Lambda}{3H^2} \quad (1.11)$$

Most matter species in the Universe can be described by a simple equation of state

$$p = w\rho, \quad (1.12)$$

where w is constant. This lead to the following solutions in a flat universe

$$\rho \propto a^{-3(1+w)}, \quad a \propto (t - t_i)^{2/(3(1+w))}, \quad (1.13)$$

where t_i is an integration constant. The relativistic matter has the equation of state $w = 1/3$ and the cosmic evolution during the radiation-dominated epoch is given by $\rho \propto a^{-4}$ and $a \propto (t - t_i)^{1/2}$. The non-relativistic matter has negligible pressure ($w = 0$) and the evolution during the matter-dominated era is given by $\rho \propto a^{-3}$ and $a \propto (t - t_i)^{2/3}$.

The accelerated expansion of the Universe ($\ddot{a} > 0$) without the cosmological constant is possible only for $w < -1/3$ (see Friedman equation (1.7)), i.e. negative pressure. Note that in Newtonian gravity there is no such equivalent. ~~The pressure is related to a force associated with a local potential that depends on the position in space but in a homogeneous and isotropic universe there is no such potential.~~

When $w = -1$, the energy-density ρ is constant and corresponds to the cosmological constant. This energy-density connected to the cosmological constant is

$$\rho_\Lambda = \frac{\Lambda}{8\pi G}. \quad (1.14)$$

With constant energy-density, the Friedmann equations lead to an exponential expansion $a \propto \exp Ht$.

1.1.2 Hubble–Lemaître law

During the 1920s, astronomers Slipher, Hubble, and Strömgren found that the observed wavelength λ_o of absorption lines of distant galaxies is larger than the wavelength λ in the rest frame (**1925ApJ....61..353S**; **1929PNAS...15..168H**). This is because the wavelength is stretched in proportion to the scale factor in an expanding Universe. Although for many years this law was known as the Hubble’s law (renamed in 2018), Lemaître first published his research, where he derived this law, two years prior to the Hubble’s paper (**1927ASSB...47...49L**, English translation in **1931MNRAS..91..483L**).

The redshift z is defined as

$$z \equiv \frac{\lambda_o}{\lambda} - 1 = a^{-1} - 1. \quad (1.15)$$

~~In an expanding Universe, a physical~~ Physical distance r from an observer ~~(at the origin)~~ to an object in an expanding Universe is given by $r = a(t)x$, where x denotes the comoving distance. ~~For objects which are motionless~~ Objects, which are at rest with respect to the Hubble flow, ~~the comoving distance remains constant~~ have constant comoving distance. Taking the time derivative of r we obtain

$$v_H \equiv \dot{r} = Hr + a\dot{x} \quad (1.16)$$

Because of the cosmic expansion, more distant objects are moving faster from us with velocity v_H . On the other hand, the peculiar velocity $v_p \equiv a\dot{x}$ describes the movement of an object with respect to the local Hubble flow. For small peculiar velocities and near objects ($z \ll 1$), we obtain

$$v \sim H_0 r, \quad (1.17)$$

which is the law Hubble reported in 1929 by plotting the recessional velocity v versus the distance r . His measurements were noisy but the current measurements give the Hubble constant the value (**planck·cosm**)

$$H_0 = (67.4 \pm 0.5) \text{ km s}^{-1}\text{Mpc}^{-1} \quad (1.18)$$

1.2 Formation and evolution of LSS

So far we have considered only equations for a smooth, homogeneous, and isotropic background. To describe the real Universe with its rich structures, we must employ perturbation theory for cosmological equations.

1.2.1 Newtonian gauge

We will consider first-order (linear) perturbations of the metric:

$$g_{\mu\nu} = g_{\mu\nu}^{(0)} + \delta g_{\mu\nu}, \quad (1.19)$$

where $g_{\mu\nu}^{(0)}$ is the FLRW metric (1.1) and all the entries in the perturbed metric $\delta g_{\mu\nu}$ have to be small with respect to the background metric. The general perturbed metric can be written as

$$\delta g_{\mu\nu} = a^2(\eta) \begin{pmatrix} -2\Psi & w_i \\ w_i & 2\Phi\delta_{ij} + h_{ij} \end{pmatrix}, \quad (1.20)$$

where $\Psi(t, x)$ and $\Phi(t, x)$ are spatial scalars, $w_i(t, x)$ is 3-vector, and $h_{ij}(t, x)$ is a traceless 3-tensor. We have the freedom to choose coordinates in which we will describe the equations of motion – we can choose our *gauge*. We wish to keep our background metric $g_{\mu\nu}^{(0)}$ the same (i.e. FLRW) and only change $\delta g_{\mu\nu}$. Note that unlike ordinary coordinate transformations ~~a gauge transformation (although expressed as a change of coordinates) does not~~, which link different observers in the same spacetime ~~but it~~, a gauge transformation links two different spacetimes seen by the same observer. For a detailed discussion of gauge choices, see e.g. **PhysRevD.40.1804**; **10.1143/PTPS.78.1**; **PhysRevD.22.1882**.

We will choose to attach the observers to the points in the unperturbed frame, the so-called *Newtonian* or *longitudinal* or *shear-free* gauge. In this case, the observer will detect a velocity field of particles falling into the clumps of matter and will measure a gravitational potential. We can impose up to four conditions on the metric, which corresponds to the four gauge coordinate transformations. The final perturbed metric is:

$$ds^2 = a^2(\eta) \left[-(1 + 2\Psi)d\eta^2 + (1 + 2\Phi)\delta_{ij}dx^i dx^j \right]. \quad (1.21)$$

1.2.2 Linear perturbations

We now decompose the Einstein tensor and the energy-momentum tensor into the background and perturbed parts. The background cosmological evolution is obtained by solving the zeroth order Einstein equations and is given by the Friedmann equations. The first-order equations are given by the perturbation of the Einstein tensor, i.e. by perturbed metric (1.21), and by the perturbed energy-momentum tensor $T_{\mu\nu}$. The energy-momentum tensor for a single perfect fluid is given by

$$T_{\mu\nu} = (\rho + p) u_\mu u_\nu + pg_{\mu\nu}, \quad (1.22)$$

where the four-velocity u^μ is up to the first order

$$u^\mu \equiv \frac{dx^\mu}{d\tau} = \left[\frac{1}{a}(1 - \Psi), \frac{v^i}{a} \right], \quad (1.23)$$

where τ is the proper time and $v^i = dx^i/d\eta$ is the matter peculiar velocity with respect to the general expansion. We also assume that the perturbed fluid remains perfect fluid. We will use the following notation

$$\delta \equiv \frac{\delta\rho}{\bar{\rho}} \equiv \frac{\rho - \bar{\rho}}{\bar{\rho}}, \quad (1.24)$$

$$\theta \equiv \nabla \cdot v, \quad (1.25)$$

where δ is the density contrast, the bar represents a mean value (spatial average) and θ is the velocity divergence. The first-order equations are (for details see e.g. **2002col.luc..cosmology** or **10.1143/PTPS.78.1**)

$$3\mathcal{H}(\mathcal{H}\Psi - \Phi') + \nabla^2\Phi = -4\pi G\bar{\rho}a^2\delta, \quad (1.26)$$

$$\nabla^2(\Phi' - \mathcal{H}\Psi) = 4\pi G\bar{\rho}a^2(1+w)\theta, \quad (1.27)$$

$$\Psi = -\Phi, \quad (1.28)$$

$$\Phi'' + 2\mathcal{H}\Phi' - \mathcal{H}\Psi - (\mathcal{H}^2 + 2\mathcal{H}')\Psi = -4\pi G\bar{\rho}a^2c_s^2\delta, \quad (1.29)$$

where the prime denotes the derivative with respect to the conformal time η . Sound velocity c_s is defined as

$$c_s^2 \equiv \frac{\delta p}{\delta\rho} = \frac{dp}{d\rho} = \frac{\dot{p}}{\dot{\rho}}, \quad (1.30)$$

where the last equality is valid only in the FLRW metric at the background level. Conservation of the energy-momentum tensor leads to the perturbed continuity equation

$$\delta' + 3\mathcal{H}(c_s^2 - w)\delta = -(1+w)(\theta + 3\Psi'), \quad (1.31)$$

which reduces for a non-relativistic matter to

$$\delta' = -\theta - 3\Phi'. \quad (1.32)$$

Another equation coming from the conservation of the energy-momentum tensor is

$$\theta' + \left[\mathcal{H}(1 - 3w) + \frac{w'}{1+w} \right] \theta = -\nabla^2 \left(\frac{c_s^2}{1+w} \delta + \Psi \right), \quad (1.33)$$

which reduces for a non-relativistic matter to

$$\theta' + \mathcal{H}\theta = -\nabla^2\Psi - \nabla^2(c_s^2\delta), \quad (1.34)$$

which is a relativistic analog of the Euler equation.

We will now transform all the equations to the Fourier space. The Fourier transformation is (up to non-relevant pre-factors)

$$f(\mathbf{x}) = \int e^{i\mathbf{k}\cdot\mathbf{x}} \hat{f}(\mathbf{k}) d^3k, \quad (1.35)$$

where \mathbf{k} is a wavenumber with modulus k and hat represents quantities in Fourier space. If there is no danger of misunderstanding we will drop the hat in the following. Since we are dealing with linear equations the different modes are not coupled and we can solve the equation for each k independently. From equations (1.26) – (1.29), (1.31), and (1.33) we will obtain the following equations in Fourier space:

$$k^2\Phi + 3\mathcal{H}(\Phi' - \mathcal{H}\Psi) = 4\pi G\bar{\rho}a^2\delta, \quad (1.36)$$

$$k^2(\Phi' - \mathcal{H}\Psi) = -4\pi G\bar{\rho}a^2(1+w)\theta, \quad (1.37)$$

$$\Psi = -\Phi, \quad (1.38)$$

$$\Phi'' + 2\mathcal{H}\Phi' - \mathcal{H}\Psi - (\mathcal{H}^2 + 2\mathcal{H}')\Psi = -4\pi G\bar{\rho}a^2c_s^2\delta, \quad (1.39)$$

$$\delta' + 3\mathcal{H}(c_s^2 - w)\delta = -(1+w)(\theta + 3\Psi'), \quad (1.40)$$

$$\theta' + \left[\mathcal{H}(1-3w) + \frac{w'}{1+w} \right] \theta = k^2 \left(\frac{c_s^2}{1+w} \delta + \Psi \right), \quad (1.41)$$

where now $\theta = i\mathbf{k} \cdot \mathbf{v}$. Note that these six equations are not independent and w and c_s^2 are arbitrary functions of time.

Super-horizon scales

In the large-scale limit $k \ll \mathcal{H}$, i.e. when the physical wavelength $\lambda_p = 2\pi a/k$ of perturbations is much larger than the Hubble radius H^{-1} , and with the barotropic fluid, i.e. when the pressure depends only on the energy density, and with the constant w , we have $c_s^2 = w$ and we can get an equation for Φ

$$\Phi'' + 3\mathcal{H}(1+c_s^2)\Phi' = 0. \quad (1.42)$$

The growing / dominant solution for $c_s^2 > -1$ is $\Phi = \text{const}$ from which follows

$$3\mathcal{H}^2\Phi = 4\pi G\bar{\rho}a^2\delta. \quad (1.43)$$

Using the Friedmann equation we get $\delta = \Phi$, i.e. δ remains constant at large scales whenever $c_s^2 = w$.

Sub-horizon scales

In the small-scale limit $k \gg \mathcal{H}$ we can get for a pressureless fluid ($w = 0$) with a small sound speed $c_s^2 \ll 1$ the Poisson equation

$$k^2\Phi = 4\pi G\bar{\rho}a^2\delta, \quad (1.44)$$

and the energy conservation equation

$$\delta' = \theta \quad (1.45)$$

$$\theta' = -\mathcal{H}\theta + c_s^2k^2\delta - k^2\Phi. \quad (1.46)$$

These equations lead to

$$\delta'' + \mathcal{H}\delta' + \left(c_s^2 k^2 + \frac{3}{2}\mathcal{H}^2\right)\delta = 0. \quad (1.47)$$

Perturbations on small scales with $(c_s^2 k^2 - \frac{3}{2}\mathcal{H}) > 0$ do not grow but undergo damped oscillations. These are perturbations with physical wavelength smaller than the Jeans length

$$\lambda_J = c_s \sqrt{\frac{\pi}{G\bar{\rho}}}. \quad (1.48)$$

For the photons and baryons before the decoupling epoch we have $c_S = c/\sqrt{3}$ and the Jeans length is comparable to the Hubble radius H^{-1} and the growth of perturbations is prevented on all scales smaller than that. For a small sound speed $c_s l \ll \mathcal{H}$, the perturbations grow freely (gravitational instability). The resulting equation for a single pressureless fluid becomes

$$\delta'' + \mathcal{H}\delta' - \frac{3}{2}\mathcal{H}^2\delta = 0. \quad (1.49)$$

The growing solution during the matter-dominated era is $\delta \propto a \propto t^{2/3}$ and the gravitational potential remains constant during this epoch.

Growth function and rate

In linear perturbation theory, the gravitational evolution of fluctuations is separable into time-dependent and spatially-dependent (or wavenumber-dependent) parts, i.e.

$$\delta(a) = \delta_0 D(a), \quad (1.50)$$

where δ_0 is present overdensity and the growth function D is normalized as $D(a=1) \equiv 1$. The logarithmic change of growth function is the growth rate f

$$f \equiv \frac{d \ln D}{d \ln a}. \quad (1.51)$$

A very good approximation of a solution to density evolution (1.49) is

$$f \approx |\Omega_m(a)|^\gamma, \quad (1.52)$$

where $\gamma \approx 0.55 - 0.6$ depends only weakly on cosmological parameters (1980 Peebles).

1.2.3 Photon propagation

The above equations describe the evolution of matter density perturbations. Now we will focus on the propagation of light in this perturbed Universe. The photon

momentum is defined via $k^\mu = dx^\mu/d\lambda_s$, where λ_s is an affine parameter. The equations for the propagation are then

$$k_\mu k^\mu = 0, \quad (1.53)$$

$$\frac{dk^\mu}{d\lambda_s} + \Gamma_{\alpha\beta}^\mu k^\alpha k^\beta = 0. \quad (1.54)$$

We will split the momentum vector into a background and a perturbed value $k^\mu = \bar{k}^\mu + \delta k^\mu$. The photon moves in the unperturbed metric along the direction r so that $d\eta = dr$. At the background level, we can integrate the photon path (1.54) to get $\bar{k}^0 \propto a^{-2}$ and therefore the photon frequency $\nu \equiv dt/d\Lambda_s = a\bar{k}^0 \propto a^{-1}$ as expected. The equations for the perturbed part δk are (**2010det0.book.....A**)

$$\frac{d(\delta k^0/k^0)}{d\eta} = - \left(\frac{\partial \Phi}{\partial \eta} + \frac{\partial \Psi}{\partial \eta} + 2 \frac{\partial \Psi}{\partial r} \right), \quad (1.55)$$

$$\frac{d^2 x^i}{d\lambda_s^2} + 2\mathcal{H} \frac{d\eta}{d\lambda_s} \frac{dx^i}{d\lambda_s} = \left(\frac{\partial \Phi}{\partial x^i} - \frac{\partial \Psi}{\partial x^i} \right), \quad (1.56)$$

where the two directions x^1 and x^2 are orthogonal to the propagation direction r .

The Sachs–Wolfe effect

The time part of the geodesic equations (1.55) describes changes in the frequency (redshift) of photons passing through changing gravitational potentials. Integrating the equation along the light-ray null path from the time of emission e to the time of observation o gives us

$$\frac{\delta k^0}{k^0} \Big|_e^o = -2 \Psi|_e^o - \int_e^o \left(\frac{\partial \Phi}{\partial \eta} - \frac{\partial \Psi}{\partial \eta} \right) d\eta, \quad (1.57)$$

where vertical bars represent the change of quantities between e and o . The first ~~effect is referred to as term is called~~ the *Sachs–Wolfe effect* and depends on the difference between the potential at the time of emission and observation. The second ~~effect term~~ is called the *integrated Sachs–Wolfe effect* and depends on the line-of-sight integral of $\Phi - \Psi$.

Weak lensing

The spatial part of the geodesic equations (1.56) can be written for $i = 1, 2$ as

$$\frac{d^2 x^i}{dr^2} = \frac{\partial \psi}{\partial x^i}, \quad (1.58)$$

where the lensing potential $\psi \equiv \Phi - \Psi$. For small displacements, we can put $x^i = r\theta^i$. Integrated the above equation gives us

$$\theta^i = \theta_0^i + \int_0^r d\tilde{r} \left(1 - \frac{\tilde{r}}{r} \right) \frac{\partial \psi(\tilde{r}\theta_0^1, \tilde{r}\theta_0^2, \tilde{r})}{\partial x^i}. \quad (1.59)$$

Two light rays separated by a small angle $\Delta\theta^i$ on the source plane at $r = r_s$ are connected to the observation plane at $r = 0$ by the symmetric transformation matrix

$$A_{ij} \equiv \frac{\partial\theta_s^i}{\partial\theta_o^j} = \delta_{ij} + D_{ij}, \quad (1.60)$$

where the distortion tensor

$$D_{ij} = \int_0^{r_s} d\tilde{r} \left(1 - \frac{\tilde{r}}{r_s}\right) \tilde{r} \frac{\partial^2 \psi}{\partial x^i \partial x^j} = \begin{pmatrix} -\kappa - \gamma_1 & -\gamma_2 \\ -\gamma_2 & -\kappa + \gamma_1 \end{pmatrix}. \quad (1.61)$$

The convergence κ describes the magnification of the source image and the two components of the shear field γ_1, γ_2 describe the distortion of the source image.

1.2.4 Non-linear cosmological perturbations

So far we have described linear gravitational processes which are essential for cosmology as a whole and approximate methods we are exploring. However, as we will compare our results with full N -body simulations, which can deal with the full non-linear dynamics, we will mention here a regime that lies between the linear perturbation theory and the full non-linear gravitational interactions.

One step further from linear order are the second-order perturbations. In this approximation one no longer neglect terms like divergence of the velocity field and the resulting equations are much more complicated than the linear order **2004astro.ph.12025T**; **10.1093/mnras/264.2.375**; **2010deto.book.....A**. We will mention here only the simplest result for a spherical perturbation in Einstein–de Sitter universe with initial Gaussian perturbations **1980Peebles**:

$$\delta = \delta^{(1)} + \delta^{(2)}, \quad (1.62)$$

$$\delta^{(1)} = \delta_0(\mathbf{x}) D_L(a), \quad (1.63)$$

$$\delta^{(2)} = \delta_0^2(\mathbf{x}) D_2(a), \quad (1.64)$$

$$D_2 = \frac{17}{21} D_L^2. \quad (1.65)$$

In general, solutions of higher-order perturbations have to be found numerically and they are computationally similarly expensive as N -body simulations described later in this work.

Another non-linear effect of cosmological importance is the spherical collapse. The model of spherical collapse describes a non-linear evolution of a spherical perturbation in an otherwise smooth expanding background. The equations and their solutions can be derived on purely Newtonian grounds (**2010deto.book.....A**). As one expects, a small perturbation expands with the cosmological expansion, reaches a turnaround point and then the perturbation collapses under its own gravity to a singularity (unphysical phenomenon originated from the exact symmetry).

In the Einstein-de Sitter Universe, we can compute the critical ~~or collapse~~ value δ_{coll} of the linear fluctuation that is reached at the time of the ~~non-linear spherical~~ collapse. This quantity ~~is an important result of this model and it has cosmological relevance as represents~~ a first approximation to the epoch of galaxy formation and ~~can be used~~ to calculate the abundance of collapsed objects. A spherical perturbation ~~in the Einstein-de Sitter Universe collapses will collapse~~ to a singularity whenever the linear density contrast $\delta_L = \delta_{\text{coll}} \approx 1.686$.

One of the main reasons why it is worth to study the phenomenon of a spherical collapse is that we can estimate the number of collapsed objects – future clusters of galaxies. At any given time, we can count how many regions have an overdensity above the collapse threshold given by δ_{coll} which gives us a rough estimate of the number of halos (more in the halo mass function in the next section).

1.3 Cosmological observables

Here we present a brief description of cosmological probes that can be used for constraining dark energy. For more details see e.g. [weinberg observational 2013](#), [2010detobook....A](#), or [DE probes 2](#).

[We have already studied this topic and some of the presented probes in the author's work masterthesis vrastil](#). Although in the main part of the work we deal mainly with large-scale structures and baryonic acoustic oscillations, general overview of other probes might interests some readers. Therefore, we reuse some parts of the former text here. Explicitly, this concerns sub-sections Supernovae, Baryonic acoustic oscillations, Weak lensing, Large-scale structure, Galaxy clusters, Strong lensing, and Redshift-space distortions.

1.3.1 Cosmic distances

In the expanding Universe, there are many ways to specify the distance between two points due to the constantly changing distances and the fact that observers look back in time as they look out in distance.

Comoving distance

The light traveling along the χ direction satisfies the geodesic equation $ds^2 = -dt^2 + a^2(t)d\chi^2 = 0$. The light emitted at the time $t = t_1$ with $\chi = \chi_1$ (redshift z) reaches an observer at time $t = t_0$ with $\chi = 0$ (redshift $z = 0$). Integrating the geodesic equation

$$d_c \equiv \chi_1 = \int_0^{\chi_1} d\chi = - \int_{t_0}^{t_1} \frac{dt}{a(t)} = \frac{1}{H_0} \int_0^z \frac{d\tilde{z}}{E(\tilde{z})}, \quad (1.66)$$

where

$$E(z) \equiv H(z)/H_0 = \sqrt{\Omega_{\gamma,0}(z+1)^4 + \Omega_{m,0}(z+1)^3 + \Omega_{K,0}(z+1)^2 + \Omega_{\Lambda,0}}. \quad (1.67)$$

If we expand $E(z)$ around $z = 0$ we can write the cosmic distance as

$$d_c = \frac{1}{H_0} z - \frac{E'(0)}{2H_0} z^2 + \frac{2E'(0)^2 - E''(0)}{6H_0} z^3 + \mathcal{O}(z^4), \quad (1.68)$$

where a prime now (and for the rest of the work) represents a derivative with respect to z .

Luminosity distance

The luminosity distance d_L is used in supernovae observations to link the supernova luminosity with ~~the expansion rate of the Universe~~its distance. It is defined ~~by as~~(weinberg observational 2013)

$$d_L^2 \equiv \frac{L_s}{4\pi F}, \quad (1.69)$$

where L_s is the absolute bolometric (i.e., integrated over all frequencies) luminosity of a source, and F is the observed bolometric flux. The flux is defined by $F = L_0/S$, where L_0 is the observed luminosity and $S = 4\pi f_K^2(\chi)$ is the area of a sphere at $z = 0$.

The absolute luminosity is defined as the energy emitted per unit time interval, $L = \Delta E/\Delta t$. The energy of a photon is inversely proportional to its wavelength, $E \propto \lambda^{-1} \propto 1+z$, which is stretching in an expanding universe. Also, the time between the arrival of two photons is proportional to the wavelength, $\Delta t \propto \lambda \propto (1+z)^{-1}$. The ratio L_s/L_0 is then

$$\frac{L_s}{L_0} = \frac{\Delta E_1}{\Delta E_0} \frac{\Delta t_0}{\Delta t_1} = (1+z)^2, \quad (1.70)$$

and the luminosity distance is

$$d_L = f_K(\chi)(1+z). \quad (1.71)$$

Using definition f_K (1.4) and comoving distance (1.66) we can express d_L as

$$d_L = \frac{1+z}{H_0 \sqrt{\Omega_{K,0}}} \sinh \left(\sqrt{\Omega_{K,0}} \int_0^z \frac{d\tilde{z}}{E(\tilde{z})} \right). \quad (1.72)$$

For small z we can once again expand the expression and get

$$d_L = \frac{1}{H_0} z - \frac{E'(0) - 2}{2H_0} z^2 + \frac{2E'(0)^2 - 3E'(0) - E''(0) + \Omega_{K,0}}{6H_0} z^3 + \mathcal{O}(z^4). \quad (1.73)$$

Angular diameter distance

The angular diameter distance d_A is defined as **(2010det0.book....A)**

$$d_A \equiv \frac{\Delta x}{\Delta \theta}, \quad (1.74)$$

where $\Delta\theta$ is the angle that subtends an object of actual size Δx orthogonal to the line of sight. Whenever we look at objects of a known size such as CMB anisotropies or BAO scale we use this distance.

The observer measures the size Δx along the surface of a sphere with radius χ and from metric (1.2) follows

$$\Delta x = a(t)f_K(\chi)\Delta\theta. \quad (1.75)$$

The angular diameter distance is then

$$d_A = a(t)f_K(\chi) = \frac{1}{1+z} \frac{1}{H_0 \sqrt{\Omega_{K,0}}} \sinh \left(\sqrt{\Omega_{K,0}} \int_0^z \frac{d\tilde{z}}{E(\tilde{z})} \right). \quad (1.76)$$

Comparing angular diameter distance (1.76) and luminosity distance (1.72) we can see that they have the following relation

$$d_A = \frac{d_L}{(1+z)^2}. \quad (1.77)$$

Degeneracy of the distance measurements

We can see that up to the first order all the distances are the same and reduce to the Euclidean distance and that the Hubble–Lemaître holds. With the increasing redshift, the Hubble–Lemaître does not hold exactly and also different distances behave differently. This can be used to measure different properties of the Universe.

As the distances depend on the cosmological parameters through the integral $\int_0^z d\tilde{z}/E(\tilde{z})$ and through Ω_K we can measure only those parameters contained in $E(z)$. Moreover, if we had distance measurements only around one particular redshift z any combination of parameters that would produce similar $E(z)$ would be equally acceptable. This degeneracy can be broken by a combination of measurements across different redshifts or by using other cosmological probes.

1.3.2 Cosmic Microwave Background

The cosmic microwave background (CMB) is the oldest ($z \sim 1090$) electromagnetic radiation we can see and its surface forms the so-called last scattering surface. The photons were tightly coupled to baryons and electrons before this decoupling epoch in a hot plasma and they could not propagate freely. ~~1965ApJ...142..419P~~ ~~first detected~~ ~~The first detection of~~ ~~the CMB photons was performed by~~ ~~1965ApJ...142..419P~~. ~~They observe the radiation~~ thermalized to an almost uniform temperature across the ~~whole sky~~. The ~~predicted~~ temperature anisotropies of the CMB were first measured at large angular separations by the COBE satellite in ~~1992ApJ...396L...1S~~. The precise measurement of temperature anisotropies by high-precision experiments (~~2003ApJS..148..175S~~) ~~opened up provided~~ a new ~~opportunity direction how~~ to determine cosmological parameters ~~to high precision~~.

The CMB provides critical information regarding our Universe. It can constrain parameters such as Ω_m , Ω_k , the high-redshift normalization of matter fluctuations, the spectral index n_s and curvature $dn_s/d\ln k$ of the scalar fluctuation spectrum, the amplitude and slope of the tensor (gravitational wave) fluctuation spectrum, the post-recombination electron-scattering optical depth τ , and the Hubble constant.

~~In The origin of CMB is described, in most theoretical models, the CMB is generated by as an isotropic Gaussian stochastic process, in which case all the available information concerning the . For gaussian perturbations, all information about the underlying theoretical model can be extracted by measuring is contained in the angular power spectrum of the CMB anisotropies. Because of isotropy Due to the isotropy of the process, one may expand the map CMB in spherical harmonics to extract its angular power spectrum, defined as (2015IJMPD..2430004B)~~

$$C_l^{TT} = \frac{1}{2l+1} \sum_{m=-l}^l |a_{lm}^T|^2, \quad (1.78)$$

where a_{lm} are spherical harmonic coefficients of temperature map T

$$T(\theta, \phi) = \sum_{l=0}^{\infty} \sum_{m=-l}^l a_{lm} Y_{lm}(\theta, \phi), \quad (1.79)$$

where θ, ϕ denote a position on the celestial sphere. It is customary to plot the quantity $l(l+1)C_l/(2\pi)$, which would be constant for a scale-invariant pattern on the sky, see Figure 1.1.

1.3.3 Supernovae¹

Supernovae (SNe) are the most straightforward tool for studying cosmic acceleration, as they directly discovered the acceleration in the first place (**riess**). Type Ia supernovae (SNe Ia) are exploding stars defined by the lack of hydrogen and the presence of silicon in their early-time spectra (**SN**), and are a product of a thermonuclear explosion of a C/O white dwarf. Observations show that SNe Ia have a luminosity peak that is tightly correlated with the shape of their light curves – supernovae that rise and fall more slowly have higher peak luminosity (**SN.lum**). From observations of (multiband) light curve shapes and colors the luminosity at a brightness peak can be predicted.

To measure cosmic expansion with Type Ia SNe, the observed flux and predicted luminosity are compared. From that the supernova's luminosity distance can be measured. An accurate redshift is obtained by measuring the host galaxy (calibrator). As we can see from the equation for the luminosity distance (1.73), this method gives the distance D_L in units of h^{-1} Mpc. Measured relation is used to constraint dark energy parameters.

¹~~Some parts of this section have already been published in masterthesis vrastil.~~

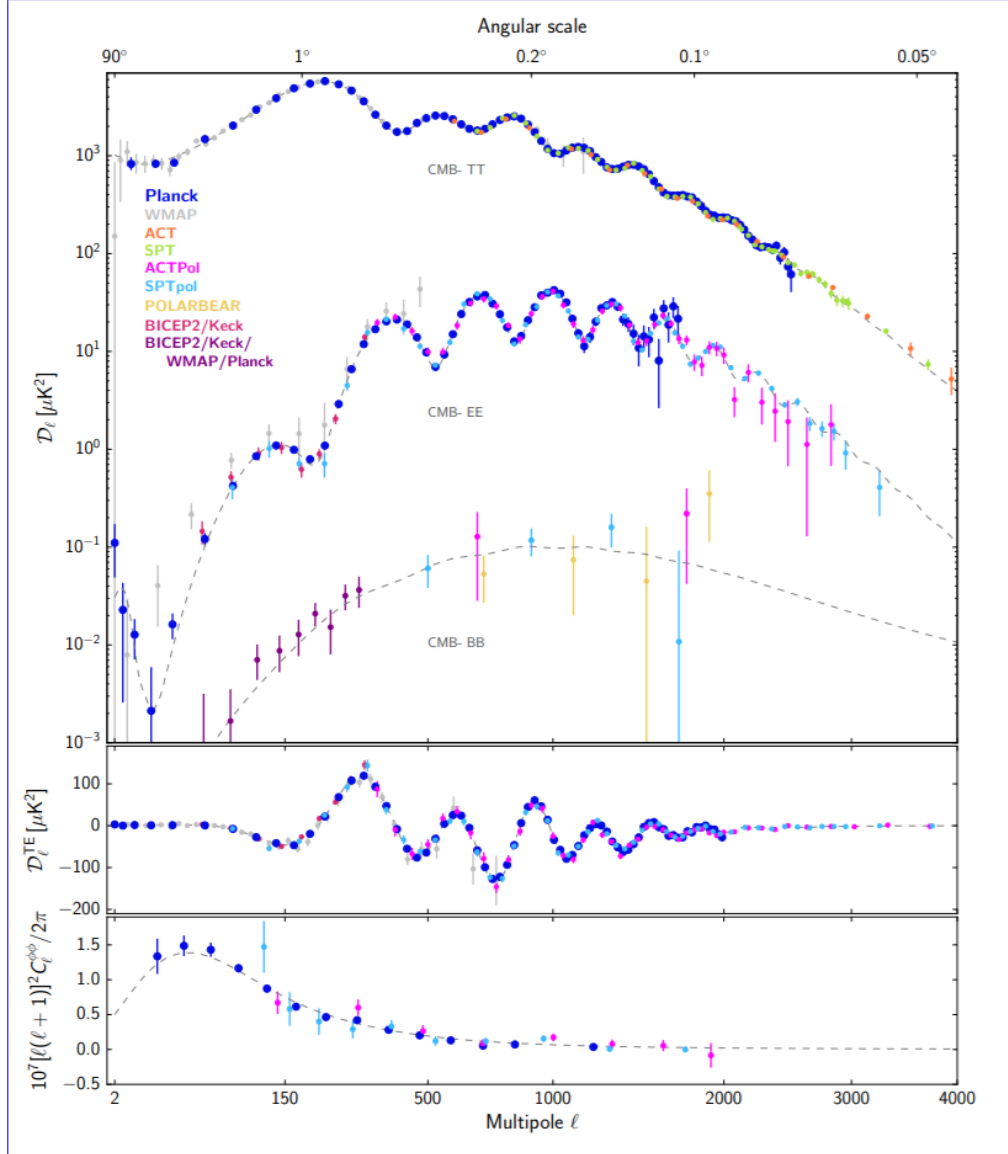


Figure 1.1: Compilation of recent CMB angular power spectrum measurements from which most cosmological inferences are drawn. The upper panel shows the power spectra of the temperature and E-mode and B-mode polarization signals, the next panel the cross-correlation spectrum between T and E, while the lower panel shows the lensing deflection power spectrum. Different colours correspond to different experiments, each retaining its original binning. For Planck, ACTPol, and SPTpol, the EE points with large error bars are not plotted (to avoid clutter). The dashed line shows the best-fit Λ CDM model to the Planck temperature, polarization, and lensing data. *Note:* Reprinted from [2018arXiv180706205P](#).

A recent analysis of [Abbott 2019](#) uses data from the Dark Energy Survey Supernova Program (DES-SN) – 207 spectroscopically confirmed SNe Ia from the first three years of DES-SN combined with a low-redshift sample of 122 SNe from the literature. For a flat w CDM model they found a matter density $\Omega_m = 0.321 \pm 0.018$ and an equation of state $w = -0.978 \pm 0.059$, see Figure 1.2.

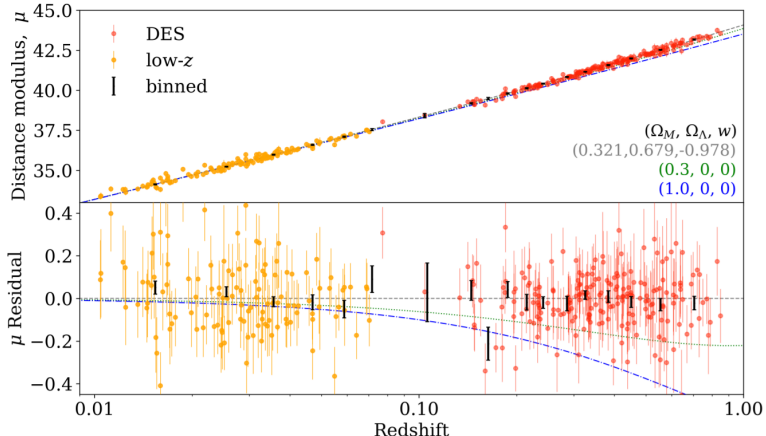


Figure 1.2: Hubble diagram for the DES-SN3YR sample. Top: distance modulus ($\mu = 5 \log[d_L/10\text{pc}]$) from “BEAMS with Bias Corrections” fit (Kessler 2017), black bars, which are used for cosmology fits) and for each SN (red, orange circles). The dashed gray line shows best fit model, while the green and blue dotted lines show models with no dark energy and matter densities $\Omega_m = 0.3$ and 1.0 respectively. Bottom: residuals to the best fit model; 1σ error bars show 68% confidence. Note: Reprinted from Abbott 2019.

1.3.4 Baryonic acoustic oscillations¹

Baryonic acoustic oscillations (BAO) provide an entirely independent way of measuring cosmic distance. Sound waves propagating before recombination imprint a characteristic scale on matter clustering. The acoustic length scale can be computed as

$$r_s = \int_0^{t_*} \frac{c_s(t)}{a(t)} dt = \int_{z_*}^{\infty} \frac{c_s(z)}{H(z)} dz, \quad (1.80)$$

where the asterisk denotes time (redshift) at recombination and c_s is the sound speed. The behavior of $H(z)$ depends on the ratio of the matter density to radiation density and the sound speed depends on the ratio of radiation pressure to the energy density of the baryon-photon fluid, determined by the baryon-to-photon ratio. Both the matter-to-radiation ratio and the baryon-to-photon ratio can be measured from the CMB anisotropy power spectrum. This gives $r_s \sim 150$ Mpc. The scale of the acoustic feature is stable to better than 1% accuracy, making it an excellent standard ruler.

This effect can be detected in the angular clustering of galaxies in bins of photometric redshift, yielding the angular diameter distance. Furthermore, measuring the BAO scale in a velocity separation allows a direct determination of $H(z)$. The BAO method measures $D(z)$ in absolute units – Mpc not h^{-1} Mpc like SNe measurements, and thus BAO measurements to the same redshift carry different information. At low redshift ($z \lesssim 0.5$), the BAO method strongly complements SN measurements, while at higher redshift ($z \gtrsim 0.5$) the BAO method is a powerful probe of dark energy and cosmic geometry.

BAO can be clearly seen in the correlation function (1993ApJ...412...64L) for definition and estimators). The two-point correlation function $\xi(r)$ is

the excess probability dP of finding two pairs of galaxies in two volumes dV_1 and dV_2 at a given comoving distance r

$$dP = \bar{n}^2[1 + \xi(r)]dV_1dV_2, \quad (1.81)$$

where \bar{n} is the expected density of the distribution. The distances are usually measured using the redshift in the redshift space where the distortions (see subsection 1.3.9) cause the redshift-space correlation $\xi(s)$ function to vary according to the angle between the separation vector and the line of sight. In Figure 1.3 we see the spherically averaged correlation function from [2005ApJ...633..560E](#) with the clear bump at $100h^{-1}$ Mpc scale.

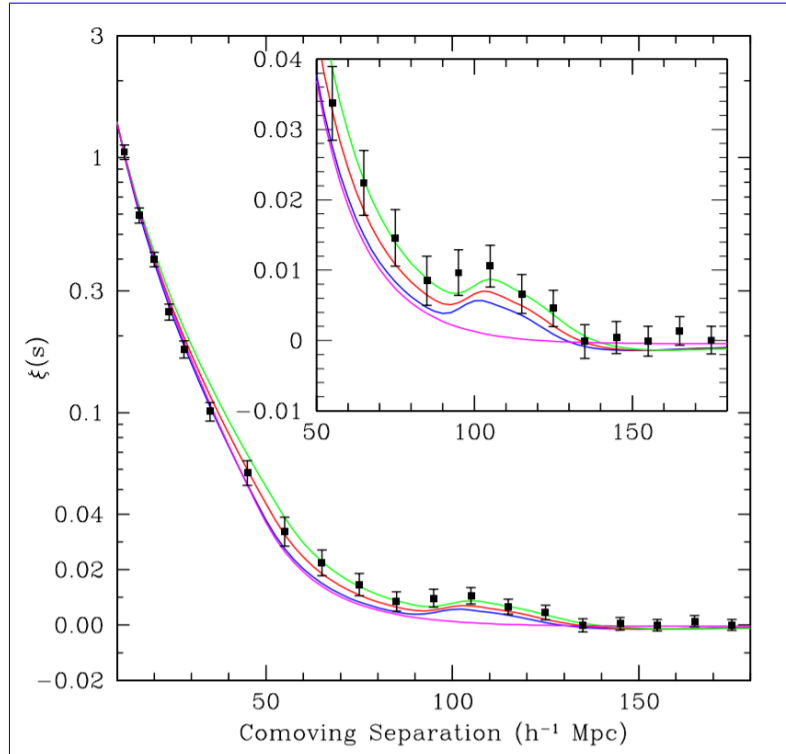


Figure 1.3: The large-scale redshift-space correlation function of the SDSS LRG sample. The error bars are from the diagonal elements of the mock-catalog covariance matrix; however, the points are correlated. Note that the vertical axis mixes logarithmic and linear scalings. The inset shows an expanded view with a linear vertical axis. The models are $\Omega_m h^2 = 0.12$ (top, green), 0.13 (red), and 0.14 (bottom with peak, blue), all with $\Omega_b h^2 = 0.024$ and $n = 0.89$ and with a mild non-linear prescription folded in. The magenta line shows a pure CDM model ($\Omega_m h^2 = 0.105$), which lacks the acoustic peak. It is interesting to note that although the data appears higher than the models, the covariance between the points is soft as regards overall shifts in $\xi(s)$. Subtracting 0.002 from $\xi(s)$ at all scales makes the plot look cosmetically perfect, but changes the best-fit χ^2 by only 1.3. The bump at $100h^{-1}$ Mpc scale, on the other hand, is statistically significant. *Note:* Reprinted from [2005ApJ...633..560E](#).

In **BAO results** present a measurement of the BAO from the three-dimensional correlation of Lyman- α forest absorption and quasars from the SDSS Data Release 14 (the first two years of observations by the eBOSS) at redshift $z = 2.35$. The position of the BAO peak is used to determine the Hubble

distance d_H and the comoving angular diameter distance d_A relative to the sound horizon at the drag epoch r_s : $d_H(z = 2.35)/r_s = 9.20 \pm 0.36$ and $d_M(z = 2.35)/r_s = 36.3 \pm 1.8$. These results are 1.5σ from the flat Λ CDM model of **2016A&A...594A..13P**.

1.3.5 Weak lensing²

Gravitational lensing is the deflection of light from distant sources due to the bending of space-time by baryonic and dark matter (lenses) along the line of sight. It is a very useful cosmological probe because it is sensitive to all matter regardless of its nature. In the limit of very small deflection angles, it is called weak lensing (WL). WL causes tiny distortions ($\sim 0.5\%$), or “shear”, in galaxy sizes and shapes. The intrinsic size or shape of a given galaxy is unknown, but normally, galaxy orientations are assumed to be random ($\sim 30\%$ dispersion), so they should not exhibit statistically significant and coherent alignments. In the presence of lensing, small but coherent shears in background galaxy images are induced. This means that WL is statistically detectable by averaging shapes over many lensed galaxies. In principle, either the shearing of galaxies (shape distortion) or their magnification (size distortion) can be measured. However, in practice, the shape distortions are used much more widely since the scatter in shapes of galaxies is less than the scatter in their sizes.

Weak lensing provides a direct measure of the distribution of matter, independent of any assumptions about galaxy biasing. Since this distribution can be predicted theoretically, and its amplitude can be directly used to constrain cosmology, weak lensing has great potential as a cosmological probe. The correlation of the density field of nearby galaxies with the lensing shear measured on more distant galaxies is called *galaxy-galaxy lensing*. Most lens systems involve sources (and lenses) at moderate or high redshift, and thus can lensing probe the geometry of the Universe – the measurement of the shear correlation function as a function of the redshifts of observed galaxies is called *tomography*. The scaling of the galaxy-galaxy lensing signal as a function of the source redshift, known as *cosmography*, depends purely on geometric factors and hence can be used to construct a distance-redshift relation.

1.3.6 Large-scale structure³

Studying the large-scale structures (LSS) of the Universe is of great importance for the cosmology. Since the clustering of matter on scales from galaxies to superclusters came from quantum fluctuations in the very early Universe with important modification by radiation and baryons, the LSS encode critical information about the contents of the Universe, the origin of the fluctuations, and the cosmic expansion background in which the structures evolved.

Measurements of the large-scale power spectrum for the spatial distribution of matter as a function of redshift constrain the cosmic expansion history, the cosmological distance scale, the growth rate of structures, the mass

²Some parts of this section have already been published in [masterthesis.vrastil](#).

³Some parts of this section have already been published in [masterthesis.vrastil](#).

of the neutrinos, and the abundance of dark matter. This includes the BAO measurement of the distance-redshift relation (as a standard ruler). The BAO with the growth of the LSS in the Universe form two robust probes of dark energy, and a potential discriminator between dark energy and modified gravity models. Beyond the dark energy, the large scale power spectrum is a probe of both neutrino mass and primordial non-Gaussianity.

Matter power spectrum

The matter power spectrum $P(k)$ is defined as a quadratic function of the Fourier transformation of the density contrast δ (**2010detobook.....A**)

$$P(k)(2\pi)^3\delta_D(k - k') \equiv \langle \hat{\delta}(k)\hat{\delta}^*(k') \rangle , \quad (1.82)$$

where δ_D is the Dirac delta function and we are averaging over possible realizations. The power spectrum is ~~by far the most common descriptor of clustering~~ ~~the most used probe in cosmology~~ in the linear and mildly non-linear regime ~~and plays a central role in cosmology~~. The power spectrum is the Fourier transform of the correlation function (1.81)

$$P(k) = \int \xi(r) e^{-ik \cdot r} d^3r . \quad (1.83)$$

However, what we observe in practice is the galaxy density contrast δ_g , which is different from the total matter density contrast δ_m . The two quantities are assumed to be related by a bias factor b defined by (**2010detobook.....A**)

$$b \equiv \frac{\delta_g}{\delta_m} , \quad (1.84)$$

from which follows $P_g(k) = b^2 P_m(k)$. ~~The idea of a simple biasing scheme tries to capture physics beyond the purely linear gravitational treatment, e.g. merging processes~~ ~~This simple assumption tries to incorporate non-linear physical processes, such as merging of galaxies, or evolutionary processes that render of stars that makes galaxies brighter or dimmer~~ ~~and therefore visible or invisible to our telescopes~~.

In Figure 1.4 is shown (linear) matter power spectrum inferred from different cosmological probes (**2018arXiv180706205P**).

1.3.7 Galaxy clusters⁴

The observed number density and clustering of galaxy clusters as a function of mass and redshift provides a powerful toolset to constraining cosmology. Galaxy clusters provided the first line of evidence for the existence of dark matter **zwicky** and cluster mass-to-light ratio measurements suggested that the matter density in the universe was sub-critical **Gott**. Galaxy clusters measurements are sensitive to both the expansion history and the growth of structure in the Universe enabling to distinguish between dark energy and modified gravity models for cosmic acceleration. Additional probes are measurements of the baryonic mass fraction in clusters, and measurements of the tomographic lensing signatures through clusters.

⁴~~Some parts of this section have already been published in masterthesis vrastil.~~

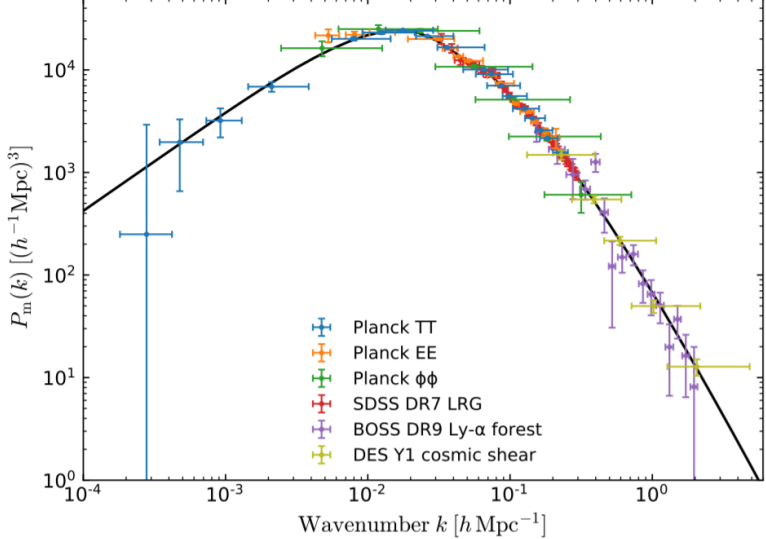


Figure 1.4: The (linear theory) matter power spectrum (at $z = 0$) inferred from different cosmological probes. The broad agreement of the model (black line) with such a disparate compilation of data, spanning 14 Gyr in time and three decades in scale is an impressive testament to the explanatory power of Λ CDM. Earlier versions of similar plots can be found in, for example, [1994ARA&A...32..319W](#), [1995Sci...268..829S](#), [2002PhRvD..66j3508T](#), and [2004ApJ...606..702T](#). A comparison with those papers shows that the evolution of the field in the last two decades has been dramatic, with Λ CDM continuing to provide a good fit on these scales. *Note:* Reprinted from [2018arXiv180706205P](#).

The basic idea of cluster abundance studies is to compare the predicted space density of massive halos to the observed space density of clusters. The basic observables are the richness, the number of galaxies in a specified luminosity and color range. Halo abundance is sensitive to the amplitude of the matter power spectrum σ_8 and the matter density Ω_m , more precisely a combination of a form $\sigma_8 \Omega_m^q$, with $q \approx 0.4$ **white**. The degeneracy between σ_8 and Ω_m can be broken by measuring abundances at a variety of masses.

The halo mass function

The halo mass function (HMF) dn/dM is defined as the number of haloes of mass M per unit volume per unit interval in M . To describe the halo mass function we need two other quantities, $f(\sigma)$ and $\ln \sigma^{-1}$. The rms linear overdensity σ of the density field smoothed with a top-hat filter W with a radius that encloses a mass M at the mean cosmic matter density is defined as ([2015IJMPD..2430004B](#))

$$\sigma^2(M, z) = \frac{D^2(z)}{2\pi^2} \int_0^\infty k^2 P(k) W^2(k, M) dk. \quad (1.85)$$

The mass function is then written as

$$\frac{dn}{dM} = \frac{\rho_0}{M} \frac{d \ln \sigma^{-1}}{dM} f(\sigma), \quad (1.86)$$

where all the cosmological information is contained in the function $f(\sigma)$ – the fraction of mass in collapsed haloes per unit interval in $\ln \sigma$. This function depends on how haloes are defined, usually using the friends-of-friends (FoF) algorithm of **1985ApJ...292..371D**. The analytical form of $f(\sigma)$ using the assumption of collisionless spherical collapse has been proposed by **1974ApJ...187..425P**

$$f_{PS}(\sigma) = \sqrt{\frac{2}{\pi}} \frac{\delta_{\text{coll}}}{\sigma} \exp\left(-\frac{\delta_{\text{coll}}^2}{2\sigma^2}\right), \quad (1.87)$$

where the parameter $\delta_{\text{coll}} = 1.686$ was introduced in the previous section ~~can be interpreted physically as the linearly extrapolated overdensity of a top-hat spherical density perturbation at the moment of maximum compression for an Einstein-de Sitter universe. While as a first approximation the~~. The PS mass function agrees with simulations at $z = 0$ reasonably well, ~~but~~ it overpredicts the number of low-mass halos and underpredicts the number of massive halos at the current epoch (**2007ApJ...671.1160L**). **2001MNRAS.321..372J** combined high-resolution simulations for four different CDM cosmologies spanning a mass range of over 3 orders of magnitude ($\sim 10^{12} - 10^{15} h^{-1} M_\odot$), and including several redshifts $z = 0 - 5$. They came up with the following fitting function

$$f_{Jenkins}(\sigma) = 0.315 \exp\left(-|\ln \sigma^{-1} + 0.61|^{3.8}\right). \quad (1.88)$$

As their range of masses and redshifts correspond to our study case we will use this fitting formula in our analysis (see chapter 5).

1.3.8 Strong lensing⁵

Strong gravitational lensing (SL) refers to the multiple imaging of a background object due to a massive foreground object (typically clusters of galaxies). The resulting angular displacement, morphological distortion, and time delay can be used to measure dark energy parameters. Strong gravitational lensing time delays measure a combination of distances that combining with other dark energy probes can further constraint cosmological parameters. The time delays are also expected to test gravity on scales where the screening mechanisms are becoming active.

Another independent way to measure dark energy parameters with SL is the analysis of systems with multiple sets of multiple images **SL'in'CLGs**. The positions of these multiple images depend strongly on the detailed properties of the lens mass distribution and on the angular diameter distance ratios between the lens, source, and observer, they encapsulate information about the underlying cosmology. This dependence on the geometry can be used to derive constraints on the cosmological parameters.

⁵~~Some parts of this section have already been published in masterthesis vrastil.~~

1.3.9 Redshift-space distortions⁵

When we observe distant galaxies, two features determine their redshifts – the Hubble expansion and their peculiar velocities. The peculiar velocities of galaxies thus cause them to appear displaced along the line of sight in redshift space. These displacements lead to redshift distortions in the pattern of clustering of galaxies in redshift space and make large scale galaxy clustering anisotropic. Redshift-space distortions (RSD) have the tremendous advantage of bearing information about the dynamics of galaxies.

The coordinate transformation from real space (r) to redshift space (s) of a source with a peculiar velocity \mathbf{v} is given by (2010deto.book.....A)

$$\mathbf{s} = \mathbf{r} \left[1 + \frac{u(r) - u(0)}{r} \right], \quad (1.89)$$

where $u \equiv \mathbf{v} \cdot \mathbf{r}/r$. The strength of the anisotropy is governed by distortion parameter $\beta = f(z)/b(z)$, where $f(z)$ is the logarithmic growth rate of fluctuations (1.51) and b is the bias. By modeling the full redshift-space galaxy power spectrum one can obtain a combination of the product of the matter clustering amplitude and the growth rate.

Anisotropy of galaxy clustering offers an alternative to weak lensing and cluster abundances as a tool for measuring the growth of structures. RSD directly measures the rate at which structure is growing at the redshift of observation, unlike WL and galaxy cluster measurements which measure the rate of growth at multiple redshifts. RSD measurements can improve constraints on dark energy models and they can be used to constrain departures from GR by testing the consistency of the growth and expansion histories. The key challenge in modeling RSD is accounting for non-linear effects, including non-linear or scale-dependent bias between galaxies and matter, at the level of accuracy demanded by the LSST's precision. [Cosmological Surveys](#) [There are many projects and missions which study properties of the dark energy, either as a main scientific goal or as a complementary program. Here we mention some of the biggest surveys while directing the reader for further references.](#) Sloan Digital Sky Surveys Sloan Digital Sky Surveys (SDSS, [SDSS](#)) aims to create the most detailed three-dimensional maps of the Universe. From the beginning of regular surveys in 2000 till 2014 there were seven finished surveys in total (SDSS-I/II results [SDSS I II](#), SDSS-III results [BOSS results](#)), while there are three ongoing surveys from 2014 (SDSS-IV, [2017AJ....154...28B](#)) and a planned panoptic spectroscopic survey (SDSS-V, [2017arXiv171103234K](#)) which will start collecting data in summer 2020. The Baryon Oscillation Spectroscopic Survey (BOSS, [BOSS](#)) was a six-year program (Fall 2009 – Spring 2014) designed to measure the scale of baryonic acoustic oscillations (BAO, see subsection 1.3.4) in the clustering of matter. The Extended Baryon Oscillation Spectroscopic Survey (eBOSS, [2016AJ....151...44D](#)) is the new cosmological survey within a SDSS-IV six-year program. eBOSS conducts observations of galaxies and quasars and will expand the selection of luminous red galaxies beyond that probed by BOSS. Dark Energy Survey The Dark Energy Survey (DES) is a program designed to uncover the nature of dark energy by measuring the history of cosmic expansion with high precision. DES is an optical near-infrared survey of 5000

deg^2 of the South Galactic Cap. Starting in August of 2013 and continuing till January 2019, DES begun to survey a large swath of the southern sky out to vast distances in order to provide new clues to these most fundamental questions (**DES**). Euclid Euclid is an ESA (European Space Agency) high-precision space mission designed to study dark matter and dark energy through mapping the geometry and evolution of the Universe ([euclid](#); [2010arXiv1001.0061R](#)). For this purpose, the Euclid will mainly use two independent cosmological probes – weak gravitational lensing and baryonic acoustic oscillation – out to redshift $z \sim 2$. As complementary probes, Euclid will use galaxy clusters and the Integrated Sachs–Wolfe effect. The Euclid mission will start in mid-2022. The overview of the Euclid system design and scientific requirements can be found in [2011arXiv1110.3193L](#). Vera C. Rubin Observatory The Vera C. Rubin Observatory project, previously known as the Large Synoptic Survey Telescope, will conduct the 10-year Legacy Survey of Space and Time (LSST, [lsst](#)). LSST is a ground-based telescope in Chile and will produce a 6-band (300 – 1100 nm) wide-field deep astronomical survey over 20,000 deg^2 of the southern sky. The LSST will scan the sky very rapidly (more than 800 images each night) and each patch of the sky will be visited about 1000 times during the whole survey. LSST’s data will be used for studying the dark matter and the dark energy. LSST will also detect and track potentially hazardous asteroids. The project is in the construction phase and will begin its full science operations in 2022 ([lsst·web](#)). Planck The Planck mission ([planck](#)) was a European Space Agency mission with significant participation from NASA. It was launched into space on May 14, 2009, and was orbiting the second Lagrange point of our Earth-sun system, about 1.5 million km (930,000 miles) away. Planck was measuring the Cosmic Microwave Background (CMB) over a broad range of far-infrared wavelengths. The mission’s goal was to study the geometry and contents of the Universe ([planck·cosm](#)). Planck’s mission ended on 23 October 2013, after nearly 4.5 years of operations ([planck·web](#)). Nancy Grace Roman Space Telescope The Nancy Grace Roman Space Telescope (formerly known as WFIRST, the Wide Field Infrared Survey Telescope) is a NASA space mission designed to study dark energy, exoplanets, and infrared astrophysics ([wmap·web](#)). It will perform wide-field imaging and spectroscopic survey of the near-infrared sky. These data will be used to determine the expansion history of the Universe and the growth history of large-scale structures. WFIRST’s mission should start in the mid-2020s ([WFIRST·report](#)).

2. Dark Energy and Modified Gravity

In this chapter we briefly introduce how we can modify Einstein's general relativity, what are reasons for such modifications (the cosmological constant problem), and the main ideas behind adding new degrees of freedom to the Einstein equations. We describe one particular model of modified gravity in more detail – the $f(R)$ theory and chameleon gravity. We will study the behavior of the chameleon field in spherical systems using numerical techniques.

Some review parts of this chapter has already been studied and described in author's work masterthesis'vrastil. In this work, we deal with the same topic of the $f(R)$ gravity. We also use various notations and equations we already defined in the former work and we need them here, such as the chameleon field χ and related equations. As we further develop the original study of the chameleon, we also took over some parts of the text. We use the text in sections $f(R)$ gravity, Chameleon Gravity, and Other theories, where a general overview of other interesting theories is presented. In section Chameleon Gravity we also extended our previous analysis of chameleon field on cosmological scales and we also extended the study of the chameleon in spherical systems on the scales of galaxy clusters.

2.1 Standard Λ CDM model – successes and issues

The standard cosmological model, the Λ CDM model or the concordance model, assumes that the Universe ~~was created originated~~ in the Big Bang from infinitely hot and dense energy, and now is the Universe composed of about 5% ordinary matter, 27% dark matter, and 68% dark energy (**redefineLCDM**). The Λ CDM model ~~is based upon depends on~~ two theoretical models – the Standard Model of Particle Physics and the General Theory of Relativity. The model also assumes that the universe is homogeneous and isotropic on sufficiently large (cosmic) scales. The model is mathematically described above in chapter 1.

The Λ CDM model represents ~~general relativity~~ the Universe with a cosmological constant Λ ~~which is described by general relativity~~. This cosmological constant is now associated with dark energy ~~and a universe containing~~. The other requirement of this model is the presence of sufficiently massive dark matter particles, ~~i.e., the~~ cold dark matter. However, the nature of both dark energy and dark matter is unknown.

In 1948, **PhysRev.74.505.2** suggested that the elements could have been made during the early hot matter-energy phase associated with the Big Bang and predicted their representation – hydrogen about 75%, helium about 25%, and small amounts of deuterium, lithium, and other light elements.

The other great success of the Big bang model is the prediction of the Cosmic Microwave Background (CMB) radiation and its temperature. In 1948, Natur. 162..774A calculated the present 1948Natur.162..774A predicted the temperature of the CMB to be about approximately 5 K, remarkably very close to the modern current value of about 2.73 K, determined by the COBE satellite. Besides, the COBE results showed an that the CMB is extremely isotropic and homogeneous. These smooth properties of the CMB are not easily explainable in the original Big Bang model and they have led to the theory of inflation (1981PhRvD..23..347G). This model predicts strongly accelerated expansion prior to the decoupling of photons from ordinary matter of the Universe during its very early stage.

The Λ CDM model has an additional major assumption about the existence of dark matter. The notion original need of dark matter arose came from observations of large astronomical objects such as galaxies and clusters of galaxies, which displayed gravitational effects that could not be accounted for by the visible matter. In particular, the galaxy clusters (zwicky) and, later, from observations of 1980ApJ...238..471R, who measured the rotation curves for the luminous matter of many spiral galaxies together with the observations of 1978PhDT.....195B, who compiled galaxy rotation curves (1980ApJ...238..471R) and 21 cm rotation curves for neutral hydrogen gas that extended far beyond the luminous matter of each galaxy, showed that the composite rotation curves were essentially flat out to the edge of the 21 cm data. This implied that considerably more mass was required to be present in each galaxy. This invisible (1978PhDT.....195B). All these objects moved under gravitational forces that could not be caused only by the visible matter. Considerably more gravitational mass was needed to explain these anomalous movements. This missing matter was called dark matter and since to date no. Up-to-date, no experiment searching for direct evidence of the dark matter has been definitely detected and the nature of dark matter remains unknown confirmed its existence and its nature remains unexplained.

The notion of dark energy arose from two Two sets of observations of supernovae of Type Ia by riess and 1999ApJ...517..565P that suggested that the expansion of the universe is accelerating. The conclusion from these observations was that the universe had to contain enough energy to overcome As standard forms of matter cause only attractive gravitational forces, which decelerate the expansion, some new kind of matter-energy is needed to overcome the gravity. This mysterious energy was named “dark energy.”

2.1.1 Cosmological constant problem

The standard cosmological Λ CDM model described above is in a good agreement with all measurements of CMB (planck cosm), type Ia supernovae (Abbott 2019), or BAO (BAO results). However, this concordance model, and namely the cosmological constant, has some significant fundamental problems. Usually, the fine-tuning of the cosmological constant is presented as the main issue but the real issue with the cosmological constant is radiative

instability, and the need to **repeatedly** fine-tune whenever the higher loop corrections are included. We will describe here only the main idea behind these problems, for a more detailed overview see e.g. **2015arXiv150205296P; 2012CRPhy..13..566M**.

The action of the general relativity, together with the action describing matter, is

$$S = \frac{M_{\text{pl}}^2}{2} \int d^4x \sqrt{-g} (R - 2\Lambda_B) + S_m[\psi_m; g_{\mu\nu}], \quad (2.1)$$

where $M_{\text{pl}} \equiv (\sqrt{8\pi G})^{-1}$ is the reduced Planck mass, R is the Ricci scalar (curvature), Λ_B the bare cosmological constant and $S_m[\psi_m; g_{\mu\nu}]$ represents the action of matter fields. The first term (R) is the standard Einstein-Hilbert action. The ~~second term consists of the bare cosmological constant appears in the second term of the above expression cosmological constant~~ and it is ~~merely just~~ a new parameter of the total action. ~~As it~~ The cosmology constant in the action above is compatible with ~~general covariance this term appears to be the principle of general covariance and it is~~ natural from the relativistic point of view. The third term in the ~~above equation action~~ denotes the generic matter action. Variation of the ~~total action~~ action (2.1) with respect to the metric tensor $g_{\mu\nu}$ leads to the Einstein equations ~~of motion~~

$$R_{\mu\nu} - \frac{1}{2} R g_{\mu\nu} + \Lambda_B g_{\mu\nu} = \frac{1}{M_{\text{pl}}^2} T_{\mu\nu}, \quad (2.2)$$

where the stress-energy tensor is defined by

$$T_{\mu\nu} = -\frac{2}{\sqrt{-g}} \frac{\delta S_m}{\delta g^{\mu\nu}}. \quad (2.3)$$

As shown by **1968SPhD...12.1040S**, ~~when one takes into account the~~ quantum field theory ~~the picture is changed~~~~changes the situation~~. The stress-energy tensor of a field placed in the vacuum ~~state~~ is given by

$$\langle 0 | T_{\mu\nu} | 0 \rangle = -\rho_{\text{vac}} g_{\mu\nu}, \quad (2.4)$$

where ρ_{vac} is the constant energy density of the vacuum. The vacuum fluctuations are ~~just a specific type, therefore just another form~~ of energy and ~~in general relativity, all forms of energy gravitate. Therefore as such, they must gravitate. If we take them into account, the Einstein equations when quantum field theory is taken into account are read~~

$$R_{\mu\nu} - \frac{1}{2} R g_{\mu\nu} + \Lambda_{\text{eff}} g_{\mu\nu} = \frac{1}{M_{\text{pl}}^2} T_{\mu\nu}, \quad (2.5)$$

where

$$\Lambda_{\text{eff}} = \Lambda_B + \frac{1}{M_{\text{pl}}^2} \rho_{\text{vac}}. \quad (2.6)$$

~~Therefore, we conclude that the~~ The effective cosmological constant Λ_{eff} is the sum of the bare cosmological constant and a contribution originating from the vacuum fluctuations. ~~The~~ When making observations using the Einstein equations, it is this effective cosmological constant Λ_{eff} is the quantity that one can observe and constrain when tests of the Einstein equations are carried out. ~~The~~ That governs the results. Another problem is that ρ_{vac} is made of several terms which are all includes several different terms, each of them huge in comparison with the observed value of Λ_{eff} and need to be fine-tuned.

Phase Transitions

Another problem with fine-tuning of the cosmological constant comes from changes in the vacuum energy during phase transitions such as was the electroweak phase transition. The contribution to the vacuum energy coming from the minimum of a potential of some field, in this case, the Higgs field, changes as the field takes its new position after the transition. One can calculate this contribution (**2012CRPhy..13..566M**) and for the mass of the Higgs boson $m_H = 125$ GeV arrives at

$$\rho_{\text{vac}}^{EW} \simeq -10^{55} \rho_{\text{crit}}. \quad (2.7)$$

For the quantum chromodynamics transition, one can compute

$$\rho_{\text{vac}}^{EW} \simeq 10^{45} \rho_{\text{crit}}. \quad (2.8)$$

If we fine-tune the vacuum energy to be zero today it had to be non-zero (and huge) before each of these transitions.

Zero-Point Energy Density

When we consider a simple real free scalar field with the potential $V(\Phi) = 2m^2\Phi^2/2$ we will arrive at the vacuum energy

$$\langle \rho \rangle = \langle 0 | T_{00} | 0 \rangle = \frac{1}{2\pi^3} \frac{1}{2} \int d^3k \sqrt{k^2 + m^2}. \quad (2.9)$$

This contribution to the cosmological constant blows up in the ultra-violet regime and is infinite. But this is nothing new in the quantum field theory. If we apply the dimensional regularization (**tHooft:1972tcz**) and subtract the pole, as usual, one is left with a finite energy density of the vacuum

$$\langle \rho \rangle = \frac{m^4}{64\pi^2} \ln \left(\frac{m^2}{\mu^2} \right), \quad (2.10)$$

where μ is a regularization scale. We see that the contribution is proportional to the fourth power of the mass of the particle and therefore, e.g., the photon does not contribute to the vacuum energy density. The equation was derived for the free scalar field but similar contributions with different pre-factors can be computed for all other fields. The overall vacuum energy density is then

$$\rho_{\text{vac}} = \sum_i n_i \frac{m_i^4}{64\pi^4} \ln \left(\frac{m_i^2}{\mu^2} \right) + \rho_B + \rho_{\text{vac}}^{EW} + \rho_{\text{vac}}^{QCD}, \quad (2.11)$$

where $n_H = 1$ stands for the Higgs boson, $n_f = 4$ for fermions and $n_V = 3$ for massive vector fields. For the renormalization scale $\mu \simeq 3 \times 10^{-25}$, as discussed in **2011arXiv1105.6296K**, one calculates the contribution from the zero-point energy of particles to be $\rho_{\text{vac}} \simeq -2 \times 10^8 \text{ GeV}^4$

Radiative instability

The one-loop contributions (2.11) to the vacuum energy can be fine-tuned via the bare cosmological constant and associated ρ_B . Even though the cancellation has to be very precise (one part in $\sim 10^{60}$) we can be fine with this solution. Problems come with two-loops correction which is not significantly suppressed with respect to the one-loop contribution (**2012CRPhy..13..566M**). ~~The~~ Therefore, the cancellation imposed at one-loop is ~~completely spoilt~~, ~~spoilt~~ and one must retune the finite contributions in the counterterm to ~~more or less the same similar~~ degree of accuracy. If we go further, to the three loops, four loops, and so on, we are required to fine-tune each time to extreme accuracy. This is radiative instability and the main cosmological constant problem.

As we know that vacuum energy really does exist, as evidenced by the Lamb shift (**2020Physi...2..105M**) or the Casimir effect (**2006BrJPh..36.1137F**), and that this energy does gravitate, as indicated by measurements of the ratio of gravitational mass to inertial mass for heavy nuclei (**Braginskii:1971tn**), we should take the radiative instability as a serious problem regarding the cosmological constant and be willing to look for alternatives. Other reasons for studying the modifications of gravity may include the following (**2006hep.th....1213N**). Modified gravity:

- can provide natural unification of the early-time inflation and late-time acceleration
- can serve as the basis for a unified explanation of dark energy and dark matter
- is expected to be useful in high energy physics (e.g. for the explanation of hierarchy problem or unification of GUTs with gravity)

2.2 $f(R)$ -gravity¹

One of the simplest modified gravity models is the so-called $f(R)$ gravity in which we consider general functions of the Ricci scalar R in the action

$$S = \frac{M_{\text{pl}}^2}{2} \int d^4x \sqrt{-g} [F(R)] + S_m[\psi_m; g_{\mu\nu}], \quad (2.12)$$

where $F(R) = R + f(R)$ and S_m is the matter action with matter fields ψ_m which are minimally coupled to gravity, i.e. they interact with gravity only through the determinant of the metric $\sqrt{-g}$ and the canonical kinetic term $-\frac{1}{2}g^{\mu\nu}\partial_\mu\psi\partial_\nu\psi$. The matter fields ψ_m obey standard conservation equations and therefore the metric $g_{\mu\nu}$ corresponds to the Jordan frame.

¹~~Some parts of this section have already been published in masterthesis vrastil.~~

Variation with respect to the metric $g^{\mu\nu}$ gives us the equation of motion

$$F_{,R}R_{\mu\nu} - \frac{1}{2}Fg_{\mu\nu} + g_{\mu\nu}\square F_{,R} - \nabla_\mu\nabla_\nu F_{,R} = \frac{1}{M_{\text{pl}}^2}T_{\mu\nu}. \quad (2.13)$$

For $f(R) = -2\Lambda$ the standard Einstein gravity is reconstructed. Taking the trace of (2.13) we get

$$3\square F_{,R} + F_{,R}R - 2F = \frac{1}{M_{\text{pl}}^2}T. \quad (2.14)$$

We see that there is a propagating scalar degree of freedom, so-called *scalarmon* $F_{,R}$ with mass $m^2 = F_{,R}/(3F_{,RR})$, which corresponds to the scalar field conformally coupled to matter in the Einstein frame.

To get the inflation we need a solution that approaches the de Sitter solution characterized by vacuum space with constant positive curvature. Thus $\square F_{,R} = 0$ and (2.14) becomes

$$F_{,R}R - 2F = 0. \quad (2.15)$$

For example, the model $F(R) = \alpha R^2$ gives rise to an asymptotically exact de Sitter solution and can be responsible for the inflation in the early Universe. In the model $f(R) = R + \alpha R^2$, the inflation ends when the quadratic term becomes smaller than the linear term. As at the present epoch is the curvature very small this model is not suitable to realize the present cosmic acceleration. Models like $f(R) = -\alpha/R^n$ with $\alpha > 0$, $n > 0$ could in principle give rise to the present acceleration. However, these models do not satisfy local gravity constraints because of the instability associated with negative values of $f_{,RR}$. Moreover, the standard matter epoch is not present because of a large coupling between the Ricci scalar and the non-relativistic matter.

There are four conditions for the viability of $f(R)$ models (**Amendola'2007**)

- $F_{,R} > 0$ (for $R > R_0$), where R_0 is the Ricci scalar at the present epoch,
– required to avoid anti-gravity (**2010deto.book.....A**)
- $F_{,RR} > 0$ (for $R > R_0$),
– required for consistency with local gravity tests (**2005gr.qc.....5136O**),
for
the presence of the matter-dominated epoch (**2007PhRvL..98m1302A**)
and the stability of cosmological perturbations (**2007PhRvD..75d4004S**)
- $F(R) \rightarrow R - 2\Lambda$ (for $R \gg R_0$),
– required for consistency with local gravity tests (**2008PhRvD..77b3507T**) and for the presence of the matter-dominated epoch (**Amendola'2007**)
- $0 < \frac{RF_{,RR}}{F_{,R}} < 1$ (for $F_{,R}R - 2F = 0$).
– required for the stability of the late-time de Sitter solution (**1988PhLB..202..198M**)

Some examples of $f(R)$ models that satisfy these conditions:

$$f(R) = -\mu R_c (R/R_c)^p \quad \text{for } 0 < p < 1; \mu, R_c > 0, \quad (2.16)$$

$$f(R) = -\mu R_c \frac{(R/R_c)^{2n}}{(R/R_c)^{2n} + 1} \quad \text{for } n, \mu, R_c > 0, \quad (2.17)$$

$$f(R) = -\mu R_c \left[1 - (1 + R^2/R_c^2)^{-n} \right] \quad \text{for } n, \mu, R_c > 0, \quad (2.18)$$

$$f(R) = -\mu R_c \tanh(R/R_c) \quad \text{for } \mu, R_c > 0. \quad (2.19)$$

One of the main predictions of $f(R)$ gravity is a different structure formation history than in Λ CDM. For the large-scale structure formation on subhorizon scales $k \gg H$ in quasi-static approximation one gets the modified equation for matter density perturbation (**2011RSPTA.369.4947B**)

$$\ddot{\delta}_m + 2H\dot{\delta}_m - 4\pi G_{\text{eff}}\rho_m\delta_m \approx 0, \quad (2.20)$$

where the effective gravitational constant is defined by

$$G_{\text{eff}} \equiv \frac{G}{1 + f_{,R}} \frac{4k^2 + 3a^2m^2}{3k^2 + 3a^2m^2}. \quad (2.21)$$

On scales much larger than the scalaron Compton wavelength m^{-1} , gravity is unmodified aside from the overall reduction factor $f_{,R}$. However, on smaller scales the gravitational coupling increases by the factor 4/3. As the scalaron mass m and the factor $f_{,R}$ depend on curvature (local density), the chameleon mechanism discussed earlier can prevent the detection of this effect in the Solar System.

2.2.1 Jordan vs. Einstein Frame

The action (2.12) is described in the so-called Jordan frame, where the matter fields are minimally coupled to the metric and follow geodesics. We can also describe the action in the so-called Einstein frame, where “standard” gravity is restored. Using the conformal transformations

$$\begin{aligned} \tilde{g}_{\mu\nu} &\equiv F_{,R} g_{\mu\nu}, \\ \phi &\equiv M_{\text{pl}} \sqrt{\frac{3}{2}} \ln F_{,R}, \\ A(\phi) &\equiv F_{,R}^{-1/2}, \\ V(\phi) &\equiv \frac{M_{\text{pl}}^2}{2} \frac{F_{,R}R - F}{F_{,R}^2}, \end{aligned} \quad (2.22)$$

we can rewrite the action (2.12)

$$S = \int d^4x \sqrt{-\tilde{g}} \left[\frac{M_{\text{pl}}^2}{2} \tilde{R} - \frac{1}{2} (\partial\phi)^2 - V(\phi) \right] + S_m[\psi_m; A^2(\phi)\tilde{g}_{\mu\nu}], \quad (2.23)$$

where tildes denote quantities in the Einstein frame. This action looks like the Einstein-Hilbert action with minimally coupled scalar but now the matter fields are also coupled with the scalar field via factor $A(\phi)$.

There is a difference between whether one takes action (2.12) or (2.23) to be the fundamental action defining the modified gravity. In the former one, there is only one coupling constant β , defined by $A(\phi) = \exp(\beta\phi/M_{\text{pl}})$, for all matter fields. If one takes the action in the Einstein frame to be the fundamental one the matter action is replaced by $S_m[\psi_m; A^2(\phi)\tilde{g}_{\mu\nu}] \rightarrow S_i[\psi_i; A_i^2(\phi)\tilde{g}_{\mu\nu}]$ where one can define the coupling strengths β_i to the different matter components to be different. This is very important for tests of modified gravity. For instance, if there is minimal coupling to the baryonic matter, $\beta_b = 0$, Solar System or astrophysical tests do not constraint coupling strength to the cold matter β_c whereas the cosmological observations do.

Note that the coupling constant for $f(R)$ is $\beta = \sqrt{1/6}$ but for other more general theories this coupling can vary. Even for $f(R)$ theories, one expects that loop corrections can change the coupling strength. Also, other theories such as the Jordan–Brans–Dicke theory, Kaluza–Klein theories, and higher derivative theories of gravity, can be formulated in two different ways (**Faraoni:1998qx**).

These two conformally related frames are physically equivalent, i.e. physical observations are frame independent, but the frame dependence of cosmological perturbations has led to confusion in the past. There have been many debates about the (in)equivalence of these frames (**Postma:2014vaa**) and whether which one is the physical (**Faraoni:1999hp**). Many contradictory arguments (sometimes incorrect) of both sides result in confusion and ambiguous viewpoints.

It has been shown in **Magnano:1993bd** that these two frames are *mathematically* equivalent, i.e. every solution in one frame implies an existence of a solution in the other frame and can be mapped into this frame. The confusion about their physical equivalence comes from interpretations of experiment results. For example, *ordinary* cosmology described by Einstein’s theory leads to an expanding universe solution. Coming to the Jordan frame we can interpret the scale factor as a scalar field which is coupled to matter. In this case, the redshift of spectral lines is no longer interpreted as an effect due to the expansion of the Universe, but due to growth of coupling constants such that the present transition energies are higher than those in the past. Hence the Jordan frame physicist does not see an expanding Universe, but growing coupling constants. Nevertheless, the measured redshift of spectral lines is the same for both frames.

Both frames have some issues with fundamental principles. In the Jordan frame, the weak energy condition can be violated and hence states with the negative energy are possible. Moreover, there is no guarantee of stability of the ground state. All *classical* fields are believed to satisfy the energy condition but no so in quantum theories. On the other hand in the Einstein frame, the weak energy condition is satisfied but due to the non-universal coupling of the matter fields, the equivalence principle is violated. However, this violation is only weak and can pass the Solar system tests.

2.2.2 Screening Mechanisms

We know that general relativity with the cosmological constant and assumptions about the cold dark matter can describe our universe very well. That means

that any modified cosmology must be able to recover Λ CDM cosmology to high accuracy. This is not normally an issue. However, since modifications of GR typically involve an extra scalar degree of freedom there are interactions with matter that are unavoidable – no symmetry can prevent all couplings to the standard model. This coupling to matter means that there should be a fifth force. Because we do not see any fifth forces or modifications of gravity in the laboratory or in the Solar System we need to suppress these fifth forces – we need some sort of a *screening mechanism*.

The nature of the screening mechanisms can be different. Let us start from (2.23) with the generalized kinetic term $-\frac{1}{2}Z(\phi, \partial\phi, \dots)(\partial\phi)^2$. We can solve the equations of motion for the background in a minimum of a potential $V(\phi)$ and write $\phi = \phi_0 + \delta\phi$, where ϕ_0 is a background solution and $\delta\phi$ is a fluctuation. The Lagrangian density for the fluctuations to the second order (first order vanishes) is

$$\mathcal{L} \propto -\frac{1}{2}Z(\phi_0)(\partial\delta\phi)^2 + \frac{1}{2}m^2(\phi_0)\delta\phi^2 + \frac{\beta(\phi_0)}{M_p}\delta\phi\delta T, \quad (2.24)$$

where $m^2(\phi) \equiv V_{,\phi\phi}(\phi)$. Now, any of these three terms can serve as a screening term:

- *Large inertia* – a large Z makes it hard for the scalar to propagate and leads to the kinetic type of the screening, where first or second derivatives being important; e.g. Galileons (**2009PhRvD..79f4036N**), massive gravity (**2012RvMP...84..671H**) or Vainshtein mechanism (**2013CQGra..30r4001B**);
- *Large mass* – a large m means the scalar propagates only over short distances and leads to the chameleon type of the screening, where in regions of high-density, such as on the Earth, the field acquires a large mass – the Chameleon mechanism (**Waterhouse:2006wv**);
- *Weak coupling* – a small β in regions of high density makes the interaction with matter fields weaker and leads to symmetron (**2010PhRvL.104w1301H**) or varying dilaton (**Damour:1994zq**; **2011PhRvD..83j4026B**) theories.

2.3 Chameleon Gravity²

We now describe $f(R)$ gravities exhibiting the chameleon mechanism in more detail. As stated, this mechanism uses the large mass of the chameleon field in high-density regions and chameleon gravity can satisfy tests of the equivalence principle in the Solar System. The action of a chameleon scalar field χ in the Einstein frame is given by the action (2.23). Varying the action with respect to the field χ one can obtain the equation of motion

$$\square\chi = V_{,\chi} - \sum_i \frac{\beta_i}{M_{\text{pl}}} e^{4\beta_i\chi/M_{\text{pl}}} g_{(i)}^{\mu\nu} T_{\mu\nu}^{(i)}, \quad (2.25)$$

²Some parts of this section have already been published in [masterthesis.vrastil](#).

where $T_{\mu\nu}^{(i)}$ is the stress-energy tensor for the i -th matter component. For a perfect isotropic fluid the equation of motion is

$$\square\chi = V_{,\chi} + \sum_i (1 - 3w_i) \frac{\beta_i}{M_{\text{pl}}} \rho_i e^{(1-3w_i)\beta_i\chi/M_{\text{pl}}}. \quad (2.26)$$

This equation could be read as

$$\square\chi = V_{\text{eff},\chi}(\chi), \quad (2.27)$$

where the effective potential V_{eff} is defined by

$$V_{\text{eff}}(\chi) \equiv V(\chi) + \sum_i \rho_i e^{(1-3w_i)\beta_i\chi/M_{\text{pl}}}. \quad (2.28)$$

If the couplings β_i are the same for each matter component with the same w (we can omit the radiation in the sum) and the overall density is $\rho = \sum_i \rho_i$, then the effective potential reads

$$V_{\text{eff}}(\chi) \equiv V(\chi) + \rho e^{(1-3w)\beta\chi/M_{\text{pl}}}. \quad (2.29)$$

For the quasi-static and weak ($\beta\chi/M_{\text{pl}} \ll 1$) field in a weak gravity background (the Minkowski background) with the non-relativistic matter, the equation further simplifies as

$$\Delta\chi = \frac{\beta}{M_{\text{pl}}} \rho + V_{,\chi}, \quad (2.30)$$

which looks like the normal Poisson equation but with an extra non-linear term.

2.3.1 Chameleon Force

The interaction of the chameleon field with matter is described by the conformal coupling (2.22). Free matter fields $\psi_m^{(i)}$ follow geodesics of the Jordan frame metric. In the Einstein frame, they follow modified trajectories affected by the chameleon field (**Waterhouse:2006wv**)

$$\frac{d^2x^\mu}{d\tau^2} + \Gamma_{\alpha\beta}^\mu \frac{dx^\alpha}{d\tau} \frac{dx^\beta}{d\tau} = -\frac{\beta_i}{M_{\text{pl}}} \left(2\chi_{,\alpha} \frac{dx^\alpha}{d\tau} \frac{dx^\mu}{d\tau} + g^{\beta\mu} \chi_{,\beta} \right). \quad (2.31)$$

Note that the chameleon force violates the weak Equivalence Principle only if there exist two matter species with differing values of β_i . In the non-relativistic limit, a test particle of mass m of species i in a static chameleon field χ is moving under a force \mathbf{F}_χ given by

$$\frac{\mathbf{F}_\chi}{m} = -\frac{\beta_i}{M_{\text{pl}}} \nabla\chi \quad (2.32)$$

2.3.2 Chameleon mechanism

As discussed previously, we need some sort of a screening mechanism to avoid Solar System tests of GR. It means as seen from (2.32) that the chameleon potential needs to approach some constant value in dense regions or at least have a marginally suppressed amplitude.

Suppose we have a background solution χ_0 which minimizes the effective potential with $\rho = \rho_0$. For small fluctuations $\chi = \chi_0 + \delta\chi$ and $\rho = \rho_0 + \delta\rho$ we can linearize (2.30) to obtain

$$\Delta\delta\chi = \frac{\beta}{M_{\text{pl}}} \delta\rho + m_0^2 \delta\chi, \quad (2.33)$$

where

$$m_0^2 \equiv V_{,\chi\chi}(\chi_0). \quad (2.34)$$

Except for the screening term, the equation (2.33) has the same behavior as the Poisson equation for the Newtonian potential Φ_G . For a spherically symmetric density profile, this gives solution

$$\chi = \chi_0 + 2\beta M_{\text{pl}} \Phi_G(r) e^{-m_0 r}. \quad (2.35)$$

As the objects in the background become more massive (larger and/or denser) the Newtonian potential grows larger (in magnitude) and so the deviation of χ from background solution χ_0 . At some point, this deviation is no longer small and the potential term in (2.30) cannot be treated perturbatively. It starts canceling the first source term and eventually the field χ posses a new value which minimizes the effective potential inside an object.

This is the essence of the chameleon mechanism. Let us derive the mechanism more properly and exactly.

2.3.3 Chameleon Profile

To obtain the chameleon behavior described above we need to choose a chameleon potential $V(\chi)$ with the right properties. To have a screening mechanism in (2.30) we need $V_{,\chi} < 0$ to cancel the source term and $V_{,\chi\chi} > 0$ to have a real mass of the field and stable behavior of perturbations.

We wish to find a solution for spherically symmetric matter distributions of a single species of pressureless matter such that

$$\rho(r) = \begin{cases} \rho_c & r < R_s \\ \rho_0 & r > R_s, \end{cases}$$

where $\rho_c > \rho_0$. Further, we define χ_c and χ_0 with their masses m_c and m_0 (the masses of small fluctuations about χ_c and χ_0) such as

$$\begin{aligned} V_{\text{eff},\chi}(\chi_c)|_{\rho=\rho_c} &\equiv 0 & m_c^2 &\equiv V_{\text{eff},\chi\chi}(\chi_c) \\ V_{\text{eff},\chi}(\chi_0)|_{\rho=\rho_0} &\equiv 0 & m_0^2 &\equiv V_{\text{eff},\chi\chi}(\chi_0). \end{aligned}$$

In the background with low density, the curvature of the potential is much shallower, corresponding to a light scalar that mediates a long-range force. Inside the object of high density, the scalar acquires a large mass, and the force shuts off.

In spherical coordinates assuming spherical symmetry, equation (2.30) becomes

$$\frac{d^2\chi}{dr^2} + \frac{2}{r} \frac{d\chi}{dr} = \frac{1}{r} \frac{d^2(r\chi)}{dr^2} = V_{,\chi}(\chi(r)) + \frac{\beta}{M_{\text{pl}}} \rho(r). \quad (2.36)$$

We must impose two boundary conditions which are

$$\begin{aligned} \frac{d\chi}{dr}(r=0) &= 0 \\ \chi(r \rightarrow \infty) &= \chi_0. \end{aligned}$$

The first one corresponds to a non-singularity of the solution at the origin while the later one ensures that the chameleon force vanishes at the infinity (as $d\chi/dr \rightarrow 0$).

The equation (2.36) drives the field χ toward the χ_0 outside the object and toward χ_c inside the object. To solve (2.36), we must do several approximations. Outside the object, we assume that the field sits near the extreme χ_0 and we can linearize our equation

$$\frac{1}{r} \frac{d^2(r\chi)}{dr^2} = m_0^2(\chi - \chi_0), \quad (2.37)$$

with the decaying solution

$$\chi(r) = -\frac{\beta}{4\pi M_{\text{pl}}} \frac{\tilde{M}}{r} e^{-m_0 r} + \chi_0. \quad (2.38)$$

Note that the integration constant \tilde{M} is not generally the mass of the object M_c as in the case of the Newtonian potential because it is determined by the field inside the object which has different behavior than the Newtonian potential. As we will see later, for small Newtonian potentials (in magnitude) this effective mass $\tilde{M} \approx M_c$ but as the potential grows larger part of the object's mass is screened away $\tilde{M} < M_c$.

Inside the object, we use one of the two approximations based on the initial value of $\chi_i \equiv \chi(0)$ – either $\chi_i \approx \chi_c$ or $\chi_i \gg \chi_c$.

Thin-shell regime

In the *thin-shell* regime, the field initially sits very close the minimum χ_c , i.e. we require

$$(\chi_i - \chi_c)/\chi_c \ll 1. \quad (2.39)$$

The field is frozen near this value until the friction term is sufficiently small to allow the field to roll. This “moment” is denoted by R_{roll} . As soon as χ is

displaced significantly from χ_c we may neglect the potential term in (2.36). This gives us the solution

$$\chi(r) = \begin{cases} \chi_c & 0 < r < R_{roll} \\ \frac{\beta}{6M_{\text{pl}}} \rho_c r^2 + \frac{A}{r} + D & R_{roll} < r < R_s. \end{cases} \quad (2.40)$$

We have boundary conditions coming from the requirement on matching χ and $d\chi/dr$ at R_{roll} , namely: $\chi = \chi_c$ and $d\chi/dr = 0$ at $r = R_{roll}$. This fixes our constants and the solution is

$$\chi(r) = \begin{cases} \chi_c & 0 < r < R_{roll} \\ \frac{\beta\rho_c}{3M_{\text{pl}}} \left(\frac{r^2}{2} + \frac{R_{roll}^3}{r} \right) - \frac{\beta\rho_c R_{roll}^2}{2M_{\text{pl}}} + \chi_c & R_{roll} < r < R_s. \end{cases} \quad (2.41)$$

The approximation of separating the solution into the two regions only makes sense if $(R_s - R_{roll})/R_s \ll 1$. Otherwise, there is no clear separation between the two regions, and one needs a solution valid over the entire range $0 < r < R_s$. In subsection 2.3.5 we solve equation (2.36) numerically and we will check these approximations against numerical solutions.

With approximation $(R_s - R_{roll})/R_s \ll 1$, we can determine the effective mass of the object \tilde{M} from the requirement $\chi(R_s^-) = \chi(R_s^+)$ and $d\chi/dr(R_s^-) = d\chi/dr(R_s^+)$.

$$\tilde{M} = \frac{3\Delta R_s}{R_s} M_c, \quad (2.42)$$

where

$$\frac{\Delta R_s}{R_s} \equiv \frac{\chi_0 - \chi_c}{6\beta M_{\text{pl}} |\Phi_G(R_s)|} \approx \frac{R_s - R_{roll}}{R_s} \ll 1. \quad (2.43)$$

This qualitative derivation of the thin-shell regime is using too much assumptions and can be done more precisely without ignoring some of the terms but then it is harder to see the principle of the thin-shell effect. For more details see e.g. **Tamaki:2008mf; 2007PhRvD..75f3501M; Waterhouse:2006wv**.

Thick-shell regime

In the *thick-shell* regime, the field is initially sufficiently displaced from the minimum $-\chi_i \gg \chi_c$ that it begins to roll almost immediately (no friction term). Hence the interior solution is most easily obtained by taking the $R_{roll} = 0$ in (2.41) and replacing χ_c by χ_i

$$\chi(r) = \frac{\beta\rho_c r^2}{6M_{\text{pl}}} + \chi_i \quad 0 < r < R_s. \quad (2.44)$$

By matching the interior and exterior solutions, we obtain

$$\begin{aligned} \chi_i &= \chi_0 - 3\beta M_{\text{pl}} \Phi_G(R_s) \\ \tilde{M} &= M_c, \end{aligned} \quad (2.45)$$

which is the linear regime with no screening. From the definition of $\Delta R_s/R_s$ we also obtain

$$\frac{\Delta R_s}{R_s} \equiv \frac{\chi_0 - \chi_c}{6\beta M_{\text{pl}} |\Phi_G(R_s)|} > 1. \quad (2.46)$$

Thin-shell suppression factor

The chameleon force outside the object (where experiments take place) comparing to the Newtonian force is

$$\begin{aligned}\frac{F_{\text{thick}}}{F_N} &= 2\beta^2 \\ \frac{F_{\text{thin}}}{F_N} &= 2\beta^2 \frac{3M_{\text{pl}}(\chi_0 - \chi_c)}{\beta\rho_c R_c^2},\end{aligned}\tag{2.47}$$

where we ignore the term $m_0r \ll 1$. Therefore for the coupling β of order unity, the chameleon force is as strong as gravity unless it is screened away by the thin-shell effect.

2.3.4 Hu-Sawicki $f(R)$ Model

We wish to study a class of $f(R)$ models that accelerate cosmic expansion at late times, without the cosmological constant, while satisfying both cosmological and Solar System tests. We consider the family of Hu-Sawicki $f(R)$ models (**Hu-Saw**). The action of these models is given by (2.12) and $f(R)$ has a broken power-law form

$$f(R) = -M^2 \frac{c_1(R/M^2)^m}{c_2(R/M^2)^m + 1},\tag{2.48}$$

where the mass scale $M^2 \equiv \bar{\rho}_0/3M_{\text{pl}}^2$, $m > 0$, and c_1 and c_2 are dimensionless parameters such that at high redshifts ΛCDM cosmology is restored.

The formulation of modified gravity in this frame leads to second-order differential equations of motion (2.13) for R and fourth-order field equations for $g_{\mu\nu}$. With a conformal transformation (2.22) we may rewrite these equations in the Einstein frame with second-order differentials only (**CHIBA20031**). In the Einstein frame, the Hu-Sawicki models correspond to chameleon gravity with the potential

$$V(\chi) = M_{\text{pl}}^2 \Lambda - \frac{\beta\bar{\rho}_0}{nM_{\text{pl}}} (2\beta M_{\text{pl}}\Phi_{0,\text{scr}})^{1-n} \chi^n,\tag{2.49}$$

$$V_{,\chi}(\chi) = -\frac{\beta}{M_{\text{pl}}}\bar{\rho}_0 \left(\frac{2\beta M_{\text{pl}}\Phi_{0,\text{scr}}}{\chi} \right)^{1-n},\tag{2.50}$$

where $\beta = \sqrt{1/6}$ and the power-law exponent n and screening potential $\Phi_{0,\text{scr}}$ are now the free parameters of the theory. The screening potential has the following relation to the present scalaron value in $f(R)$ -gravity:

$$\Phi_{0,\text{scr}} = \frac{3}{2} \ln(1 + f_{R0}) \approx \frac{3}{2} f_{R0}.\tag{2.51}$$

The chameleon obeys the equation of motion (2.25) which reduces for our study case (non-relativistic pressureless matter) to

$$\Delta\chi = \frac{\beta}{M_{\text{pl}}}\rho - \frac{\beta}{M_{\text{pl}}}\bar{\rho}_0 \left(\frac{2\beta M_{\text{pl}}\Phi_{0,\text{scr}}}{\chi} \right)^{1-n}\tag{2.52}$$

We rescale the equations to units in which we can clearly see the role of the screening potential Φ_{scr} and its relation to the gravitational potential Φ_G . We start by defining a few special values of the chameleon potential – the current background value

$$\chi_0 \equiv 2\beta M_{\text{pl}} \Phi_{0,\text{scr}}, \quad (2.53)$$

the background value at a given time (for a matter-dominated universe)

$$\chi_a(a) \equiv \chi_0 a^{3/(1-n)} \quad (2.54)$$

and the value of the screening potential at a given time

$$\Phi_{a,\text{scr}} \equiv \Phi_{0,\text{scr}} a^{\frac{5-2n}{1-n}}. \quad (2.55)$$

With these definitions, we rewrite equation (2.30) as

$$\Delta(\chi/\chi_a) = C_\chi(a) \left[1 + \delta - \left(\frac{\chi_a}{\chi} \right)^{1-n} \right], \quad (2.56)$$

where the pre-factor $C_\chi(a)$ is defined by

$$C_\chi(a) \equiv \frac{3H_0^2 \Omega_m}{2\Phi_{0,\text{scr}}} a^{-3\frac{2-n}{1-n}} = (a\mu\Phi_{a,\text{scr}})^{-1}. \quad (2.57)$$

Linear prediction

Equation (2.56) is similar to the Poisson equation for the gravitational potential and gives meaning to the screening potential $\Phi_{a,\text{scr}}$. If we assume $\chi \approx \chi_a$, then

$$\Delta(\chi/\chi_a) \approx (\mu\Phi_{a,\text{scr}})^{-1} \frac{\delta}{a} = \Delta(\Phi_G/\Phi_{a,\text{scr}}) \quad (2.58)$$

and we can write down a linear solution as

$$\chi(\mathbf{x}, a) = \chi_a(a) \left(1 + \frac{\Phi_G(\mathbf{x}, a)}{\Phi_{a,\text{scr}}(a)} \right). \quad (2.59)$$

Here we can clearly see the role of the (time-dependent) screening potential $\Phi_{a,\text{scr}}$ – as long as $|\Phi_G| < \Phi_{a,\text{scr}}$ we have a valid solution but once the gravitational potential is large enough (in its negative values) the linear solution breaks down, as the chameleon field would become negative.

We may derive a more accurate solution in Fourier space. If the chameleon field sits near its background value, i.e. $\chi = \chi_a(1 + \delta\tilde{\chi})$, where $\delta\tilde{\chi} \ll 1$, we can rewrite (2.56) as

$$\Delta\delta\tilde{\chi} = \frac{m^2}{1-n} \delta + m^2 \delta\tilde{\chi}, \quad (2.60)$$

where the mass of the chameleon field is

$$m^2(a) \equiv \frac{1-n}{a\mu\Phi_{a,\text{scr}}}. \quad (2.61)$$

This equation has a solution in k -space of the form

$$\hat{\chi}(k) = -\frac{\chi_a}{1-n} \frac{m^2}{m^2 + k^2} \hat{\delta}(k) = -\frac{\beta \bar{\rho}}{M_{\text{pl}}} \frac{\hat{\delta}(k)}{k^2 + m^2}. \quad (2.62)$$

The other regime, which can be solved approximately, is the screened regime inside massive objects. When the solution (2.59) breaks down, and if $\delta(x)$ is approximately constant, the solution of equation (2.56) is

$$\chi = \frac{\chi_a}{(1+\delta)^{1/(1-n)}}. \quad (2.63)$$

Because χ_a is constant in space the chameleon force (2.32) vanishes in this screened regime.

In Figure 2.1 we show the evolution of background parameters of the chameleon field – Compton wavelength $\lambda_c = m^{-1}$, background value of the chameleon field χ_a and the screening potential $\Phi_{a,\text{scr}}$ – for different values of the power-law exponent n and the screening potential $\Phi_{0,\text{scr}}$.

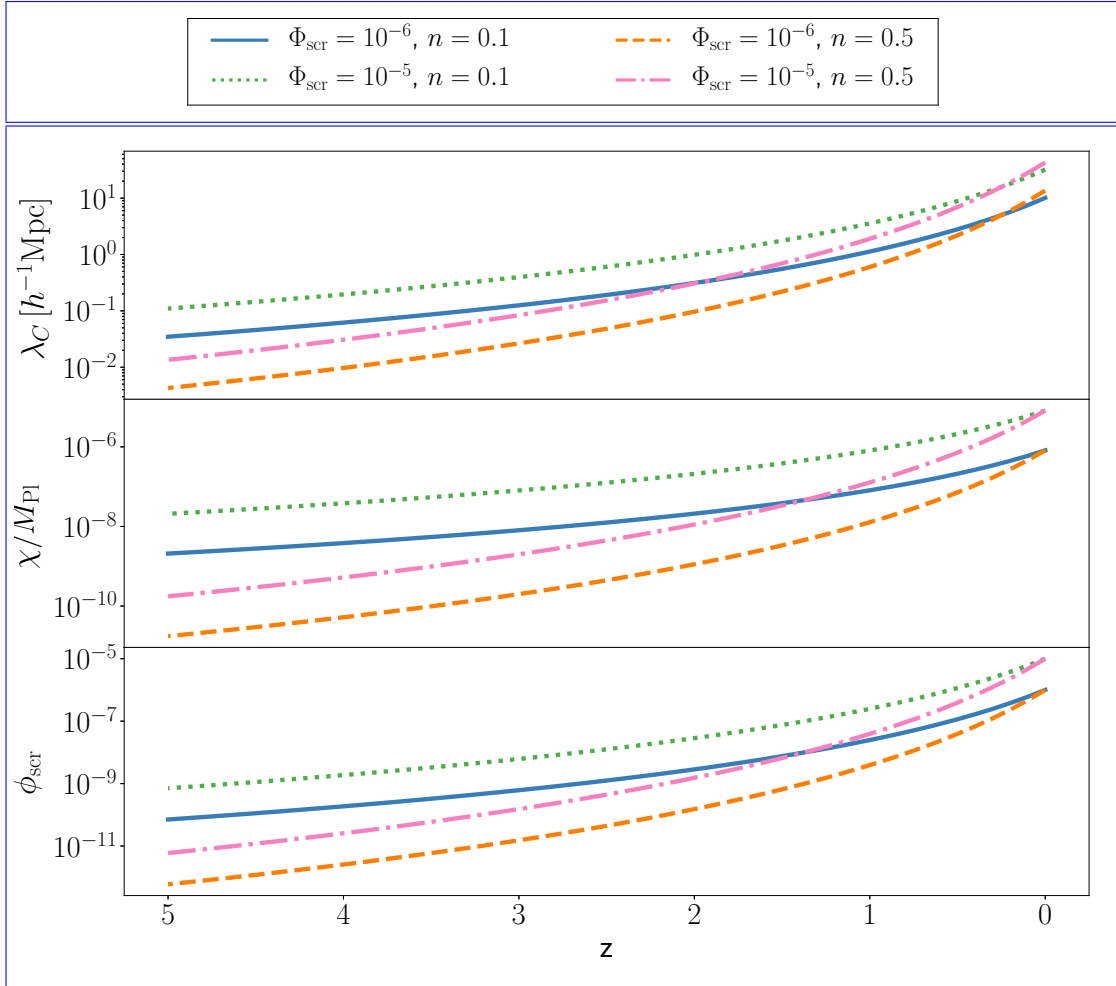


Figure 2.1: Evolution of background parameters of the chameleon field. From top to bottom: Compton wavelength λ_c , chameleon field χ_a and screening potential $\Phi_{a,\text{scr}}$.

The background value of the Compton wavelength informs us about the global behavior of the chameleon field whereas the screening potential describes its behavior locally. At high redshifts, the chameleon’s Compton wavelength is too short to have any effects – on large scales, due to its low background value, and on small scales due to a low value of the screening potential. At lower redshifts, the chameleon field starts to affect matter, initially only on small scales but with the passage of time also on large scales. We thus expect the strongest effects to be on small scales.

2.3.5 Numerical solutions

In this section, we will show the results of numerical solutions of the chameleon profile. We will solve the equations for the Hu-Sawicki $f(R)$ model, (2.52). In this section we will focus only on systems with spherical symmetry (2.36), i.e. we will solve the following equation

$$\frac{d^2\chi}{dr^2} + \frac{2}{r} \frac{d\chi}{dr} = \frac{\beta}{M_{pl}} \rho - \frac{\beta}{M_{pl}} \bar{\rho}_0 \left(\frac{\chi_0}{\chi} \right)^{1-n} \quad (2.64)$$

Our algorithm for finding solutions to (2.64) uses the shooting method (**10.5555/42249**) and is based on the original algorithm of **masterthesis`vrastil**. We further improved the code applicability, readability, and its parametrization. The code is publicly available at https://github.com/vrastil/chi_r_solver.

Stars

We will first consider a case where some approximate solutions exist – a compact spherical object of constant density ρ_c surrounded by the background of density ρ_0 as discuss in subsection 2.3.3. We expect that for low-mass objects the chameleon field will track the Newtonian potential while for massive objects the chameleon field will be frozen inside the sphere and outside it will be following the Newtonian behavior but with decreased amplitude.

In Figure 2.2 we show results for the chameleon profile. We used the notation $\tilde{\chi} \equiv (\chi - \chi_0)/2\beta M_{pl}$ for better comparison with the Newtonian potential. We see that for $\Phi_{scr} > \Phi_G$ we have an unscreened solution as expected. For lower values of Φ_{scr} the field is frozen inside the object and have lower amplitude outside the object as expected from analytical solutions.

Let us focus on the regime which cannot be treated analytical, i.e. regime between thin-shell and thick-shell solutions. This regime corresponds to the situation when the linear approximation (thick-shell) breaks down inside the object, i.e. the gravitational potential cancels screening potential somewhere inside the object. We will denote R_{eq} the *equivalence radius* – radius at which the Newtonian potential equals the screening potential $|\Phi_G(R_{eq})| = \Phi_s$. By letting the equivalence radius posses also negative values such as $(1 + |R_{eq}|/R_s)|\Phi_G(0)| = \Phi_s$ we can clearly distinguish between the linear ($R_{eq} < 0$) and the screening ($R_{eq} > 0$) regime.

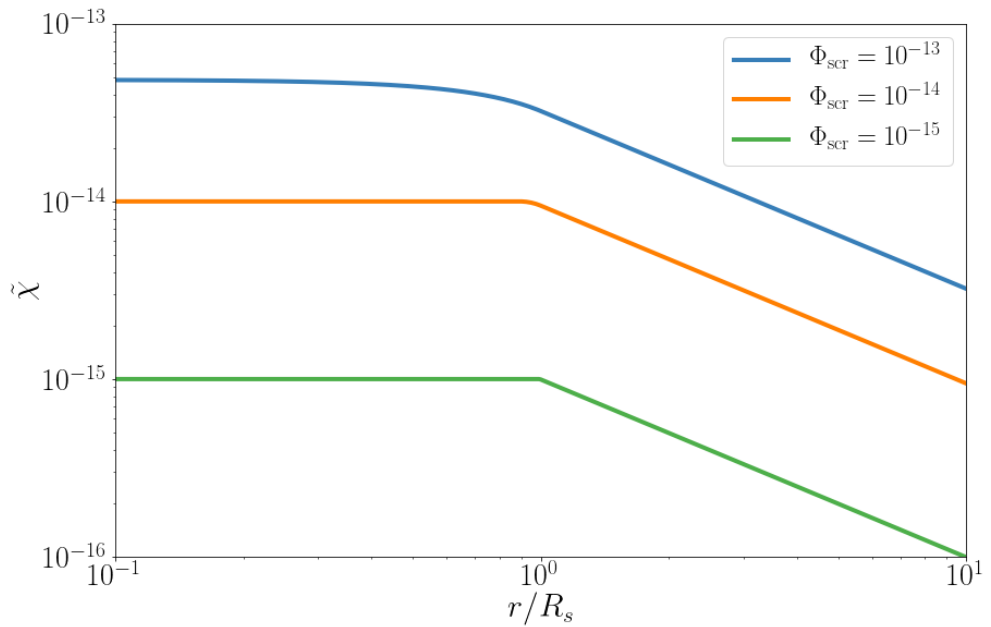


Figure 2.2: Chameleon profile for several screening potentials. The top solution is in the linear regime and is identical to the gravitational potential. The other two solutions are in the screened regime and the amplitude of the field is suppressed.

In Figure 2.3 we show the behavior of the chameleon fifth force in this regime. We see that for the linear regime the fifth force is as strong as standard gravity (up to the factor $2\beta^2$). For $R_{eq} \ll R_s$ the chameleon field manages to catch up with the linear solution inside the object and there is no screening outside. As the R_{eq} grows the field is not able to catch up with the linear solution while inside the object and the force outside is screened.

NFW Halo

The Navarro-Frenk-White (NFW) profile proposed by [1996ApJ...462..563N](#) describes the distribution of cold dark matter. The NFW profile of matter overdensity is given by

$$\delta\rho_{\text{NFW}}(r) = \frac{\rho_c}{r/r_s (1+r/r_s)^2}, \quad (2.65)$$

where ρ_c is the density scale and r_s is the scale radius. We will also be using the dimensionless radius $x \equiv r/r_s$. The total mass of the halo is divergent (logarithmically) so we take a cut-off at the radius r_{200} , which is defined as the radius at which the density is 200 times the critical density. Then the mass of the halo is

$$M_{200} = \int_0^{r_{200}} 4\pi r^2 \rho(r) dr = 4\pi \rho_c r_s^3 \left(\ln(1+c) - \frac{c}{c+1} \right), \quad (2.66)$$

where $c \equiv r_{200}/r_s$ is the concentration of the halo. For a given mass the halo is fully characterized by the concentration.

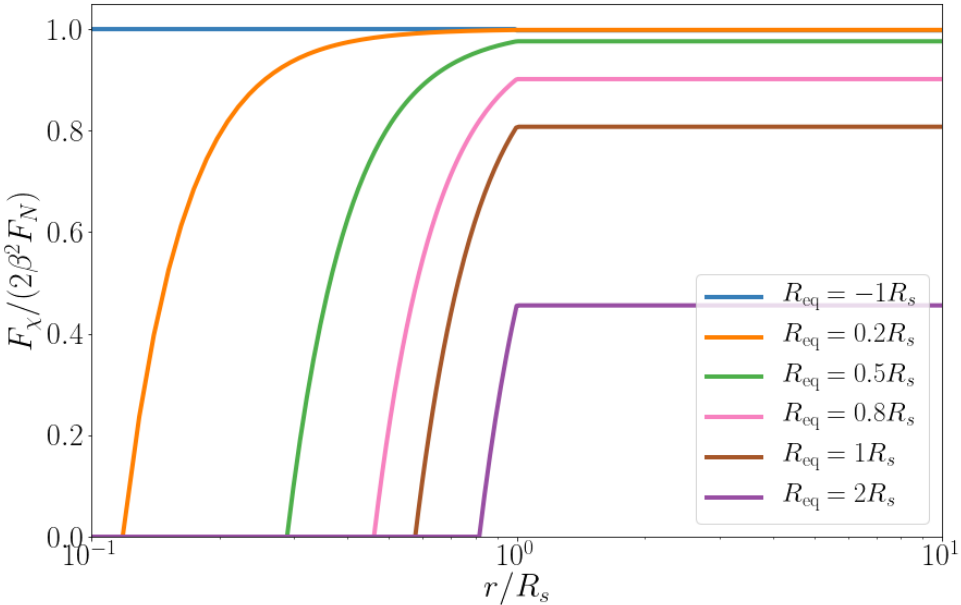


Figure 2.3: Chameleon force relative to the standard gravitational force for several screening potentials (given through the equivalence radius). For $R_{\text{eq}} \ll R_S$ there is no screening outside the object. As the R_{eq} grows the chameleon enters the screened regime.

For NFW halo the density is not constant as in the case of compact spherical objects (stars). The chameleon mass and the screened solution are therefore also not constant and one does not have analytical solutions as in the case of stars. However, for realistic halo, the density varies on scales much larger than the Compton wavelength of the chameleon. In such cases, we can treat the field as frozen in the same sense as in the case of stars. Therefore we expect the chameleon field to behave in a similar way as in the case of stars, i.e. to follow the Newtonian potential in the linear case and to have screened behavior for more massive halos.

In Figure 2.4 we show the chameleon fifth force. We see that the behavior is indeed similar to stars although the field catches up much later. This is because there is no sudden drop in density (and mass of the field) where the chameleon can start to behave as free but rather the mass is slowly dropping. This indicates that it will be much harder to detect the chameleon fifth force on scales of galaxies than for star-like objects. This is of course true only assuming the screening potential is the same on all scales.

The meaning of the screening potential and its connection to the Newtonian potential in (2.58) is given by the value of the field at the background, i.e. value that minimizes right side of (2.56). However, objects like stars or galaxy halos do not sit directly in the overall average density of the universe but rather in galaxy halo or halo of the cluster of galaxies. Therefore the value of the effective screening potential is given by the density of the background object we can consider as being in infinity relative to the scale of the studied object. In Figure 2.5 we show

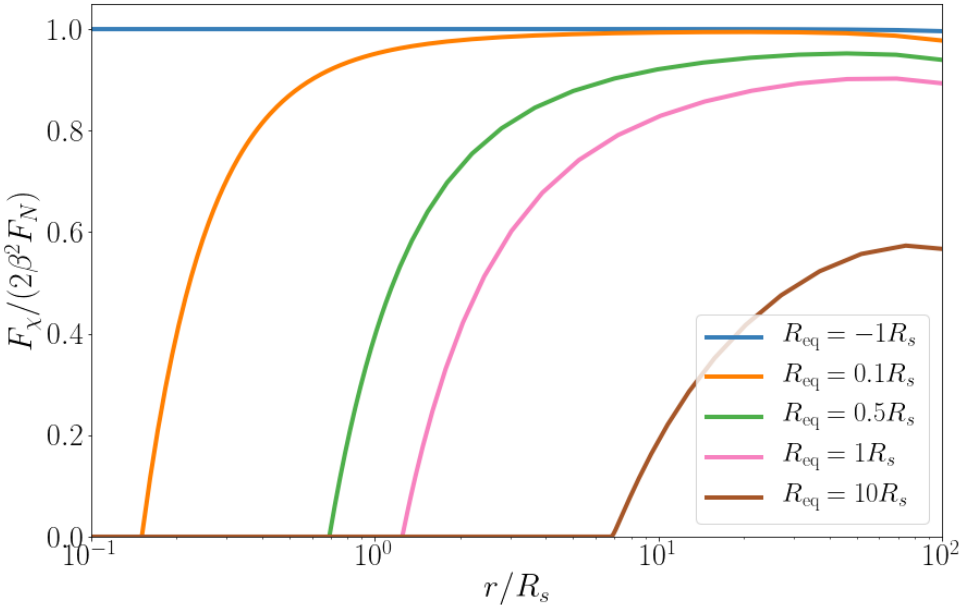


Figure 2.4: Chameleon force relative to the standard gravitational force for several screening potentials (given through the equivalence radius). For $R_{\text{eq}} \ll R_S$ there is no screening outside the object. As the R_{eq} grows the chameleon enters the screened regime.

the value of this effective screening potential for a cluster of galaxies of a typical size – $M = 10^{14} M_\odot, c = 4$. We see that the screening potential is greatly reduced in inner parts of the galaxy cluster halo. For this reason, we do not think it much likely to observe the effects of the chameleon field on scales smaller than Mpc.

As the chameleon affects only non-relativistic matter it can be detected using a combination of dynamical measurements and lensing measurements. Therefore, we considered what would be the difference between the mass distribution of a galaxy cluster measured via lensing (true mass) and via dynamics of enclosed galaxies. In Figure 2.6 we plot this ratio for five real clusters (simulated as having ideal NFW profile), see their parameters in Table 2.1, and for four different values of the screening potential. We see that except for the case $\Phi_{\text{scr}} = 1$ one would need very precise (and nowadays unrealistic) measurements of the mass distribution. We are therefore left with only cosmological scales of tens of Mpc and larger to study the chameleon. We will study this case in chapter 5.

2.4 Other theories³

In this section we briefly mention some of the other theories of modified gravity. This list is in no way complete and serves only as an example of different approaches to modifications of gravity. See references for further reading.

³Some parts of this section have already been published in [masterthesis vrastil](#).

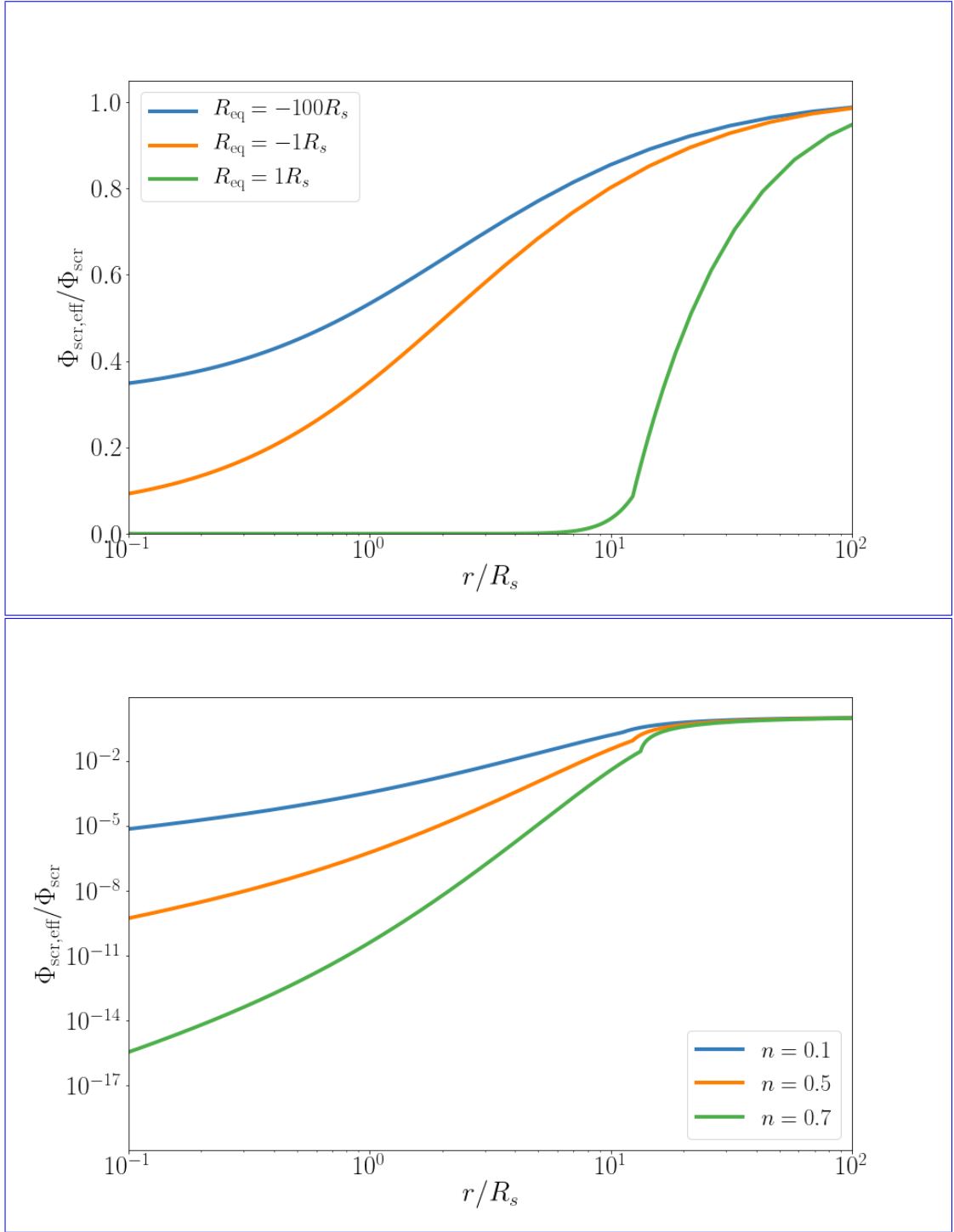


Figure 2.5: Effective screening potential relative to the screening potential for a cluster of galaxies, $M = 10^{14}M_\odot, c = 4$. The top Figure is shown for several screening potentials (given through the equivalence radius) while the bottom for different chameleon parameter n .

Cluster	c	M	Cluster	c	M
ClG 0054-27	1.2	$0.42 \cdot 10^{14}$	Cl 0016+1609	2.1	$1.12 \cdot 10^{14}$
MS 2137.3-2353	13	$2.9 \cdot 10^{14}$	ClG 2244-02	4.3	$4.5 \cdot 10^{14}$
MS 0451.6-0305	5.5	$18 \cdot 10^{14}$			

Table 2.1: Properties of clusters simulated as perfect NFW halos: concentration c and mass $M[M_\odot]$. Parameters are taken from **2007MNRAS.379..190C**

2.4.1 Quintessence

Quintessence, from the Latin “fifth element”, is according to ancient and medieval philosophy the fifth element, or ether, supposed to be the constituent matter of the heavenly bodies after air, fire, earth, and water. The name quintessence, or the Q component, was first used by **1998PhRvL..80.1582C** for the canonical scalar field ϕ evolving along a potential $V(\phi)$. Such a dynamical field can reproduce the late-time acceleration with the equation of state $w = w(t) \approx 1$. Although quintessence can alleviate the coincidence problem of dark energy via the so-called tracker solution, it still suffers by the fine-tuning problem as the potential needs to be flat enough to lead to the slow-roll inflation today with an energy scale $\rho_{DE} \simeq 10^{-120} M_{\text{pl}}^4$ and a mass scale $m_\phi \lesssim 10^{-33}$ eV. However, such fine-tuned potentials can be constructed within the framework of particle physics.

Quintessence is one of the simple models of dark energy as it is a canonical scalar field that interacts with all the other components only through standard gravity. The Lagrangian density for the quintessence field is

$$\mathcal{L}_\phi = -\frac{1}{2}(\partial\phi)^2 - V(\phi) \quad (2.67)$$

We can compute the stress-energy tensor as

$$T_{\mu\nu}^\phi \equiv \frac{-2}{\sqrt{-g}} \frac{\delta(\sqrt{-g}\mathcal{L}_\phi)}{\delta g^{\mu\nu}} = \partial_\mu\phi\partial_\nu\phi - g^{\mu\nu} \left(\frac{1}{2}(\partial\phi)^2 + V(\phi) \right). \quad (2.68)$$

Now, the energy density and pressure are given by components of the stress-energy tensor. For FLRW background and ϕ only time-dependent we get

$$\rho_\phi = -T_0^0 = \frac{1}{2}\dot{\phi}^2 + V(\phi) \quad p_\phi = \frac{1}{3}T_i^i = \frac{1}{2}\dot{\phi}^2 - V(\phi). \quad (2.69)$$

Equation of state for the quintessence is then

$$w \equiv \frac{p}{\rho} = \frac{\dot{\phi}^2 - 2V(\phi)}{\dot{\phi}^2 + 2V(\phi)}. \quad (2.70)$$

We require the condition $w < -1/3$ to realize the late-time cosmic acceleration, which translates into the condition $\dot{\phi}^2 < V(\phi)$, i.e. the potential needs to be shallow enough for the field to evolve slowly along the potential. For a slow-rolling field such as $\dot{\phi} \ll V(\phi)$ equation of state (2.70) reduce to $w \approx -1$ as indicated by cosmological measurements.

The variation of (2.67) with respect to ϕ gives us the equation of motion for the scalar field ϕ

$$\ddot{\phi} + 3H\dot{\phi}^2 + V_{,\phi} = 0. \quad (2.71)$$

Depending on which term and when determines the evolution of the field, the quintessence models have been dynamically classified into *freezing* models and *thawing* models (**2005PhRvL..95n1301C**). In the freezing models the field was rolling along the potential in the past, but the movement gradually slows down as the field approaches the minimum of the potential ($\dot{\phi} \rightarrow 0$) and the system enters the phase of the cosmic acceleration ($w \rightarrow -1$). In the thawing models, the field was initially frozen ($\dot{\phi} \approx 0$) in the early matter era because of the Hubble friction (the term $H\dot{\phi}$) until recently and then it begins to evolve once H drops below m_ϕ and w evolves from -1 .

A potential of the freezing models is for example

$$V(\phi) = M^{4+n}\phi^{-n} \quad (n > 0), \quad (2.72)$$

which appears in the fermion condensate model as dynamical supersymmetry breaking (**1999PhRvD..60f3502B**). This potential does not possess a minimum and hence the field rolls down the potential toward infinity. Another example of potential in the freezing models is

$$V(\phi) = M^{4+n}\phi^{-n} \exp(\alpha\phi^2/M_{\text{pl}}^2), \quad (2.73)$$

which can be constructed in the framework of supergravity (**1999PhLB..468...40B**). This potential has a minimum at which the field is eventually trapped (corresponding to $\dot{\phi} = 0$ and hence $w = -1$).

The broader class of potentials belonging to the thawing models are so-called hilltop quintessence models (**2008PhRvD..78l3525D**), in which the scalar field is rolling near a local **maximum** in the potential but it begins to roll down around the present. A particular example that is well-described by this model is the pseudo-Nambu-Goldstone Boson (PNGB) model of **1995PhRvL..75.2077F**, for which the potential is given by

$$V(\phi) = M^4 [\cos(\phi/f) + 1]. \quad (2.74)$$

2.4.2 K-essence

Quintessence models are based on a scalar field with a canonical kinetic term and a slowly varying potential. However, in the context of particle physics there appear scalar fields with non-canonical kinetic terms. In **1999PhLB..458..209A** it is shown that a large class of scalar fields with non-canonical kinetic terms can, without the help of potential terms, drive an inflationary evolution starting from rather generic initial conditions. The Lagrangian density for the k-essence is

$$\mathcal{L}_K = P(\phi, X), \quad (2.75)$$

where $X = -\frac{1}{2}(\partial\phi)^2$ is the canonical kinetic energy and the function $P(\phi, X)$ must vanish for $X \rightarrow 0$ (otherwise there would be some potential term).

The energy-momentum tensor of the k-essence is given by

$$T_{\mu\nu}^K \equiv \frac{-2}{\sqrt{-g}} \frac{\delta(\sqrt{-g}\mathcal{L}_K)}{\delta g^{\mu\nu}} = P_{,X} \partial_\mu \phi \partial_\nu \phi + g^{\mu\nu} P, \quad (2.76)$$

which is of the form of a perfect fluid, $T_{\mu\nu} = (\rho+p)u_\mu u_\nu + g_{\mu\nu}p$, with a four-velocity $u_\mu = \partial_\mu \phi / \sqrt{2X}$, pressure $p_K = P$ and energy density

$$\rho_K = 2XP_{,X} - P. \quad (2.77)$$

The equation of state of the k-essence is then

$$w_K = \frac{p_K}{\rho_K} = \frac{P}{2XP_{,X} - P}, \quad (2.78)$$

which is $w_K \approx -1$, as long as the condition $XP_{,X} \ll P$ is satisfied.

In the low-energy effective string theory appear higher-order derivative terms coming from α' and loop corrections to the tree-level action (**2003PhR...373....1G**). The k-essence action for these theories is for example

$$P = K(\phi)X + L(\phi)X^2. \quad (2.79)$$

Phantom or ghost scalar fields with a negative kinetic energy $-X$ and $w \lesssim -1$ can also fit the current observations. These ghost fields generally suffer from a quantum instability problem unless higher-order terms in X or ϕ are taken into account in the Lagrangian density (**2010det0.book.....A**). The action of the so-called dilatonic ghost condensate model is (**2004JCAP...07..004P**)

$$P = -X + e^{\kappa\lambda\phi}X^2/M^4. \quad (2.80)$$

2.4.3 Gauss-Bonnet Dark Energy Models

In $f(R)$ gravity one adds the general function of the Ricci scalar. But in principle, one can add general functions of the Ricci and Riemann tensors as well, e.g. $f(R, R_{\mu\nu}R^{\mu\nu}, R_{\alpha\beta\gamma\delta}R^{\alpha\beta\gamma\delta}, \dots)$ (**2005PhRvD..71f3513C**). These Lagrangians are generally plagued by the existence of ghosts. However, there exists a combination of Ricci and Riemann tensors that keeps the equations at second-order in the metric and does not necessarily give rise to instabilities – so-called Gauss-Bonnet term \mathcal{G} coupled to a scalar field

$$\mathcal{G} \equiv R^2 - 4R_{\mu\nu}R^{\mu\nu} + R_{\alpha\beta\gamma\delta}R^{\alpha\beta\gamma\delta}. \quad (2.81)$$

The Gauss-Bonnet term is the unique invariant for which the highest (second) derivative occurs linearly in the equations of motion and thus ensuring the uniqueness of solutions. The Gauss-Bonnet term naturally arises as a correction to the tree-level action of low-energy effective string theories (**2000PhR...337..343L**). The starting action is given by

$$S = \int d^4x \sqrt{-g} \left[\frac{M_{pl}^2}{2} R - \frac{\gamma}{2} (\nabla\phi)^2 - V(\phi) + f(\phi)\mathcal{G} \right], \quad (2.82)$$

where $\gamma = \pm 1$ (+1 for the canonical scalar). For more details see **2005PhRvD..71l3509N**; **2006JCAP...06..004N**; **2013PhRvD..87h4037C**.

2.4.4 Braneworld Models

In the braneworld model of Dvali, Gabadadze, and Porrati (**2000PhLB..485..208D**) the 3-brane is embedded in a Minkowski bulk spacetime with infinitely large extra dimensions. The theory gives rise to the correct 4D potential at short distances whereas at large distances the potential is that of a 5D theory. The action of the theory is

$$S = \frac{M_{(5)}^3}{2} \int d^5X \sqrt{-\tilde{g}} \tilde{R} + \frac{M_{pl}^2}{2} \int d^4x \sqrt{-g} R + \int d^4x \sqrt{-g} \mathcal{L}_m, \quad (2.83)$$

where $g_{AB}(X) = g_{AB}(x, y)$ denotes a 5D metric for which the 5D Ricci scalar is \tilde{R} and $M_{(5)}$ is the 5D Planck mass. Capital letters are used for 5D quantities ($A, B = 0, 1, 2, 3, 5$). The brane is located at $y = 0$. The induced 4D metric on the brane is denoted by

$$g_{\mu\nu}(x) \equiv \tilde{g}_{\mu\nu}(x, y = 0). \quad (2.84)$$

The cross-over scale r_0 is defined by

$$r_0 \equiv \frac{M_{pl}^2}{2M_{(5)}^3}. \quad (2.85)$$

At short distances $r \ll r_0$ gravity behaves as usual 4D theory, i.e the gravitational potential has correct $1/r$ behavior (except small logarithmic repulsion term). On the other hand at large distances $r \gg r_0$ the potential scales as $1/r^2$ according to the laws of 5D theory.

The presence of the extra dimension has severe consequences on the cosmology as well. It can be shown (**2010deto.book.....A; 2009PhLB..674..237M**) that the matter-dominated Universe approaches the de Sitter solution $H = r_0^{-1}$. This cosmological solution drives our Universe into the self-inflationary regime without dark energy. From $H_0 \approx r_0^{-1}$ we get $M_{(5)} \approx 10 - 100$ MeV.

2.4.5 Massive Gravity

The idea to give a mass to the graviton (infrared modification of gravity) is not new and has been investigated since the first years of General Relativity. It is a less minimal theory than $f(R)$ theories or modified gravities with an extra scalar field because it introduces three new degrees of freedom rather than one. By giving a mass m to the graviton we deform the classical potential to the Yukawa profile $\sim \frac{1}{r} e^{-mr}$ which departs from the classical one at distances $r > 1/m$. By choosing the graviton mass to be of the order of the Hubble constant $m \sim H$ one can hope to explain the acceleration of the universe without dark energy.

The simplest theory for a non-self-interacting massive graviton is the Fierz-Pauli theory of **1939RSPSA.173..211F**. The action for a single massive spin 2 particle in flat space, carried by a symmetric tensor field $h_{\mu\nu}$ is

$$\begin{aligned} S = \int d^4x & \left[-\frac{1}{2} \partial_\lambda h_{\mu\nu} \partial^\lambda h^{\mu\nu} + \partial_\mu h_{\nu\lambda} \partial^\nu h^{\mu\lambda} - \partial_\mu h^{\mu\nu} \partial_\nu h \right. \\ & \left. + \frac{1}{2} \partial_\lambda h \partial^\lambda h - \frac{1}{2} m^2 (h_{\mu\nu} h^{\mu\nu} - h^2) \right] + S_m. \end{aligned} \quad (2.86)$$

Any other combination of $h_{\mu\nu}h^{\mu\nu}$ and h^2 would lead to instabilities. Varying the action with respect to $h_{\mu\nu}$ yields the equation of motion

$$R_{\mu\nu} - \frac{1}{2}Rg_{\mu\nu} + \frac{1}{2}m^2(h_{\mu\nu} - h\eta_{\mu\nu}) = \frac{1}{M_{\text{pl}}^2}T_{\mu\nu}, \quad (2.87)$$

where all quantities are linearized around $\eta_{\mu\nu}$.

Because of the so-called vDVZ discontinuity (“van Dam-Veltman-Zakharov”) in the propagator of a graviton, the Fierz-Pauli theory leads to different physical predictions from those of GR regardless the mass of the graviton (even when $m \rightarrow 0$). The Vainshtein mechanism (**1972PhLB...39..393V**) allows in principle to get rid of the vDVZ discontinuity by introducing non-linear Fierz-Pauli gravity.

The Vainshtein mechanism is another example of the screening mechanism and restores the continuity with GR on scales below the so-called Vainshtein radius r_V , defined as

$$r_V \equiv (GM/m^4)^{1/5}. \quad (2.88)$$

Much below the Vainshtein radius, which grows as the graviton’s mass approaches 0, only linear terms play a crucial role and the GR is restored.

For more about the massive gravity and the Vainshtein mechanism see e.g. **2013CQGra..30r4001B; 2012RvMP...84..671H**.

2.4.6 Acceleration without Dark Energy

So far we studied some kind of dark energy – either in the form of an exotic matter or by modifying gravity itself. But this need for dark energy as an explanation of the acceleration comes from our observations which are based on the presumption of the homogeneous and isotropic Universe. What we observe are different expansion rates at different distances rather than an increase in the expansion rate at all distances. But this can be caused by strong inhomogeneities in the distribution of matter rather than by an accelerating Universe.

Void models

The basic idea behind void models is that we live in the middle of a huge spherical region which is expanding faster because it is emptier than the outside. That means that the Universe as a whole does not accelerate but that we observe an *apparent* cosmic acceleration. The edge of this void should be located around $z \sim 0.3 - 0.5$, the value at which in the standard interpretation we observe the beginning of the acceleration. These models are described by the Lemaître-Tolman-Bondi (LTB) spherically symmetric metric – the generalization of a FLRW metric in which the expansion factor along the radial coordinate is different relative to the surface line element $d\Omega^2$ (**2013JCAP...02..047D; 2006PhRvD..73h3519A**).

The inhomogeneous LTB model matches to the supernovae data and the location of the first acoustic peak of the CMB temperature power spectrum but cannot satisfactorily reproduce the entire CMB angular power

spectrum ([2011JCAP...02..013C](#)). The observed isotropy of the CMB radiation implies that we must live close to the center of the void – nearer than 15 Mpc ([2006PhRvD..74j3520A](#)). Moreover, there is no valid mechanism at present to explain the formation of such huge inhomogeneities, let alone one with our Galaxy near the center.

Backreaction

Unlike the void models, which regard the acceleration as an apparent one, *backreaction* models try to explain the cosmic acceleration by arranging inhomogeneities so that the deviation from the FLRW metric can produce a real acceleration ([2011CQGra..28w5002S](#); [2004JCAP...02..003R](#); [2005PhRvD..72b3507M](#)). Because GR equations are non-linear, averaging the inhomogeneities and then solving the GR equations (which is the usual approach) is not the same as first solving the full (inhomogeneous) GR equations and then averaging them – the expected value of a non-linear function is not the same as the non-linear function of the expected value.

Any large inhomogeneities must be concealed from our sight to fit observations. Strong peculiar velocities instead of strong density fluctuations can do this job, but there are strong constraints on peculiar velocities from e.g., the kinematic Sunyaev–Zel’dovich effect. Moreover, the accompanying anisotropy is another source of observable effects difficult to accommodate with current observations.

2.5 Parametrization of models

We saw in the previous chapter that at the background level the evolution is governed by Friedman equations (1.6) – (1.8) and consequently omega parameters (1.11) and Hubble parameter H which can be obtained, e.g., from distance measurements. As we discussed, the cosmological constant is not the only possible explanation of the accelerated expansion and the equation of state w of dark energy does not have to be exactly $w = -1$. For the arbitrary equation of state $w_{DE} = p_{DE}/\rho_{DE}$ in the flat Universe with a negligible contribution of radiation we can obtain the following equation

$$w_{DE}(z) = \frac{(1+z)(E^2(z))' - 3E^2(z)}{3[E^2(z) - \Omega_{m,0}(1+z^3)]}, \quad (2.89)$$

where a prime denotes derivative with respect to z . We see that w_{DE} cannot be determined solely from $E(z)$ (obtainable through distance measurements) and we need also present density of matter $\Omega_{m,0}$. However, if we parametrize w_{DE} in some way as it is usually done through measurements of $E(z)$ at several redshifts we can constraint both w_{DE} and $\Omega_{m,0}$.

Several parametrization of w_{DE} have been proposed so far. We can write such parametrization in the form

$$w_{DE} = \sum_{n=0} w_n x_n(z), \quad (2.90)$$

where he expansions can be given by

$$(i) \text{Redshift :} \quad x_n(z) = z^n, \quad (2.91)$$

$$(ii) \text{Scalefactor :} \quad x_n(z) = (1-a)^n = \left(\frac{z}{1+z} \right), \quad (2.92)$$

$$(iii) \text{Logarithmic :} \quad x_n(z) = [\ln(1+z)]^n. \quad (2.93)$$

Parametrization (ii) is usually written for $n \leq 1$ as $w = w_0 + w_a(1-a)$.

For the generic $f(R)$ gravity, the equation of state is given by
(2013qopu.conf...73B)

$$w_{DE} = \frac{-(1/2)(F_{,R}R - F) + \ddot{F}_{,R} + 2H\dot{F}_{,R} - (1 - F_{,R})(2\dot{H} + 3H^2)}{(1/2)(F_{,R} - F) - 3H\dot{F}_{,R} + 3(1 - F_{,R})H^2}, \quad (2.94)$$

which then can be compared with observations (2.89). For different examples of evolution of w_{DE} see, e.g., **2020arXiv200707717A**.

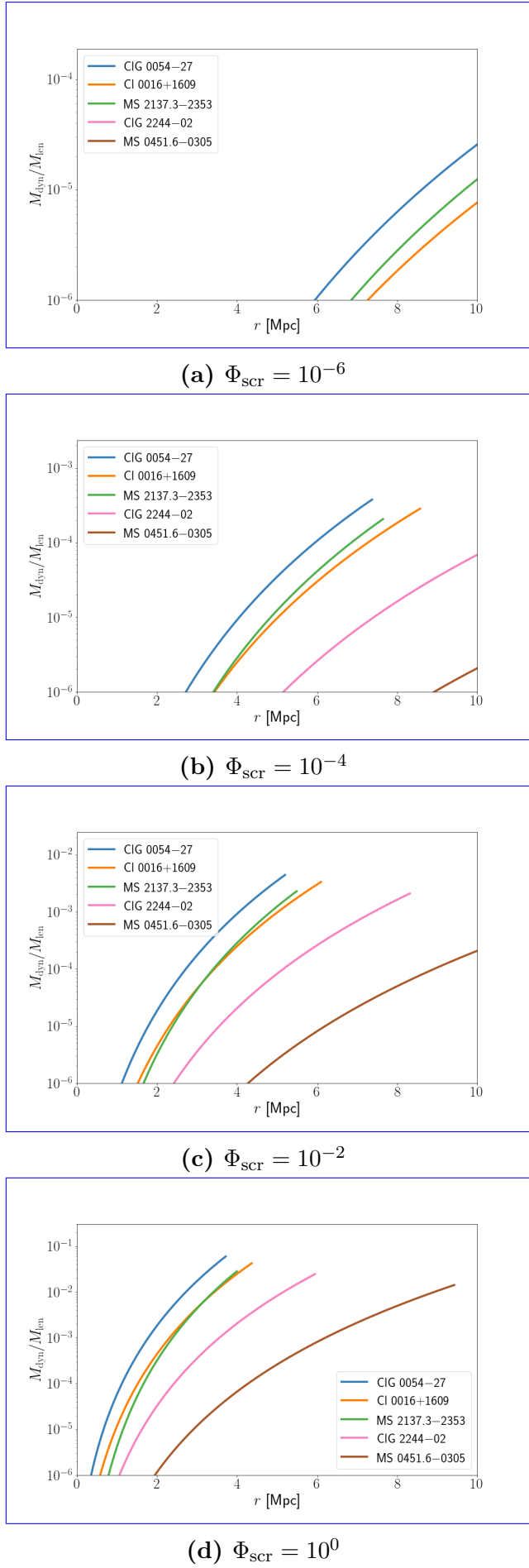


Figure 2.6: Effective dynamical mass of the clusters relative to the actual (lensing) mass of the cluster. Cluster properties are shown in Table 2.1.

3. Cosmological Simulations

In this chapter, we will describe methods and techniques that are used for studying our Universe on the largest scales by using numerical simulations. We will describe how we implemented these methods in our code for N -body simulations .

In this chapter we will use the following notation: box size L [$h^{-1}\text{Mpc}$], number of particles N_p , number of force mesh points N_f , number of power spectrum mesh points N_a , number of runs N , number of time-steps N_t , and a derived parameter, the particle mass m [M_\odot]. This notation is summarized in Table 3.1.

3.1 N -body problem

Many problems in physics, including cosmology, involve particle systems with each particle interacting with all other particles present. In astronomy, there is a gravitational interaction between stars, galaxies, and cluster of galaxies, depending on the scale which we are studying. The challenge of efficiently carrying out the related calculations is generally known as the N -body problem.

The main problem is the following – we have N_p particles all interacting gravitationally with each other. To compute a trajectory of even a single particle involves computing trajectories of all other particles as the gravitational force is dependent on time-varying positions of other particles. That means that at each time-step we have to compute forces from all other N_p particles and we need to compute these forces for each of N_p particles. This leaves us with complexity of $\mathcal{O}(N_p^2)$. This brute force approach can be used only for small systems and is computationally unimaginable for large systems in cosmology which typically involve $N_p \sim 10^9$ particles.

This direct approach is generally referred to as the Particle–Particle (PP) method (**Hockney:1988:CSU:62815**). Although computationally expensive

Symbol	Definition
L	box size in units of $h^{-1}\text{Mpc}$
N_p	number of particles
N_f	number of force mesh points
N_a	number of power spectrum mesh points
N	number of runs
N_t	number of time-steps
m	particle mass in units of $[M_\odot]$

Table 3.1: Summary of symbols used for simulation parameters.

the accuracy in the force calculation is of machine precision. To be able to simulate large systems of particles we need to drop the accuracy of continuous positions and use discrete positions for force calculations. In our code, we use two main methods for force calculations – the Particle-Mesh algorithm (PM) and grid-based methods, both of them we describe in more detail below.

3.1.1 Time integration

Accurate time integration is a very important part of any N -body simulation. While there are many different methods to integrate particle trajectories (**Hockney:1988:CSU:62815**) we describe here one of the most used ones in collisionless simulations – the Leapfrog integrator.

The leapfrog integrator ~~is an example of a symplectic integrator~~^{belongs to a class of symplectic integrators} (2011EPJP..126...55D). Symplectic integrators ~~exactly solve an approximate Hamiltonian. As a consequence, the numerical time evolution is a canonical map and preserves certain conserved quantities exactly, are canoncial transformations and as such, they conserve certain quantities~~ such as the total angular momentum, the phase-space volume, and the Jacobi constants. ~~The idea is to approximate the Hamiltonian H governing motion of particles with an approximate one~~ Instead of solving the exact Hamiltonian approximately, the leapfrog integrator tries to solve an approximate Hamiltonian exactly

$$\tilde{H} = H + H_{\text{err}}, \quad (3.1)$$

where H_{err} is the error Hamiltonian. ~~Provided that If~~ \tilde{H} and H are time-invariant~~do not dependent explicitly on time~~, the energy error~~error in energy~~ is bounded at all times. ~~The goal now is to find We want to find such a~~ \tilde{H} that can be solved ~~exactly by simple numerical means~~ easily by numerical methods and simultaneously and minimizes H_{err} . Defining the combined phase-space coordinates $w \equiv (x, p)$ ~~the~~ The Hamilton's equations are

$$\dot{w} = \mathcal{H}w, \quad (3.2)$$

where $w \equiv (x, p)$ are combined phase-space coordinates and $\mathcal{H} \equiv \{\cdot, H\}$ is an operator acting on w through Poisson bracket. Hamilton's equations have then the formal solution

$$w(t + \Delta t) = e^{\Delta t \mathcal{H}} w(t). \quad (3.3)$$

~~The We want to split the~~ operator $e^{\Delta t \mathcal{H}}$ ~~can be split~~, in an approximate sense, into a succession of discrete but symplectic steps, each of which can be exactly integrated. The most common choice is to separate out (approximately) into steps that, individually, can be integrated exactly. This is usually done by separating the Hamiltonian into the kinetic and potential energies, $H = T(p) + V(x)$, such that we can split ~~That we can write~~

$$e^{\Delta t \mathcal{H}} = e^{\Delta t(\mathcal{T} + \mathcal{V})} \approx e^{\frac{1}{2}\Delta t \mathcal{V}} e^{\Delta t \mathcal{T}} e^{\frac{1}{2}\Delta t \mathcal{V}}, \quad (3.4)$$

where operators $\mathcal{T} \equiv \{\cdot, T\}$ and $\mathcal{V} \equiv \{\cdot, V\}$ are known as drift and kick, as they only change either the positions (drift) or velocities (kick). Because these operators are non-commutative, the central relation in (3.4) is only approximately true. This operator splitting is extremely useful because the new equations have a simple solution:

$$e^{\Delta t \mathcal{T}} \begin{pmatrix} x \\ p \end{pmatrix} = \begin{pmatrix} x + \Delta t p \\ p \end{pmatrix} \quad \text{and} \quad e^{\Delta t \mathcal{V}} \begin{pmatrix} x \\ p \end{pmatrix} = \begin{pmatrix} x \\ p - \Delta t \nabla V \end{pmatrix}. \quad (3.5)$$

The splitting (3.4), also known as kick-drift-kick (DKK), is second-order accurate, whereas simpler splitting only into one kick and one drift is first-order accurate. The same accuracy and results have also similar splitting into drift-kick-drift which we use in our integrator.

3.2 Particle-Mesh algorithm

As we mentioned in the introduction, in order to effectively compute forces on particles one has to abandon the continuous position and solve the forces using discretized positions. The idea of the PM method is that we set up a mesh (grid) over the computational box, and then we solve the gravitational potential (i.e. Poisson's equation (1.44)) at the mesh-points (**nbodyLindholm**). Forces at the mesh-points can then be obtained by calculating the gradient of the potential. The four principal steps of the particle-mesh calculation are (**Hockney:1988:CSU:62815**):

1. assign mass to the mesh,
2. solve the field equation on the mesh,
3. calculate the mesh-defined force field,
4. interpolate to find forces on the particles,

where the forces found at the last step are used to integrate the equations of motion.

3.2.1 Assignment schemes

In step 1 and 4 we make a connection between discrete mesh and continuous positions of the particles. In the first, we need to distribute the mass of all particles onto the mesh and in the last step, on the contrary, we need to interpolate forces known on the discrete mesh onto particles with continuous positions. ~~There are several ways of assigning the particle masses~~ We can assign the masses of particles to the discrete density function δ and the discrete force $-\nabla \Phi$ to the particles in several ways:

Nearest gridpoint (NGP)

The mass of each particle m_i is assigned as a whole to the gridpoint closest to the particle. Similarly, the force on particles is given by force on the nearest gridpoint. Although computationally the simplest, NGP as a zero-order interpolation offers lowest accuracy, and the interparticle force changes discontinuously as particles cross cell boundaries.

Cloud-in-Cell (CIC)

The mass of each particle is weighted over the eight closest cells while the weighting in each dimension is proportional to the distance between the particle and the mesh. CIC scheme is more costly in terms of the number of arithmetic operations per particle per timestep than NGP but offers better accuracy as first-order (linear) interpolation. The CIC interpolation function in one dimension is

$$w(x - x_p) = \begin{cases} 1 - \frac{|x - x_p|}{H} & |x - x_p| < H \\ 0 & \text{otherwise} \end{cases} \quad (3.6)$$

where x is the position of a mesh point, x_p position of the particle, and H the distance between mesh points. The three-dimensional interpolation function is $W(\mathbf{x}) = w(x_1)w(x_2)w(x_3)$. The CIC scheme is somewhere in the middle between oversimplistic NGP and higher-order interpolations which offer greater accuracy and smoother transitions but at the cost of much greater computational resources – second-order interpolation (triangular shaped cloud, TSC) involves 27 cells, third-order 64, etc. ~~CIC gives a much smoother force than The piecewise linear force of the CIC is much smoother than that of the NGP scheme (piecewise linear) and. It also~~ reduces the amplitude of fluctuations in the interparticle forces ~~as when~~ the particles are displaced with respect to the mesh. In our code, we use the CIC scheme. ~~Mixed schemes The NGP and CIC schemes both employ mass assignment functions which are the same as their force interpolation functions. A result of this symmetry is that they conserve momentum, i.e., the forces between a pair of particles are equal and opposite, and the force of a particle upon itself (the self-force) is zero. A possible variation is to use a mass assignment function which is different from the force interpolation function. In such cases, symmetry still causes the force between pairs of particles to be equal and opposite, but no longer ensures that the self force is zero. At best, the presence of the self-force presents a nonphysical restriction on the timestep and, at worst, it is disastrous.~~

3.2.2 Solution of the field equations

An efficient method for the solution of the field equations is a necessary requirement for the practical implementation of the particle simulation algorithms that have been described. For linear Poisson's equation (1.44) the most used method is the Fast Fourier Transformation which can compute convolutions involved in the force computation rapidly with the complexity of $\mathcal{O}(N_m \log N_m)$.

The FFT also automatically solves periodic boundary conditions usually incorporated in cosmological simulations to enforce homogeneity and isotropy of the Universe. Therefore, FFT-based methods are predominantly used with cosmological simulations.

The Green's function $G(k)$ of (1.44) is not the expected one, $-1/k^2$, but we have the freedom to choose such a Green's function which will minimize errors introduced by all the steps involved in force calculation – mass assignment, potential solver, finite difference and force interpolation. This topic is in great detail studied in **Hockney:1988:CSU:62815**.

3.2.3 Particle-Particle Particle-Mesh algorithm

The PM methods are excellent for solving long-range forces between particles as these methods are very fast and accurate. However, this accuracy is limited by the mesh size H , and PM algorithms cannot truly describe anything below this scale. The accuracy is given by the Nyquist wavelength $\lambda_N = 2H$, which is the shortest spatial wavelength that can be accurately recovered. Similarly, power on wavenumbers larger than the Nyquist wavenumber $k_N = 2\pi/\lambda_N = N_m\pi/L$ will be aliased into longer waves. To overcome these limitations Particle-Particle Particle Mesh algorithms (P^3M) have been proposed **hockney:10000:1973**.

~~The essence of the method is to express In the P^3M algorithm, one writes~~ the interparticle force as the sum of ~~two parts;~~ the short-range ~~part~~force, which is ~~nonzero only for particle separations less than~~ limited by some cutoff radius, and the ~~smoothly varying long-range part, which has a transform which~~ long range force, which varies smoothly and is approximately band-limited (that is to say, is approximately nonzero for only a limited range of k). The ~~total~~ short-range force on a particle is computed by direct particle-particle (PP) ~~pair~~ force summation and the ~~smoothly varying part is approximated by~~ longe-range ~~force is computed using~~ the particle-mesh (PM) ~~force calculation~~algorithm.

We do not use P^3M in our approximate methods because of their much greater numerical requirements compared to simpler PM methods. For more details, see e.g. **Hockney:1988:CSU:62815**.

3.3 Multi-grid techniques

Practical multi-grid techniques were introduced by **10.2307/2006422**. These methods also ~~interpolate the density and potential between grid and particles use~~ the discrete grids and continuous particles positions as PM methods based on FFT with $\mathcal{O}(N_m \log N_m)$ complexity but they use relaxation methods such as Gauss-Seidel iteration (**doi:10.1002/zamm.19720520813**) and can solve elliptic partial differential equations using $\mathcal{O}(N_m)$ operations. The ~~numerical coefficients in these estimates are such that multigrid methods are comparable to the rapid methods in execuation speed. Unlike the speed of these methods is comparable to the PM and other rapid methods, however, but~~ the multigrid methods can also solve general elliptic equations with nonconstant coefficients ~~with hardly any loss of efficieney~~. Even non-linear equations of modified gravitational can be solved with these methods (**10.5555/42249**).

The basic idea principle of the multigrid methods is based on the fact that on a coarser, than on a smaller (coarser) grid, we can achieve an approximate solution with small long-range errors faster than on a bigger (finer) grid. Relaxation occurs faster because information travels faster. The distribution of errors (the difference between the actual density source and that obtained via the discretization of potential from the current estimate for the potential) is first smoothed on the finest grid by a few. The problem is sequentially transferred to coarser and coarser grids, each time smoothing the errors via a few Gauss-Seidel iterations. After transferring the problem to a coarser grid, the process is repeated on coarser and coarser grids until convergence, until the convergence on the coarsest grid is achieved. Then the problem is then transferred back to finer and finer grids, each time iterating until convergence (2011EPJP..126..55D).

3.3.1 Simple two-grid V-cycle

The key idea of the multigrid method can be understood by considering the simplest case of a two-grid method. Suppose we are trying to solve the discretized linear elliptic problem on a uniform grid with mesh size h

$$\mathcal{L}_h u_h = f_h, \quad (3.7)$$

where \mathcal{L} is some linear elliptic operator and f is the source. The error or correction of the (exact) solution u_h to some approximate solution \tilde{u}_h is

$$v_h \equiv u_h - \tilde{u}_h. \quad (3.8)$$

The residual or defect is

$$d_h \equiv \mathcal{L}\tilde{u}_h - f_h. \quad (3.9)$$

Since \mathcal{L}_h is linear, the error satisfies

$$\mathcal{L}_h v_h = -d_h. \quad (3.10)$$

To find v_h we need to make an approximation to \mathcal{L}_h . This can be done using classical iteration methods, such as Jacobi or Gauss-Seidel, which use a simpler operator than \mathcal{L}_h , e.g. only the diagonal part (Jacobi iteration) for the Jacobi iteration, or the lower triangle (for the Gauss-Seidel iteration).

Instead of using a simpler form of \mathcal{L}_h we can use a coarser form, i.e. we will solve the problem using \mathcal{L}_H on a coarser grid with $H = 2h$. The residual equation (3.10) is now approximated by

$$\mathcal{L}_H v_H = -d_H. \quad (3.11)$$

Since \mathcal{L}_H has a smaller dimension this equation can be solved much faster than the original fine-grid solution. To transform residuals from fine to the coarse grid

we need a restriction operator \mathcal{R} , and similarly, we need a prolongation operator \mathcal{P} to interpolate corrections from coarse to the fine grid.

$$d_H = \mathcal{R}d_h, \quad (3.12)$$

$$\tilde{v}_h = \mathcal{P}\tilde{v}_H, \quad (3.13)$$

where \tilde{v}_H is some approximate solution of (3.11). The new approximation \tilde{u}_h^{new} is then obtained as

$$\tilde{u}_h^{\text{new}} = \tilde{u}_h + \tilde{v}_h. \quad (3.14)$$

The idea behind multigrid techniques is a combination of smoothing on the fine grid (relaxation) and on the coarse grid (coarse-grid correction). Relaxation can rapidly reduce high-frequency errors but low-frequency errors tend to converge slowly. On the other hand, high-frequency errors are not even representable on the coarse grid and low-frequency errors converge much quickly. The whole scheme, two-grid V-cycle, is thus:

- Apply a relaxation method to \tilde{u}_h (pre-smoothing),
- Compute the defect on the fine grid from (3.9),
- Restrict the defect by (3.12),
- Solve (3.11) on the coarse grid,
- Interpolate the correction to the fine grid by (3.13),
- Compute the next approximation by (3.14),
- Apply a relaxation method to \tilde{u}_h^{new} (post-smoothing).

To achieve the full multigrid method is now straightforward. Instead of solving the coarse-grid defect exactly, we can get an approximate solution ~~of it~~ by introducing an even coarser grid and so on.

We considered \mathcal{L} to be a linear operator but the above method works also with non-linear operators. The speed of convergence is obviously worse and depend on the exact form of the operator. For our problem and finding solutions to the chameleon equation of motion (2.52) this method proves to be sufficient.

Gauss-Seidel relaxation

The most popular smoothing method is Gauss-Seidel relaxation. The Gauss-Seidel scheme for N_m mesh points is

$$u_i^{\text{new}} = u_i - \left(\sum_{j \neq i}^{N_m} L_{ij} u_j - f_i \right) \frac{1}{L_{ii}}, \quad (3.15)$$

where new values of u are used on the right-hand side as they become available. It is usually best to use the tile scheme, making one pass through the mesh updating the even points and another pass updating the odd points.

For non-linear problems as ours, one needs to modify the scheme (3.15) by Newton iteration

$$u_i^{\text{new}} = u_i - \frac{L_i(u_i) - f_i}{\partial L_i(u_i)/\partial u_i}. \quad (3.16)$$

3.4 Initial conditions

So far we have described how the particles evolve under their mutual gravity. However, in a cosmological simulation, we must first place these particles into the simulation box – we must specify the initial conditions (IC). The particles cannot be placed arbitrarily but they must represent the real Universe. Among the properties we want is the particles to simulate our homogeneous, isotropic, and infinite Universe. As we described in chapter 1 the particles evolve and the resulting density field δ is not perfectly homogeneous. Statistical properties of the Gaussian density field, which is predicted by simple inflation models and supported by observation, can be entirely described by the matter power spectrum $P(k)$. Any procedure for generating the IC must be able to place the particles in the simulation box such as the resulting density field retains all of these properties.

Our code for generating the IC is based on a convolution method described by **1997ApJ...490L.127P**. We first create a random uncorrelated Gaussian density field $n(x)$ of unit variance. This white noise has a constant power spectrum $\langle |\hat{n}(k)|^2 \rangle = 1$. We then convolve this field with a correlation kernel $W(k) = \sqrt{P(k)}$ to obtain the initial density field

$$\delta(k) = n(k)W(k). \quad (3.17)$$

It can be easily seen that this density field has the correct power spectrum $\langle |\hat{\delta}(k)|^2 \rangle = P(k)$. This density field is then used to compute the gravitation potential and forces in the simulation box. The actual positions and velocities of the particles are found using the linear perturbation theory, the Zel'dovich approximation (**1970A&A.....5...84Z**),

$$\mathbf{x} = \mathbf{q} + D(t)\mathbf{S}(\mathbf{q}), \quad (3.18)$$

where D is the growth function at the start of the simulation (typically $z \sim 20 - 200$). The displacement field S is computed from the linear theory and satisfies

$$\nabla \cdot \mathbf{S} = -\delta. \quad (3.19)$$

The initial positions \mathbf{q} of particles are chosen to be grid points of the simulation box to satisfy homogeneity and isotropy. We use these grid-based IC but the so-called glass IC can also be employed. In the glass IC, the particles are placed at random positions across the box and then evolved with repulsive gravity until they reach an equilibrium state. These IC look more natural but contain lots of white noise power.

In order to have reliable results, one has to run the cosmological simulation many times with different IC to lower the sampling variance. To accelerate the convergence, we use each IC twice, the second time with opposite phases (**PhysRevD.93.103519**). Opposite phases of the density field in the Fourier space correspond to switched minima and maxima of the gravitation potential in the real space, $n_2(\mathbf{x}) = -n_1(\mathbf{x})$

3.5 Core Cosmology Library

The Core Cosmology Library (**CCL**, **2019ApJS..242....2C**) is an open-source software package written in C, with a python interface. The **CCL** provides routines to compute basic cosmological observables such as various distances, power spectra, correlation functions, and many others. The accuracy of all quantities has been extensively tested and compared with many other independent software packages. This allows establishing a well-defined numerical accuracy for each predicted quantity. The **CCL** was developed for the needs of the DESC of the LSST which needs very precise predictions for the next generation of cosmological analysis. The author contributed to the development of this library, mainly by writing documentation, examples of usage and helping with automatization process and improving its compatibility.

We use **CCL** for quantities such as linear and non-linear power spectra or growth functions. Internally, **CCL** calculates the matter power spectrum $P(k)$ using various methods including common approximations, by calling external software such as Cosmic Linear Anisotropy Solving System (**CLASS**, **class**), or emulators, such as the CosmicEmu emulator (**Heitmann:2015xma**).

3.6 Other methods

3.6.1 TreePM

The tree code was pioneered by **1986Natur.324..446B** and uses a hierarchical spatial tree to define localized groups of particles. This has an advantage over an equidistant mesh when dealing with highly inhomogeneous systems like stellar dynamics when few cells ~~would can~~ contain most of the particles ~~With the usual in the system. When using the~~ oct-tree, each cubic cell containing more than some maximum number of particles is split into eight child cells of half their parent's size. ~~This results in In this way,~~ a tree-like hierarchy of cubic nodes ~~with the root box, containing all particles, at its bottom is created~~. The particles within each of the tree nodes constitute a well-defined and localized group. The potential of a cell is obtained by multipole expansion around some center of the group of particles (usually center of mass). The gravity at any point is then approximated by the summation of potentials from all other cells while considering only cells with a sufficiently small opening angle (size of the cell over the distance). If the opening angle is big the same algorithm is applied to the daughter cells (**2011EPJP..126...55D**).

3.6.2 Fast multipole methods

The fast multipole method of **1987JCoPh..73..325G** also works with localized particle groups and was originally proposed using a fixed grid but **2000ApJ...536L..39D** implemented the method using a tree structure with better results. The method works similarly as the tree code but in addition to expanding the potential at the source positions, it also expands it at the sink positions. This ~~dual expansion at both ends of all interactions considerably~~ speeds up the ~~simultaneous~~-computation of gravity for all particles ~~but brings significantly but has~~ no advantage over the tree ~~eode~~-methods when computing the force at a single position (**2011EPJP..126...55D**).

The second part of the force calculation is the interaction phase when the coefficients of the Taylor series are evaluated for each cell. If the opening angle for a mutual cell-cell interaction is small enough the coefficients for the interactions in each direction are computed. Otherwise, the interaction is split into up to 8 new interactions by opening the bigger of the two cells. The total ~~computational costs of this algorithm are dominated by complexity of the interaction phase, which only requires algorithm is given by~~ $\mathcal{O}(N_p)$ interactions for the computation of all N_p particle forces. This represents a ~~substantial great~~ reduction from the $\mathcal{O}(N_p^2)$ for direct summation and can greatly improves simulations of astrophysical problems with inhomogeneous particle distributions.

4. Approximation Schemes

In this chapter we will introduce different approximation methods that we plan to use in our numerical simulations. We will go over equations governing their behavior and we also briefly mention some other approximations that were used in the past.

Parts of this chapter have been published in **2020MNRAS.493.2085V**.

4.1 Motivation

Various approximations in different scientific fields have always been studied in detail. Many non-linear equations cannot be solved analytically and one can hope to achieve at least some results using linearization or other perturbation theories of higher-order. Cosmological simulations are no exception. From the beginning of first attempts to simulate clustering of matter on large scales in the late '60s the approximate methods were developed to help understand the dynamics of the Universe. The greatest pioneering efforts to improve and validate these approximate methods have been undertaken in the '90s.

These analytic or semi-analytic methods can be used to understand the otherwise very complicated problem of structure formation. Instead of running a simulation “blindly” and trying to analyze them phenomenologically one can compare these simulations with much better understood approximate methods.

Besides the usefulness of approximations in getting an insight into gravitational evolution, they are very helpful in getting a large number of simulations quickly. In order to study BAO, one needs a high number of simulations with very large volume and a high number of particles which requires demanding resources. The BAO scale is of particular interest to us as it lies between the linear regime which can be studied analytically and the highly non-linear regime of halo formation which requires precise N -body simulations. The semi-analytical methods are expected to work very well in this regime.

In this chapter, we describe several approximations that have been studied in the past – Zel’dovich approximation and its *truncated* extension, frozen-flow approximation, and frozen-potential approximation. The Zel’dovich approximation has been studied extensively in the past and here we use it mainly as a reference for comparison in the context of the other approximations.

4.2 Recapitulation of the linear theory

Here we remind some results of the linear theory previously presented in chapter 1. We rewrite the equations using variables more suited for cosmological simulations. We will be working in comoving coordinates – the comoving position \mathbf{x} is defined in terms of the proper position coordinate $\mathbf{r} = a\mathbf{x}$. The comoving velocity \mathbf{v} is then defined as a derivative with respect to cosmic time t , $\mathbf{v} = \dot{\mathbf{x}}$, where the overdot denotes a time derivative. Particles move in the Newtonian

gravitational potential, Φ . The equations for linear perturbations then read

$$\dot{\delta} + \nabla \cdot \mathbf{v} = 0, \quad (4.1)$$

$$\dot{\mathbf{v}} + 2\frac{\dot{a}}{a}\mathbf{v} = -\frac{1}{a^2}\nabla\Phi, \quad (4.2)$$

$$\begin{aligned} \Delta\Phi &= 4\pi G\bar{\rho}a^2\delta \\ &= \frac{3}{2}H_0^2\Omega_{m,0}\frac{\delta}{a} \equiv \mu^{-1}\frac{\delta}{a}, \end{aligned} \quad (4.3)$$

where we defined the constant $\mu \equiv \left(\frac{3}{2}H_0^2\Omega_{m,0}\right)^{-1}$. In this linear regime, the time and space dependence of the overdensity evolution are separable and we can write $\delta(a, \mathbf{x}) = D(a)\delta_0(\mathbf{x})$ where the growth factor D represents the growing solution (we neglect the decaying mode) and is normalized to unity at the present time.

It is often useful to rewrite these equations with a different time variable, namely the scale factor a . This is convenient both from the numerical and theoretical points of view because the quantities are “more constant”. With the new time-variable a and comoving velocity $\mathbf{u} = d\mathbf{x}/da$, equation (4.1) becomes

$$\frac{dD}{da}\delta_0 + \nabla \cdot \mathbf{u} = 0, \quad (4.4)$$

where $dD/da = 1$ in the Einstein–de Sitter universe (hereafter EdS) and so the divergence of the velocity field remains constant in both time and space. Equation (4.2) then becomes

$$\frac{d\mathbf{u}}{da} = -\frac{3}{2a}[\mathbf{u} + \mu\nabla\Phi] \quad (4.5a)$$

in EdS and, more generally,

$$\frac{d\mathbf{u}}{da} = -\frac{3}{2a}[\mathbf{u}(1 + \Omega_\Lambda) + \mu\nabla\Phi(1 - \Omega_\Lambda)] \quad (4.5b)$$

in the Λ CDM universe. The omega factor of the cosmological constant

$$\Omega_\Lambda(a) = \frac{\Omega_{\Lambda,0}a^3}{\Omega_{m,0} + \Omega_{\Lambda,0}a^3} \quad (4.6)$$

rises from 0 to $\Omega_{\Lambda,0}$ and becomes significant ($> 5\%$) around redshift $z \approx 2.5$. The transformation (2.22) from the Jordan frame to the Einstein frame introduces non-standard coupling of the chameleon field to standard matter resulting in the fifth force (2.32). Using our new variables, this equation reads

$$\frac{d\mathbf{u}_\chi}{da} = -\frac{3\mu}{2a}\frac{\beta}{M_{\text{pl}}}\nabla\chi. \quad (4.7)$$

Equation (4.3) expressed with the growth factor reads

$$\Delta\Phi(\mathbf{x}, a) = \mu^{-1}\frac{D}{a}\delta_0(\mathbf{x}). \quad (4.8)$$

4.3 Zel'dovich approximation

The Zel'dovich approximation (**1970A&A.....5...84Z**) bears its name after a pioneer in the study of large-scale structure, a Soviet physicist Yakov Zel'dovich. The ZA provides an intuitive way to understand the emergence of filamentary structures (cosmic web) and can realize the model of non-linear structure formation even though it is based only on linear approximations (**2014MNRAS.439.3630W**). The Zel'dovich approximation predicts the rich structure of voids, clusters, sheets, and filaments observed in the Universe.

The ZA is based on an ansatz that particles move in straight lines in the Lagrangian frame

$$\mathbf{x}(\mathbf{q}, a) = \mathbf{q} + D(a)\mathbf{S}(\mathbf{q}), \quad (4.9)$$

where \mathbf{q} are the initial positions (Eulerian coordinates) of a particle and \mathbf{S} is some displacement field. Inserting equation (4.9) into the continuity equation (4.4) yields

$$-\nabla \cdot \mathbf{S} = \delta_0. \quad (4.10)$$

Combining with the Poisson equation (4.8), we can see that (4.9) represents a potential flow, $\mathbf{S} = -\nabla\phi_V$, where the velocity potential ϕ_V obeys the Poisson equation

$$\Delta\phi_V = \delta_0 \quad (4.11)$$

and has a simple relation to the gravitational potential

$$\phi_V = \mu \frac{a}{D} \Phi. \quad (4.12)$$

This results to ZA being

$$\mathbf{x}(\mathbf{q}, a) = \mathbf{q} - D(a)\nabla\phi_V(\mathbf{q}). \quad (4.13)$$

Note that the velocity potential is not exactly a potential of our velocity field \mathbf{u} but

$$\mathbf{u}_{ZA}(\mathbf{x}) = -\frac{dD}{da}\nabla\phi_V(\mathbf{q}). \quad (4.14)$$

The ZA differs from other approximations (among other things) in how this (constant) velocity potential, ϕ_V , enters the equations of motion. To avoid having different definitions of the *real* velocity potential for the velocity fields in each approximation, we take the equation (4.11) as defining the velocity potential ϕ_V .

The deformation tensor is defined as

$$d_{ij} = \frac{\partial x_i}{\partial q_j} = \delta_{ij} + D \frac{\partial \nabla_i \phi_V}{\partial q_j}. \quad (4.15)$$

The eigenvectors of the deformation tensor determine the principal directions of the collapse and the corresponding eigenvalues determine the time when

the compression will be infinite. The density is given through eigenvalues λ_i as

$$\rho = \frac{\bar{\rho}}{(1 - D\lambda_1)(1 - D\lambda_2)(1 - D\lambda_3)} . \quad (4.16)$$

The time when the density in ZA becomes infinite corresponds to particles crossing the paths of other particles. Once this shell-crossing has occurred, the approximation has formally broken down, since there are no forces present to slow down the particles and capture them within halos.

In Figure 4.1 we show a comparison of the simulations with ZA at four different redshifts through the projected density field. At redshift $z = 1.82$ the cosmic web still looks nice but after that, at redshifts $z = 0.53, 0.00$, we can see that shell-crossing occurred and the overall picture gets blurry. The large-scale structures remain visible but the small-scale structures get diluted at later times.

4.4 Truncated Zel'dovich approximation

The shell-crossing and diffusion of particles on small scales in ZA happens the sooner the more power there is on small scales. **1993MNRAS.260..765C** suggested an improvement of the ZA by removing power on these small non-linear scales, i.e. to set the initial power spectrum to zero for wave-numbers k greater than a non-linear scale k_{nl} defined as

$$\frac{a^2(t)}{2\pi^2} \int_0^{k_{nl}} P(k) dk = 1 , \quad (4.17)$$

where the power spectrum $P(k)$ was defined in (1.82) as

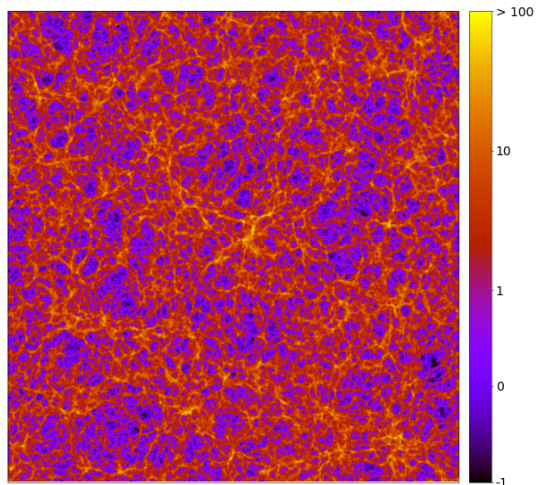
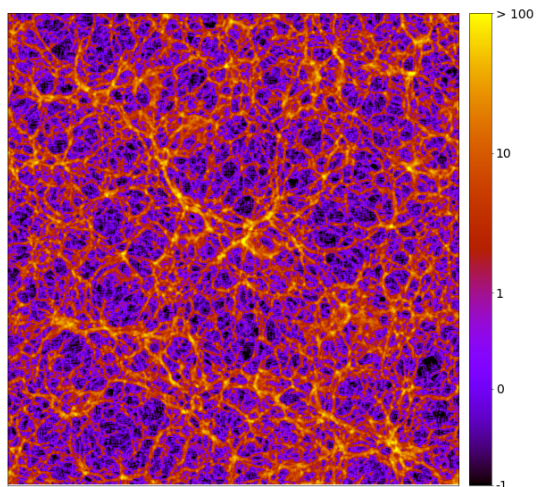
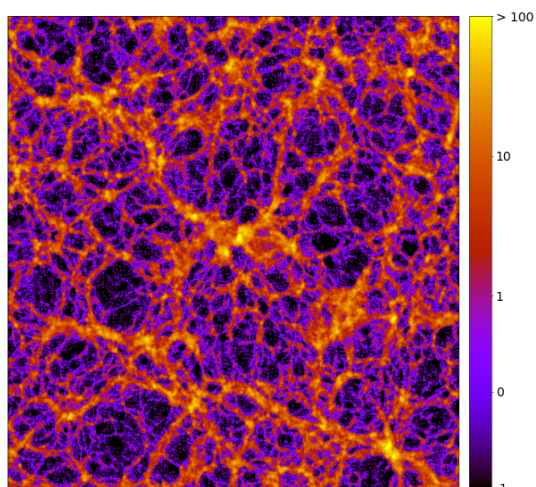
$$P(k)(2\pi)^3\delta_D(k - k') \equiv \langle \hat{\delta}(k)\hat{\delta}^*(k') \rangle . \quad (4.18)$$

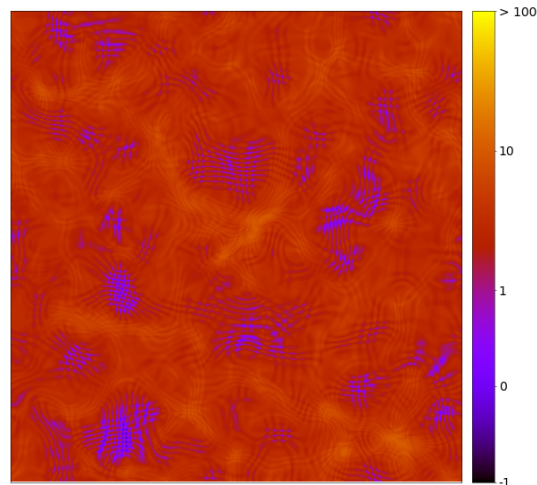
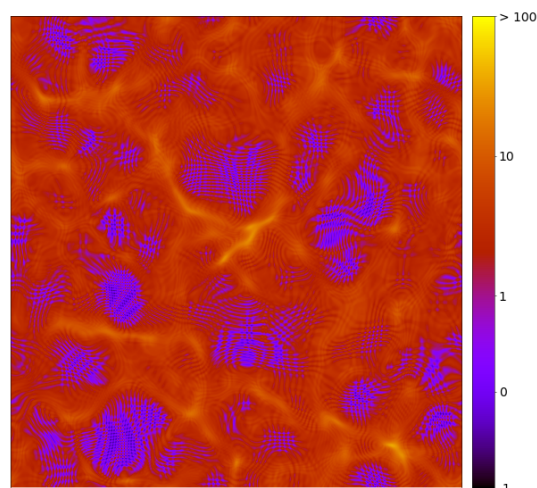
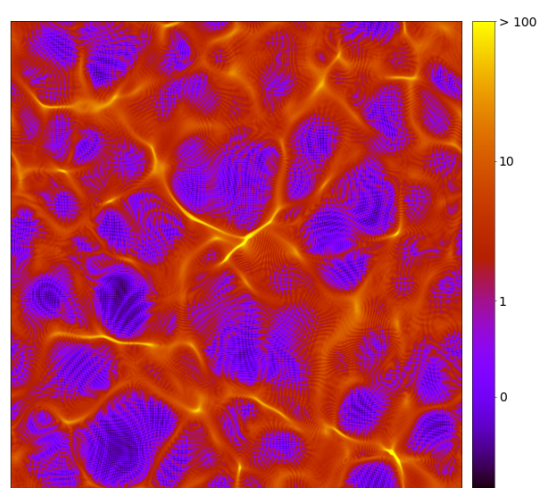
[doi:10.1093/mnras/269.3.626](https://doi.org/10.1093/mnras/269.3.626) further improved this truncation by applying a Gaussian window instead of an abrupt cutoff

$$W(k) = e^{-k^2/2k_G^2} , \quad (4.19)$$

where the smoothing scale k_G is 1 to 1.5 times k_{nl} . This filtering leads to the so-called truncated Zel'dovich approximation (TZA). This removes most of the strongly non-linear behavior and allows the Zel'dovich pancakes to be seen.

In Figure 4.2 we show a comparison of the simulations with TZA at four different redshifts through the projected density field. We see clear differences in comparison with ZA. Large-scale structures evolve similarly to ZA but we see clear artifacts on small scales given by artificial cutoff at these scales. These small-scale structures in filaments are not so diluted as in the case of ZA, however, a lot of particles remain in voids where they are frozen due to the lack of the initial kick.

(a) $z = 3.88$ (b) $z = 1.82$ (c) $z = 0.53$

(a) $z = 3.88$ (b) $z = 1.82$ (c) $z = 0.53$

4.5 Frozen flow approximation

The frozen-flow, or frozen-field, approximation (FFA) was originally proposed by **Matarrese:1992be** as the exact solution of equation (4.5a) in EdS

$$\tilde{\mathbf{u}}_{\text{FFA}}(\mathbf{x}) = \mathbf{u}_0(\mathbf{x}) = -\mu \nabla \Phi(\mathbf{x}) = -\nabla \phi_V(\mathbf{x}). \quad (4.20)$$

The velocity field $\tilde{\mathbf{u}}$ is frozen at each point to its initial value, i.e.

$$\frac{\partial \tilde{\mathbf{u}}}{\partial a} = 0. \quad (4.21)$$

These equations are very similar to ZA but now the particles update their velocities to the local value of the velocity field (not the initial value), without any memory of their previous motion. This can be viewed as a movement of particles under some force in a medium with very large viscosity. In our case of cosmological simulations, gravity represents the attractive force while Hubble friction represents the informal equivalent of a “damping” or “viscous” force.

Originally, **Matarrese:1992be** stated three main reasons of why should the FFA work:

- FFA is, by construction, consistent with linear theory and follows correctly the evolution at early times. Keeping the linear approximation for the velocity potential is justified by the fact that this quantity is more sensitive to large wavelength modes than the density, and is, therefore, less affected by strongly non-linear evolution.
- Stream-lines are frozen to their initial shape, so multistream regions cannot form and FFA avoids the formation of caustics at a finite time and can, therefore, work well after shell-crossing would occur in ZA. A particle moving according to FFA has zero velocity at minima (or maxima) of the gravitational potential. It will slow down its motion when approaching such a position – particles in FFA would need infinite time to reach such places. Particles move along curved paths and once they come close to pancake configurations they curve their trajectories, moving almost parallel to them, trying to reach the positions of filaments.
- This type of dynamics implies an artificial thickening of particles around pancakes, filaments, and knots, which mimics the real gravitational clustering around these types of structures.

The definition (4.20) is, however, no longer valid in the general Λ CDM cosmology where even in the linear regime both gravitational potential and velocity field undergo evolution. We generalize FFA for the Λ CDM cosmology by adding an extra time dependence in equation (4.20)

$$\mathbf{u}_{\text{FFA}}(\mathbf{x}, a) = -\frac{dD}{da}(a) \nabla \phi_V(\mathbf{x}). \quad (4.22)$$

This velocity field solves (4.5b) exactly, due to the definition of the growth factor and its relation to the velocity field in the linear regime (see equation (4.4)).

Although equation (4.22) now does not represent a *frozen* flow, particles still move along the same characteristic curves as in EdS, just with different velocities. The particle trajectories are described by the integral equation

$$\mathbf{x}(a) = \mathbf{q} + \int_0^a d\tilde{a} \mathbf{u}_{\text{FFA}}(\mathbf{x}(\tilde{a}), \tilde{a}). \quad (4.23)$$

In Figure 4.3 we show a comparison of the simulations with FFA at four different redshifts through the projected density field. Unlike in the case of ZA or TZA there is no shell-crossing and structures remain clear even at later times. As the particles approach minima of the gravitational potential, they slow down and we can see that resulting structures are elongated along stream-lines.

4.6 Frozen potential approximation

The frozen-potential approximation (FPA) was introduced by **1994MNRAS.266..227B**. They exploit the fact that the gravitational potential changes much more slowly than the density contrast, and hence may be viewed as essentially frozen. Moreover, like the velocity potential in FFA is more sensitive to large wavelength modes, this is doubly true for gravitational potential. They solved equation (4.5a) at each time-step with the initial (constant) gravitational potential. In Λ CDM

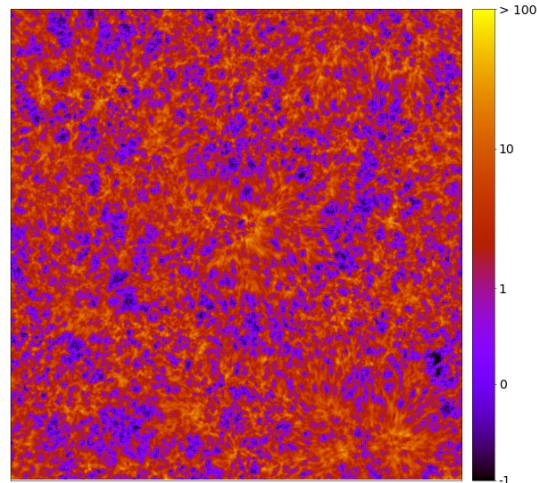
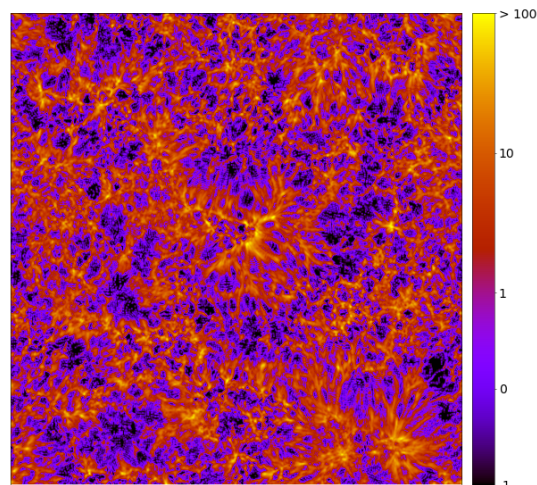
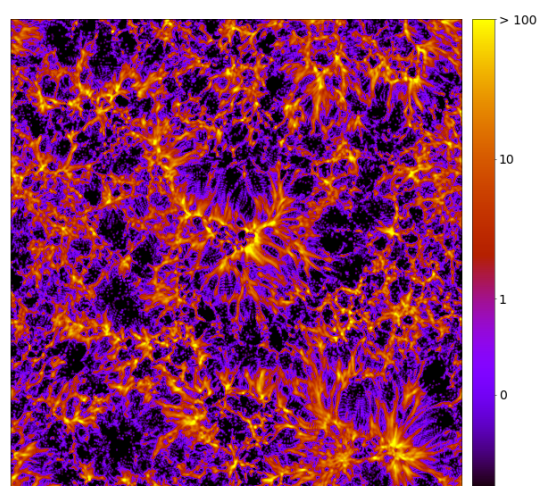
$$\frac{d\mathbf{u}_{\text{FPA}}}{da} = -\frac{3}{2a} \left[\mathbf{u}_{\text{FPA}}(\mathbf{x}, a) (1 + \Omega_\Lambda(a)) + \frac{D}{a} \nabla \phi_V(\mathbf{x}) (1 - \Omega_\Lambda(a)) \right] \quad (4.24)$$

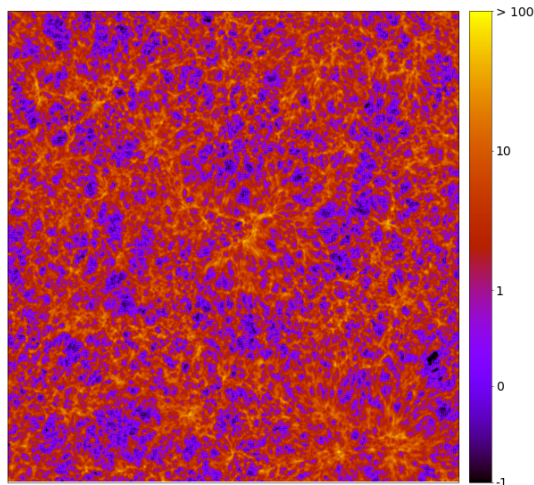
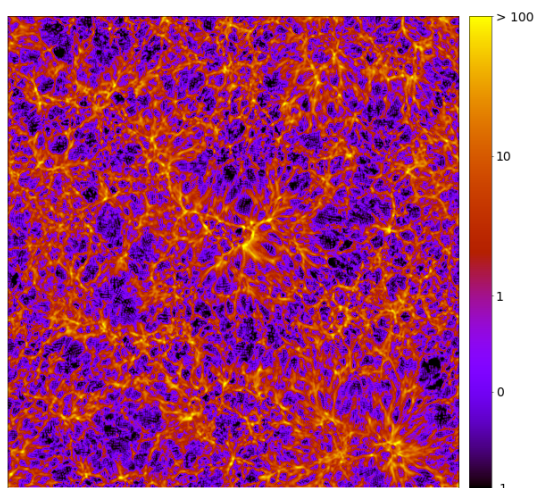
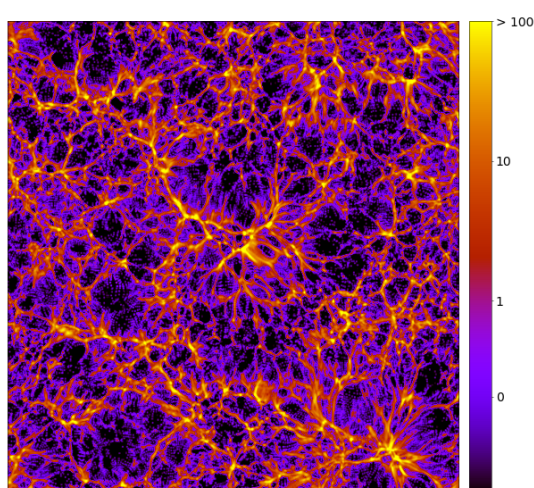
and the particle trajectories are given as in the case of FFA

$$\mathbf{x}(a) = \mathbf{q} + \int_0^a d\tilde{a} \mathbf{u}_{\text{FPA}}(\mathbf{x}(\tilde{a}), \tilde{a}). \quad (4.25)$$

Particles now follow the linear *gravitational* potential (which evolves slightly in Λ CDM) instead of the initial *velocity* potential as in the case of FFA. Equation (4.24) drives the particle velocities (approximately) to the velocities of FFA but unlike in the FFA, particles now keep their inertia. Same as in the case of FFA, the particles tend to move along the pancakes towards regions of lower potential ~~to end up in a few clumps~~. The acceleration used in FPA is largest in regions where the instantaneous velocity vector points along the gradient of the potential, as happen for particles after they cross the pancake. In FFA the inertia of particles is ignored, whereas in the Zel'dovich approximation inertia is assumed to dominate over the change in the force field. FPA takes into consideration both factors but assumes a constant potential.

In Figure 4.4 we show a comparison of the simulations with FPA at four different redshifts through the projected density field. At the first sight, it looks similarly as in the case of FFA, especially at early times. For $z = 0.53, 0.00$ we can see the differences due to the fact that particles have an inertia and resulting structures are not so elongated as in the case of FFA.

(a) $z = 3.88$ (b) $z = 1.82$ (c) $z = 0.53$

(a) $z = 3.88$ (b) $z = 1.82$ (c) $z = 0.53$

4.7 Particle-mesh simulation

For comparison with other approximations, we also implemented the particle-mesh code, i.e. a simulation where the gravitation potential evolves according to the current position of particles but the particles feel only this long-range force without any short-range forces (for details see section 3.2). The particles move according to the equation of motion (4.5b) and the gravitational potential evolve according to Poisson equation (4.3).

In Figure 4.5 we show a comparison of all approximation methods with PM at $z = 0$ through the projected density field. Here we can see side-by-side the main differences between individual approximation methods: ZA with diluted small-scale structures, TZA with (almost) frozen small-scale structures, FFA and FPA with elongated structures. We see that PM simulation has more concentrated filaments but also more particles in voids than ZA, FFA, and FPA.

4.8 Approximation methods in modified gravity

Here we remind the basic chameleon equations we want to solve numerically. The non-linear Poisson equation

$$\Delta(\chi/\chi_a) = C_\chi(a) \left[1 + \delta - \left(\frac{\chi_a}{\chi} \right)^{1-n} \right], \quad (4.26)$$

where

$$C_\chi(a) \equiv \frac{3H_0^2\Omega_m}{2\Phi_{0,\text{scr}}} a^{-3\frac{2-n}{1-n}} = (a\mu\Phi_{a,\text{scr}})^{-1}, \quad (4.27)$$

the linear solution

$$\chi(\mathbf{x}, a) = \chi_a(a) \left(1 + \frac{\Phi_G(\mathbf{x}, a)}{\Phi_{a,\text{scr}}(a)} \right). \quad (4.28)$$

the linear solution in k -space

$$\hat{\chi}(k) = -\frac{\chi_a}{1-n} \frac{m^2}{m^2 + k^2} \hat{\delta}(k) = -\frac{\beta\bar{\rho}_m}{M_{\text{pl}}} \frac{\hat{\delta}(k)}{k^2 + m^2}. \quad (4.29)$$

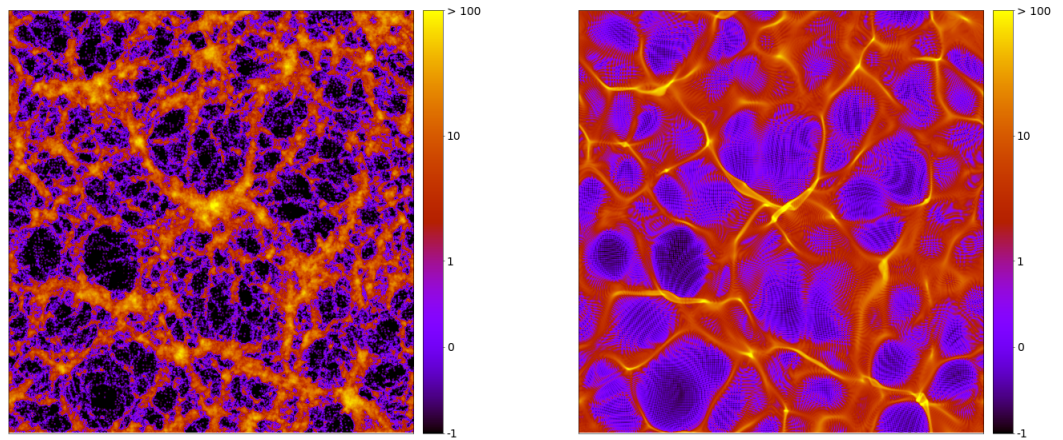
where the mass of the chameleon field is

$$m^2(a) \equiv \frac{1-n}{a\mu\Phi_{a,\text{scr}}}, \quad (4.30)$$

and the screened solution inside massive objects

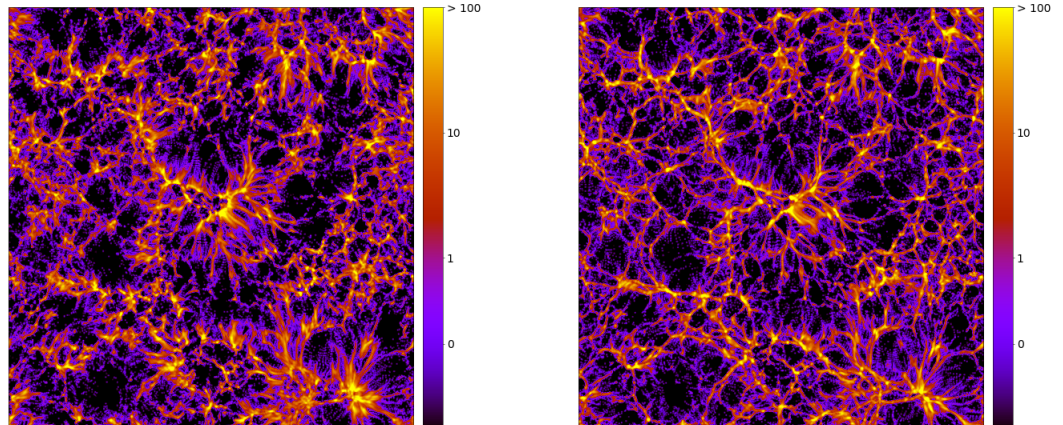
$$\chi = \frac{\chi_a}{(1+\delta)^{1/(1-n)}}. \quad (4.31)$$

When applying the approximation methods to the chameleon equations, we have three choices on how to arrive at an approximate solution:



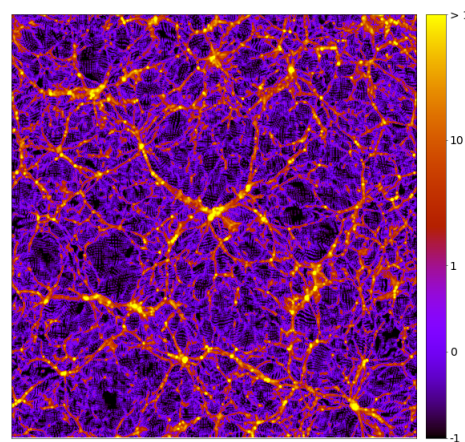
(a) Zel'dovich approximation

(b) Truncated Zel'dovich approximation



(c) Frozen-flow approximation

(d) Frozen-potential approximation



(e) PM simulation

Figure 4.5: Projected density field at redshift $z = 0$ for the different approximations, all run with the same initial conditions. Each slice has a box-length of $200 h^{-1}\text{Mpc}$ and is $1 h^{-1}\text{Mpc}$ thick.

1. Purely linear prediction in (\mathbf{q}, a) -space, solution (4.28)
2. Purely linear prediction in (\mathbf{k}, a) -space, solution (4.29)
3. Non-linear prediction in (\mathbf{x}, a) -space, solution (4.26)

Choice 1 means that there is no computational overhead and we can simply take the chameleon force to be $2\beta^2 a^{-2}$ of the gravitational one. This method clearly overestimates the chameleon force at early times when the chameleon’s Compton wavelength is short. This is because the solution (4.28) does not take into account the non-zero mass of the field.

A better choice is to use 2 where the non-zero mass is incorporated. This solution adds relatively little computational overhead over normal gravity – needing (at least) one Fourier transform and also extra storage. The overdensity $\delta(\mathbf{k}, a)$ is either the linearly evolved one, i.e. $\delta(\mathbf{k}, a) = D(a)\delta_0(\mathbf{k})$, or we can compute δ at each time-step from the current positions of particles. This adds extra computation when assigning the mass of particles on the grid and one extra Fourier transform to get $\delta(\mathbf{k}, a)$. However, we cannot use (4.29) blindly to get a solution in real space as this linear approximation breaks down inside massive objects where we would get a negative solution. This effect is similar to usage of linear evolution for δ where we can end up with regions where $\delta < -1$. We need to check if the resulting chameleon field is positive and fix it where it is not. We use the screening regime value (4.31) to get a positive solution. We will refer to this prediction as pseudo-linear since it can address some effects of the screening mechanism.

The most expensive choice is 3 where we must iteratively solve nonlinear equations. Unlike other methods, this one can address the screening regime inside and near massive objects but at the cost of the most computational overhead.

4.9 Other approximations

Approximations described previously are studied numerically in detail in the next chapter. Here we present a few of the other approximations studied in the past or used today.

4.9.1 Adhesion approximation

The adhesion approximation was introduced in **1989MNRAS.236..385G**. To study the evolution of density inhomogeneities they used the model of non-linear diffusion (Burger’s equation), that gives an approximate description of the growth of structures at the advanced non-linear stage of gravitational instability.

To overcome problems of ZA with shell-crossing they propose a solution of “sticking articles.” Particles move according to ZA until they ran into one another. Then they move together, with the velocity conserving momentum. This model can be described mathematically by inserting the viscous term into

equations of motion, simulating attractive forces of gravity

$$\frac{d\mathbf{u}_{AA}}{da} = \nu \frac{\partial^2 \mathbf{u}}{\partial \mathbf{x}^2}. \quad (4.32)$$

The Burger's equation has an analytical solution that can be used to study the formation of structures. For more information regarding the adhesion approximation see also **1990MNRAS.247..260W; 1994ApJ...428...28M**.

4.9.2 Stable clustering

It was proposed by **1974ApJ...189L..51P** that ~~clustering in the very we can study the behavior of a~~ non-linear regime might be understood by assuming that regions of clustering in high-density contrast undergo regions by assuming that these regions have undergone virialization and subsequently now maintain a fixed proper density, hence stable clustering. The correlation function ~~for a population~~ of such systems would ~~then simply~~ evolve according to

$$\xi(r, a) \propto 1/\bar{\rho} \propto a^3. \quad (4.33)$$

1991ApJ...374L...1H developed a ~~method for interpolating between model which enabled interpolating between the~~ linear theory on large scales and the non-linear predictions of the stable clustering ~~hypothesis~~ on small scales. They showed that the non-linear ~~volume-averaged~~ two-point correlation function could be parameterized by a simple function of the linear correlation function

$$\bar{\xi}_{NL} = f(\bar{\xi}_L), \quad (4.34)$$

where the functional form of f can be derived from the spherical top-hat model without any shell-crossing. For the linear regime $\bar{\xi}_L \ll 1$, $f(y) = y$, and for non-linear $\bar{\xi}_L \gg 1$, $f(y) = y^{3/2}$. For more information regarding the stable clustering see also **1996MNRAS.280L..19P; 2003MNRAS.341.131S**.

4.9.3 Lagrangian perturbation theories of higher-orders

The success of ZA, the first-order Lagrangian perturbation theory (LPT), has motivated studies of higher-order corrections (**10.1093/mnras/264.2.375; 2002PhR...367....1B; 2010MNRAS.403.1859J; 2014ApJ...788...63S**). In the Lagrangian description, the spatial coordinates are transformed through the displacement vector Ψ as

$$\mathbf{x} = \mathbf{q} + \Psi(a, \mathbf{x}). \quad (4.35)$$

In LPT, this displacement vector field is expanded in a perturbation series in the linear growth function D in Fourier space. Density perturbations δ are described as a function of the displacement vector through conservation of mass. ~~This Lagrangian picture is intrinsically non-linear in the density field, and a small perturbation in Lagrangian fluid element paths carries a considerable amount of non-linear information about the corresponding Eulerian density and velocity fields.~~

5. Simulations with Approximation Methods

In this chapter we present main results of our research regarding approximation techniques and the possibility to use these techniques in studies of modified gravity. Parts of this chapter have been published in **2020MNRAS.493.2085V**.

We ran our simulations with the Planck Λ CDM cosmology (**planck·cosm**); its parameters are summarized in Table 5.1. We expect our results to apply generically to cosmologies that are not too far from this set of parameter values. The non-linear scale (4.17) for our chosen power spectrum is $k_{nl} = 0.32 \text{ } h\text{Mpc}^{-1}$. The smoothing scale for TZA is suggested to be in the range from 1 to 1.5 times k_{nl} so we ran the TZA simulations twice, once with $k_G = 0.3 \text{ } h\text{Mpc}^{-1}$ and once with $k_G = 0.5 \text{ } h\text{Mpc}^{-1}$. The results using $k_G = 0.5 \text{ } h\text{Mpc}^{-1}$ proved to be better in terms of predicting the BAO features so we show only those results.

In the plots we use various abbreviations for compactness, while discussing the results of the simulations and the linear and non-linear predictions. These are summarized in Table 5.2.

In total, we ran and analyzed 7117 simulations using different approximations, parameters of the simulation volume and chameleon parameters. Their properties are described in Table 5.3 – Table 5.6.

Hubble constant [km s ⁻¹ Mpc ⁻¹]	H_0	67.74
Baryon density parameter	Ω_b	0.0486
Matter density parameter	Ω_m	0.3089
Total density parameter	Ω_{tot}	1
Scalar spectral index	n_s	0.9667
Fluctuation amplitude at $8h^{-1}\text{Mpc}$	σ_8	0.8159

Table 5.1: Planck Collaboration cosmological parameters (**planck·cosm**) used in the simulations.

Λ CDM (lin)	prediction of the linear theory with standard gravity
Λ CDM (nl)	prediction of the emulator with standard gravity
ZA, TZA, FFA, FPA	simulation run with given approximation and standard gravity
χ (psl)	simulation run with pseudo-linear prediction of modified gravity
χ (nl)	simulation run with non-linear solution of modified gravity

Table 5.2: Abbreviations used in the plots.

L	N_p	N_f	N_a	N	N_t	m
100	512^3	512^3	1024^3	1	200	$9.4 \cdot 10^8$
100	512^3	512^3	1024^3	211	100	$9.4 \cdot 10^8$
200	512^3	512^3	1024^3	1	200	$7.6 \cdot 10^9$
200	512^3	512^3	1024^3	2	100	$7.6 \cdot 10^9$
300	512^3	512^3	1024^3	1	200	$2.6 \cdot 10^{10}$
400	512^3	512^3	1024^3	1	200	$6.0 \cdot 10^{10}$
500	512^3	512^3	1024^3	1	200	$1.2 \cdot 10^{11}$
500	512^3	512^3	1024^3	1	200	$1.2 \cdot 10^{11}$
500	512^3	512^3	1024^3	207	100	$1.2 \cdot 10^{11}$
2000	512^3	512^3	1024^3	20	400	$7.6 \cdot 10^{12}$
2000	512^3	512^3	1024^3	201	100	$7.6 \cdot 10^{12}$
2000	512^3	512^3	1024^3	20	200	$7.6 \cdot 10^{12}$
2000	512^3	512^3	1024^3	50	$7.6 \cdot 10^{12}$	
2000	512^3	512^3	1024^3	20	25	$7.6 \cdot 10^{12}$

L	N_p	N_f	N_a	N	N_t	m
100	512^3	512^3	1024^3	1	200	$9.4 \cdot 10^8$
100	512^3	512^3	1024^3	211	100	$9.4 \cdot 10^8$
200	512^3	512^3	1024^3	1	200	$7.6 \cdot 10^9$
200	512^3	512^3	1024^3	2	100	$7.6 \cdot 10^9$
300	512^3	512^3	1024^3	1	200	$2.6 \cdot 10^{10}$
400	512^3	512^3	1024^3	1	200	$6.0 \cdot 10^{10}$
500	512^3	512^3	1024^3	1	200	$1.2 \cdot 10^{11}$
500	512^3	512^3	1024^3	1	200	$1.2 \cdot 10^{11}$
500	512^3	512^3	1024^3	207	100	$1.2 \cdot 10^{11}$
2000	512^3	512^3	1024^3	20	400	$7.6 \cdot 10^{12}$
2000	512^3	512^3	1024^3	201	100	$7.6 \cdot 10^{12}$
2000	512^3	512^3	1024^3	20	200	$7.6 \cdot 10^{12}$
2000	512^3	512^3	1024^3	50	$7.6 \cdot 10^{12}$	
2000	512^3	512^3	1024^3	20	25	$7.6 \cdot 10^{12}$
2000	512^3	512^3	1024^3	20	25	$7.6 \cdot 10^{12}$

Table 5.3: Parameters of the simulations for ZA (left) and TZA (right): box size L [$h^{-1}\text{Mpc}$], number of particles N_p , number of force mesh points N_f , number of power spectrum mesh points N_a , number of runs N , number of time-steps N_t , and a derived parameter particle mass m [M_\odot].

L	N_p	N_f	N_a	N	N_t	m
2000	64^3	64^3	128^3	1	100	$3.9 \cdot 10^{15}$
2000	256^3	256^3	512^3	99	100	$6.0 \cdot 10^{13}$
100	512^3	512^3	1024^3	1	200	$9.4 \cdot 10^8$
100	512^3	512^3	1024^3	211	100	$9.4 \cdot 10^8$
200	512^3	512^3	1024^3	1	200	$7.6 \cdot 10^9$
200	512^3	512^3	1024^3	2	100	$7.6 \cdot 10^9$
300	512^3	512^3	1024^3	1	200	$2.6 \cdot 10^{10}$
400	512^3	512^3	1024^3	1	200	$6.0 \cdot 10^{10}$
500	512^3	512^3	1024^3	1	200	$1.2 \cdot 10^{11}$
500	512^3	512^3	1024^3	208	100	$1.2 \cdot 10^{11}$
2000	512^3	512^3	1024^3	20	400	$7.6 \cdot 10^{12}$
2000	512^3	512^3	1024^3	20	200	$7.6 \cdot 10^{12}$
2000	512^3	512^3	1024^3	201	100	$7.6 \cdot 10^{12}$
2000	512^3	512^3	1024^3	20	50	$7.6 \cdot 10^{12}$
2000	512^3	512^3	1024^3	19	25	$7.6 \cdot 10^{12}$

Table 5.4: Parameters of the simulations for FF (left) and FP (right): box size L [$h^{-1}\text{Mpc}$], number of particles N_p , number of force mesh points N_f , number of power spectrum mesh points N_a , number of runs N , number of runs N_a , number of time-steps N_t , and a derived parameter particle mass m [M_\odot].

L	N_p	N_f	N_a	N	N_t	m	Φ_{scr}	n
2000	256^3	256^3	512^3	100	100	$6.0 \cdot 10^{13}$	$1.0 \cdot 10^{-4}$	0.5
2000	256^3	256^3	512^3	96	100	$6.0 \cdot 10^{13}$	$1.0 \cdot 10^{-5}$	0.7
2000	256^3	256^3	512^3	98	100	$6.0 \cdot 10^{13}$	$1.0 \cdot 10^{-6}$	0.5
2000	256^3	256^3	512^3	97	100	$6.0 \cdot 10^{13}$	$1.0 \cdot 10^{-5}$	0.5
2000	256^3	256^3	512^3	99	100	$6.0 \cdot 10^{13}$	$1.0 \cdot 10^{-5}$	0.1

	L	N_p	N_f	N_a	N	N_t	m	Φ_{scr}	n
		1000	256^3	256^3	512^3	101	100	$7.6 \cdot 10^{12}$	$1.0 \cdot 10^{-5}$
		2000	256^3	256^3	512^3	100	100	$6.0 \cdot 10^{13}$	$1.0 \cdot 10^{-6}$
		2000	256^3	256^3	512^3	99	100	$6.0 \cdot 10^{13}$	$1.0 \cdot 10^{-5}$
		2000	256^3	256^3	512^3	120	100	$6.0 \cdot 10^{13}$	$1.0 \cdot 10^{-5}$
		2000	256^3	256^3	512^3	100	100	$6.0 \cdot 10^{13}$	$1.0 \cdot 10^{-5}$
		2000	256^3	256^3	512^3	100	100	$6.0 \cdot 10^{13}$	$1.0 \cdot 10^{-5}$
		500	512^3	512^3	1024^3	100	100	$9.4 \cdot 10^8$	$1.0 \cdot 10^{-5}$
		500	512^3	512^3	1024^3	100	100	$1.2 \cdot 10^{11}$	$1.0 \cdot 10^{-5}$

Table 5.5: Parameters of the pseudo-linear chameleon simulation for FF (left) and FP (right): box size L [$h^{-1}\text{Mpc}$], number of particles N_p , number of force mesh points N_f , number of power spectrum mesh points N_a , number of runs N , number of time-steps N_t , a derived parameter particle mass m [M_\odot], screening potential Φ_{scr} , and the chameleon power-law exponent n .

L	N_p	N_f	N_a	N	N_t	m	Φ_{scr}	n
2000	256^3	256^3	512^3	100	100	$6.0 \cdot 10^{13}$	$1.0 \cdot 10^{-5}$	0.5
2000	256^3	256^3	512^3	99	100	$6.0 \cdot 10^{13}$	$1.0 \cdot 10^{-5}$	0.1
2000	256^3	256^3	512^3	99	100	$6.0 \cdot 10^{13}$	$1.0 \cdot 10^{-4}$	0.5
2000	256^3	256^3	512^3	100	100	$6.0 \cdot 10^{13}$	$1.0 \cdot 10^{-5}$	0.7
2000	256^3	256^3	512^3	99	100	$6.0 \cdot 10^{13}$	$1.0 \cdot 10^{-6}$	0.5
500	512^3	512^3	512^3	98	100	$6.0 \cdot 10^{13}$	$1.0 \cdot 10^{-5}$	0.5
1000	256^3	256^3	512^3	77	100	$7.6 \cdot 10^{12}$	$1.0 \cdot 10^{-5}$	0.5
2000	256^3	256^3	512^3	96	100	$6.0 \cdot 10^{13}$	$1.0 \cdot 10^{-6}$	0.5
2000	256^3	256^3	512^3	100	100	$6.0 \cdot 10^{13}$	$1.0 \cdot 10^{-5}$	0.1
2000	256^3	256^3	512^3	102	100	$6.0 \cdot 10^{13}$	$1.0 \cdot 10^{-5}$	0.5
2000	256^3	256^3	512^3	99	100	$6.0 \cdot 10^{13}$	$1.0 \cdot 10^{-5}$	0.7
500	512^3	512^3	1024^3	100	100	$9.4 \cdot 10^8$	$1.0 \cdot 10^{-5}$	0.5
500	512^3	512^3	1024^3	98	100	$1.2 \cdot 10^{11}$	$1.0 \cdot 10^{-5}$	0.5

Table 5.6: Parameters of the non-linear chameleon simulation for FF and FP: box size L [$h^{-1}\text{Mpc}$], number of particles N_p , number of force mesh points N_f , number of power spectrum mesh points N_a , number of runs N , number of time-steps N_t , a derived parameter particle mass m [M_\odot], screening potential Φ_{scr} , and the chameleon power-law exponent n .

5.1 Results for standard gravity

5.1.1 Matter Power Spectrum

The power spectrum is defined by equation (1.82). In Figure 5.1 we show the power spectra $P(k)$ at redshifts $z = 0$ and $z = 1.8$ for the different approximation schemes. The gray areas represent variation across different realizations (different simulation runs). We see that on large (linear) scales all approximations reproduce the linear theory prediction (note that this is because the FFA and FFP results have been compensated for slower growth, as described below). On smaller scales, differences between the approximations become apparent. At the higher redshift, the TZA is still missing a lot of power due to the initial truncation while ZA sticks close to the linear prediction. At $z = 0$, the ZA loses power compared to the linear power spectrum on these scales due to shell-crossing. In contrast, FFA and FPA do much better and can even partially simulate non-linear clustering.

Comparison with linear theory

The relative differences between power spectra and the linear predictions at different redshifts are plotted in ???. By the linear prediction, in this case, is meant the initial power spectrum of the realization linearly evolved to the given epoch. The error bars once again represent variation across different realizations but individual differences are computed from the same realization of the power spectrum.

The upper panel shows the non-linear power spectrum $P(k)$ generated by the CosmicEmu emulator (**Heitmann:2015xma**) for comparison purposes. The emulator predictions involve interpolations across results from a finite number of high-resolution simulations run with different cosmological parameters; the results are accurate at the level of a few percent.

As expected, the ZA predicts power spectra at large scales very well but fails on small scales at later times. In the case of FFA and FPA, the power spectrum growth is slower than linear theory predicts but, unlike ZA, this behavior is across all scales and there is significantly less suppression of power on smaller scales.

5.1.2 Effective Redshift

The power spectrum growth is slower than the linear prediction in the case of FFA or FPA. For FFA, this can be understood from the equation of motion (4.22). As the particles approach the minimum of the gravitational well, their velocities decrease as the gradient of the potential drops. In these approximations, as the velocity potential is constant in time, there is no change in slope as more and more particles arrive into the gravitational well, which is certainly not realistic. (If possible, the resulting artifacts should be corrected when using these approximations.)

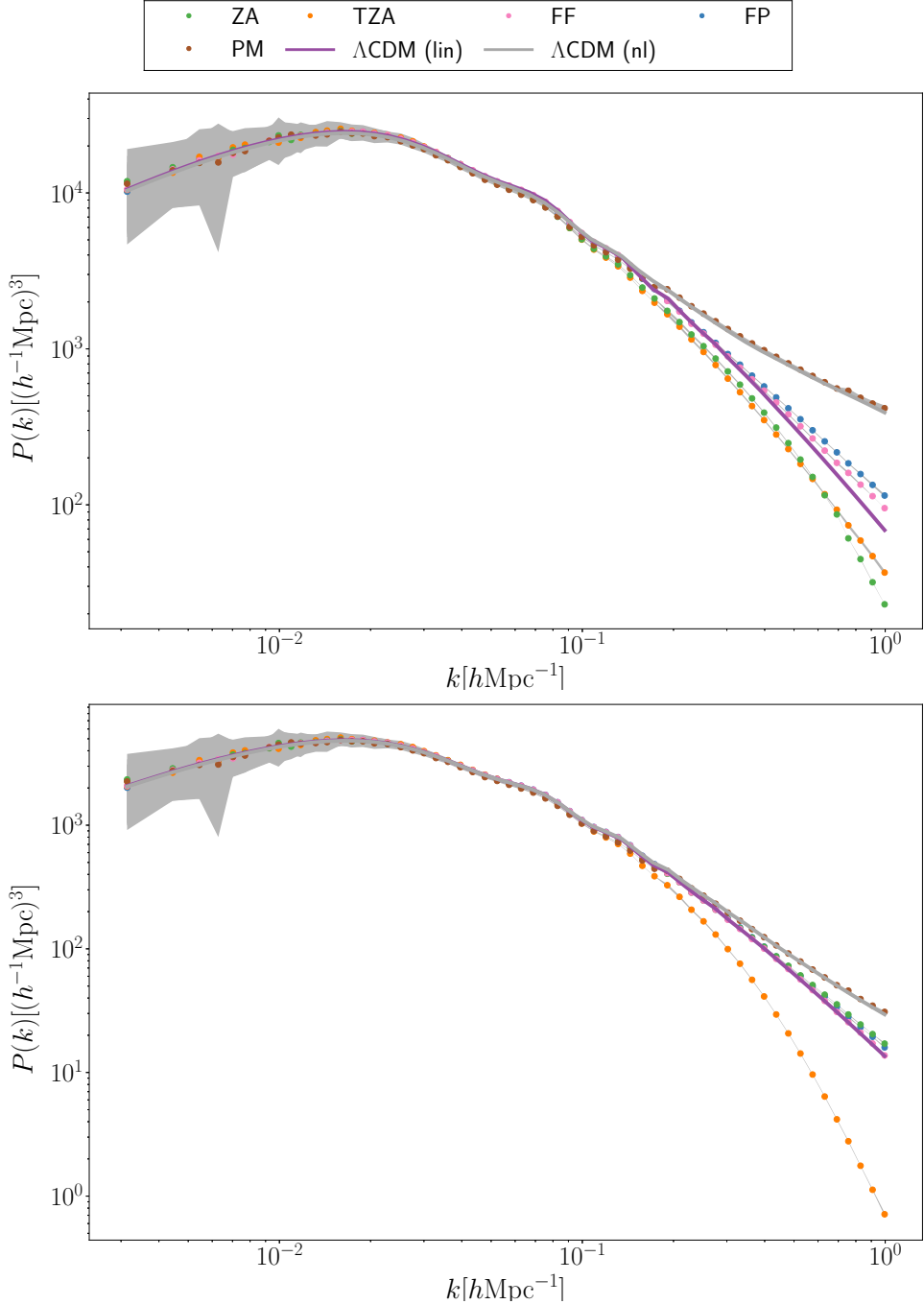


Figure 5.1: Matter power spectrum $P(k)$ at redshifts $z = 0$ (top) and $z = 1.8$ (bottom) for different approximation schemes. Grey areas represent variations across different runs. At $z = 1.8$, the TZA is much below the linear prediction due to the initial truncation whereas ZA stick close to the linear prediction. At $z = 0$, due to shell-crossing, ZA filters the power at higher k , falling below the linear power spectrum, whereas FFA and FPA retain some features of the full non-linear clustering.

For FPA, the reason for the suppression is very similar, although not as significant. Particles are not moving without any memory of their previous positions as in the case of FFA. They do not stop at the bottom of the well but rather oscillate around it. However, equation (4.24) still drives them toward the velocities of FFA and they slow down inside gravitational wells.

Note that this effect of slower growth due to a decreasing gradient of the velocity potential is not bound to some particular scale – it occurs both in shallow large wells as well as in deep and more concentrated wells. Consequently, it can be compensated via a correction factor. A similar situation occurs in particle-mesh codes when the number of time-steps is restricted because the assumption of constancy in velocity and force (the “drift” and “kick” terms in a standard integrator) fails to hold. In approximate particle-mesh codes, this error may be compensated by employing a ZA-motivated correction (**Ref:Feng**) in the time-stepping. The same technique could be applied here by combining the approximations in a suitable way or, as we do, by simply calibrating against linear theory, which yields the same result.

Additionally, the dynamical approximations in FFA and FPA can lead to artificial non-linear enhancement of the growth at later times on small scales within deep wells. It takes more time to get into a local gravitational well than in standard N -body but once the particles are there, they may form stable cores as they simply move towards the local potential minimum. On these small scales, the approximations are not valid in any case, so this point is mostly academic.

As discussed above, the suppression of linear growth in FFA and FPA can be viewed as a modified growth function and we can introduce a simple rescaling via an effective redshift z_{eff} so that the power spectrum on large linear scales matches the linear prediction

$$\langle P(k, z_{\text{eff}}) \rangle = \langle P_{\text{lin}}(k, z) \rangle, \quad (5.1)$$

where we are averaging over “large scales”. In our simulations, this means we are fitting the linear power spectrum in the range from the minimum available wave-number $k_{\text{min}} = 2\pi/L$ to half a decade $k = \sqrt{10}k_{\text{min}}$.

In the rest of the paper when we are comparing our results with a prediction of the linear or non-linear theory, we use this effective time instead of the simulation time unless stated otherwise.

In ??, we compare the effective growth function with the linear growth function of Λ CDM. For ZA and TZA there is almost no suppression as we are comparing large scales. However, at later times (or if we had used smaller scales) we would see an exponential suppression as described in **Bharadwaj 1996**. For FFA and FPA we have an almost linear dependence of D_{eff} on a , for FFA with a slope of approximately 8% and for FPA with the slope being approximately 6%.

In ?? we study the dependence of D_{eff} on the number of time-steps. A larger number of time-steps improves D_{eff} for FPA but, as expected, cannot eliminate the effect. In the case of FFA, D_{eff} actually decreases with an increase in the number of time-steps. In this case, for a smaller number of time-steps, particles do not evolve exactly along characteristic curves of the (initial) potential, and the deceleration is suppressed.

After the linear theory compensation via the effective time, all approximations match the linear prediction on large scales (by definition), however, on smaller scales, there are considerable differences. In the case of ZA (and TZA) at early times there is an enhancement of power above linear theory, but at later times, the lack of the ability to follow small-scale structure (“diffusion” at caustics)

causes a suppression of power that continues to leak to larger scales. For FFA and FPA, however, the behavior is quite different. At early times particles on the smallest scales are almost in the minimum of the local gravitational potential (and consequently at the minimum of the velocity potential) and do not evolve much. This effect is weaker for FPA where particles have inertia and are not overdamped. At later times more and more particles end up in these (constant-in-time) gravitational wells and we observe (partial) non-linear gravitational clustering.

5.1.3 Correlation Function

The two-point correlation function is defined by the equation (1.81). We computed the correlation function as an inverse Fourier transformation of (1.83) as

$$\xi(r) = \langle \delta(\mathbf{x})\delta(\mathbf{x} + \mathbf{r}) \rangle = \int \frac{d^3k}{(2\pi)^3} P(k) e^{i\mathbf{k}\cdot\mathbf{r}}. \quad (5.2)$$

We computed the correlation function $\xi(r)$ for different approximation schemes at different redshifts directly from the measured matter power spectrum $P(k)$ using equation (5.2). In ??, we display an example of the correlation function at redshift $z = 0.5$. All approximations agree reasonably with the full non-linear predictions of the emulator for the location of the BAO peak and its width.

Individual features of the BAO peak – location r_0 , amplitude A and width σ – are obtained by fitting a Gaussian to $r^2\xi(r)$ around the BAO peak

$$\xi_G(r) = A \cdot e^{-(r-r_0)^2/2\sigma^2} \quad (5.3)$$

In ??, we show these features of the BAO peak relative to the non-linear predictions of the emulator as a function of time. All approximations can predict the location of the peak with 1% accuracy. In predicting the shape of the peak, however, they do worse – all approximations deviate in predictions for the peak width and amplitude. Note that which approximation does best (compared to the others) for a given quantity is a function of redshift.

5.1.4 Halo mass function

We computed the halo mass function (1.86) from the amplitude of density fluctuations for all approximation schemes. For our simple analysis we just use the fitting formula (1.88) instead of implementing the full friend-of-friend algorithm.

The comparison of approximations in mass range $(10^{11} - 10^{15} M_\odot)$, is shown in ???. We see that TZA for higher redshifts is completely wrong as its missing a lot of power on these scales. At higher redshifts, this gets better as the TZA gets more power on these scales without so much shell-crossing as ZA. We see that for $z = 0$ TZA gives results closer to the linear prediction than ZA.

Also in ?? we show the halo mass function in more detail, mainly as a relative difference between prediction of approximation schemes and prediction of the non-linear theory. We see that approximation schemes generally predicts less massive halos ($M \gtrsim 10^{12} M_{\odot}$) and more light halos ($M \lesssim 10^{12} M_{\odot}$). We see that simple PM simulations get results close to the non-linear prediction, except at higher redshift.

5.2 Results for modified gravity

In this section, we apply the approximate techniques to chameleon gravity. Parameters of all run and analyzed simulations are described in Table 5.5 and Table 5.6. We focused on issues closely related to the scale where the chameleon field starts to affect the matter distribution. We first wish to study the effects of varying the simulation resolution on the power spectrum. Because the screening mechanism is directly related to the depth of the gravitational wells, and with lower spatial resolution, these wells are smeared, the role of the resolution also needs to be understood. For this analysis, we chose the FPA as this approximation is closest in spirit to N -body simulations.

Following this, we compare the results of chameleon gravity directly against the FPA and FFA simulations. We will study both k -space effects (power spectrum) and real-space effects (BAO peak in the correlation function). For chameleon gravity we ran all simulations twice – once solving the non-linear Poisson equation (4.26) using the multigrid solver, and the second using the pseudo-linear prediction for the chameleon in k -space given by (4.29) corrected by (4.31).

5.2.1 Effect of simulation resolution

In order to study the effects of the simulation resolution, we define this resolution via the Nyquist wave-number k_{nq}

$$k_{\text{nq}} = \frac{\pi N_f}{L}. \quad (5.4)$$

We wish to study two things in particular. The first is the minimum resolution needed to explore some particular scale, i.e., whether non-linear effects on smaller scales can affect larger scales. The second is to study the validity range of the pseudo-linear approximation of the chameleon field. We want to investigate on which scale this approximation breaks down and cannot be used even for generating approximate results.

In ??, we see several chameleon simulations ($n = 0.5$, $\Phi_{\text{scr}} = 10^{-5}$) with different resolutions. We compared the resulting power spectra directly with FPA simulations with the same parameters (box size, number of particles, etc.). There are four sets of simulations with different resolutions (Nyquist frequencies), each one with a pseudo-linear prediction for the chameleon field and a non-linear result from the multigrid solver.

For lower resolutions ($k_{\text{nq}} = 0.4 \text{ hMpc}^{-1}$ and $k_{\text{nq}} = 0.8 \text{ hMpc}^{-1}$), the pseudo-linear theory predicts a higher amplitude of the power spectrum as it underestimates the screening effect on smaller scales. However, with higher resolution (and the ability to see deeper gravitational wells) this pseudo-linear prediction starts to overestimate the screening and suppress the power spectrum sooner than in the non-linear solver. It is because the correction to the solution (4.29) suppresses the chameleon force completely – not only inside massive objects but near those as well. The non-linear solution predicts suppressed forces nearby these massive objects but not completely. The exact scale when this happens is dependent on the screening potential – lower Φ_{scr} means we need a finer resolution to see deep gravitational wells where the chameleon is in the screening regime. For the choice of the screening potential as in ?? ($\Phi_{\text{scr}} = 10^{-5}$) this crossover where we cannot use the linear prediction happens at $k \sim 2 \text{ hMpc}^{-1}$. However, as FPA cannot fully resolve non-linear features on scales $k \gtrsim 1 \text{ hMpc}^{-1}$ we cannot take this scale exactly.

We can also see that even with higher resolution the power spectra on large and medium scales remain the same. This may suggest that the non-linear effects due to the coupling of different wave-numbers are small. However, as these results are coming from a quasi-linear approximation we should be cautious about such a statement. We will further explore this resolution effects of the chameleon gravity using full N -body simulations in the future.

5.2.2 Matter power spectrum

We now turn to results for the matter power spectrum; ?? shows power spectra for different chameleon parameters for modified gravity simulations with FFA and FPA.

The FFA predicts an increased enhancement of the power spectrum compared to the FPA, unlike the corresponding situation for ΛCDM . This can be understood from how dynamics are treated within the FFA. In the case of standard gravity, the velocity of a particle decreases steadily as it approaches a minimum of the gravitational potential. In the case of chameleon gravity, however, once the particle is close enough to the potential minimum such that the screening effect kicks in, the fifth force is abruptly cut off and the particle stops at the potential minimum. In the case of FPA, the particles retain their velocities inside the screened regions and the clustering effect, therefore, is not as strong.

In ??, we compare simulations with different chameleon parameters directly with FPA and FFA. For the values of the chosen screening potential ($\Phi_{\text{scr}} = 10^{-6}, 10^{-5}, 10^{-4}$) and a given resolution, the pseudo-linear prediction slightly underestimates the screening effect. The dependence of the enhancement of the power spectrum on chameleon parameters is according to our expectations. A lower value of the screening potential leads to a shorter Compton wavelength and greater effect of screening and therefore lower enhancement. The lower value of the chameleon power-law exponent leads to a longer Compton wavelength and higher screening potential $\Phi_{a,\text{scr}}$ and therefore greater enhancement. We also again see that FFA predicts greater enhancement than FPA.

In ?? we show the ratio of the power spectrum using the full non-linear solver of the chameleon field to results using pseudo-linear predictions. The enhancement of the pseudo-linear prediction on scales $k \sim 0.1 h^{-1}\text{Mpc}$ is at percent level, while again somewhat stronger for FFA.

In ??, we compare chameleon gravity to the FPA through the ratio of their power spectra for one set of chameleon parameters ($n = 0.5$, $\Phi_{\text{scr}} = 10^{-5}$) as a function of time and scale. Here we can see a comparison of a non-linear prediction as well as a comparison with the chameleon mass (at a given time). The chameleon mass is a very good indicator at which time and on what scales we should expect to see some effects of the fifth force. This can be used to improve the speed of the simulations at early times when chameleon effects are negligible.

5.2.3 Correlation function

In ??, we display the correlation function for one particular case of chameleon gravity – $n = 0.5$, $\Phi_{\text{scr}} = 10^{-5}$ at $z = 0.5$. In ??, we show the effects of different parameters of chameleon gravity through the BAO peak (amplitude, location, and width). In this plot, the BAO peak characteristics are shown relative to the non-linear prediction (at the effective time) from the emulator. Comparison is done both for FPA (left) and FFA (right). We see that chameleon generally leads to a higher amplitude of the peak, a slight shift to the higher r , and a narrower width of the peak. All these effects are stronger for FFA than for FPA (as expected).

5.2.4 Halo mass function

In ?? we compared the (relative) halo mass function for different parameters of chameleon gravity. We use the halo mass function relative to the non-linear prediction (at the effective time) from the emulator. Comparison is done both for FPA (top) and FFA (bottom). We see that for FPA in the mass range ($10^{12} - 10^{14} M_\odot$) all the simulations give very similar results and differ more outside this range. FFA shows much greater differences between individual parameters, as we have already seen in the correlation function. For both approximations, we see that the higher the screening potential Φ_{scr} the more power on small scales and therefore more massive halos. For distinguishing between different chameleon parameters we should, therefore, use the most massive halos ($M \gtrsim 10^{14} M_\odot$).

5.3 Discussion

In this chapter, we studied different approximation schemes and tested their usefulness as fast alternatives to full N -body simulations. The results for ZA and TZA are as expected. Both of these approximations may be used to make very fast predictions (no need for trajectory integration). Speed (and other computation resources) is the main advantage of ZA and TZA but at the cost

	$P_1(k)$	$P_2(k)$	amp	loc	width
FF	1.3%	8.2%	11.2%	0.4%	5.2%
FP	2.1%	8.2%	8.7%	0.3%	2.9%
TZA	11.3%	33.0%	5.2%	0.9%	13.4%
ZA	6.4%	17.2%	0.2%	0.5%	8.4%

Table 5.7: Errors of different approximation schemes at the redshift $z = 0.5$. $P_1(k)$ corresponds to an error at scale $k = 0.1 \text{ } h\text{Mpc}^{-1}$ and $P_2(k)$ at scale $k = 0.2 \text{ } h\text{Mpc}^{-1}$. Amp, loc and width are errors of the BAO peak.

of reduced accuracy. We saw that they predict very good results on large scales ($k < 10^{-2} \text{ } h\text{Mpc}^{-1}$) but structures on smaller scales are smeared out due to the line-crossing. TZA proved to work better on these smaller scales but at the cost of loss of sub-structures.

FFA and FPA have better results on our scales of interest – they predict better location and width of the BAO peak for redshifts $z \gtrsim 0.5$ than ZA or TZA. Their main disadvantage compared to the ZA or TZA is speed because we need to integrate the whole trajectory through the frozen field (velocity or gravitational potential). Although they are slower than ZA and TZA, they are still much faster than full N -body simulations. Because we do not need to compute the short range force and the density field at each time-step and the surrounding field remains (almost) constant, we can use much larger time-steps than in full N -body simulations. Because particles do not *see* each other, we can integrate their paths independently – from the starting redshift to the final one with adaptive time-step which can further improve the overall speed and accuracy.

In FFA and FPA, structures grow more slowly than in the case of the linear theory. This feature of the approximations can be fixed through mapping of the simulation time and real time. With this fix, structures grow on all scales (there is no smearing on small scales as in the case of ZA/TZA) and there are even non-linear features in the power spectrum. We also showed that this slower growth is not due to the insufficient number of time-steps as may be the case for standard PM simulations. Summary of the achieved accuracy is shown in Table 5.7.

All approximations can predict the BAO peak location to a 1% accuracy at $z = 0.5$, comparing to a non-linear theory. However, ZA and TZA predict the smoothing of the peak stronger than non-linear evolution (**2007ApJ...664..660E; 2014JCAP...02..042S**) whereas FFA and FPA weaker. All approximations predict lower amplitude and narrower width of the peak than linear theory (smoothing). ZA and TZA predict a wider peak, while FPA and FFA a narrower one, as compared to the N -body prediction. Compared to the amplitude of the BAO peak of the N -body prediction ZA and TZA give the best results for low z . However, for higher redshifts $z > 1$, FFA and FPA give better amplitude, location and width.

The broadening and shift of the acoustic peak due to the non-linear evolution of structures can be reduced by reconstruction techniques

([2007ApJ...664..675E](#)). A widely used technique is based on ZA, as described in [10.1111/j.1365-2966.2012.21888.x](#). As FFA and FPA are closer to the non-linear evolution than ZA or TZA, they could potentially be used for similar purposes.

Different approximation methods – Lagrangian perturbation theory (LPT) up to third order ([10.1093/mnras/264.2.375](#)), Truncated LPT ([1993MNRAS.260..765C](#)), Augumented LPT ([10.1093/mnrasl/slt101](#)), MUSCLE ([10.1093/mnrasl/slv141](#)) and COLA – have been tested in [2017JCAP...07..050M](#), see [??](#). Our results for ZA and TZA match theirs (on the basis of matter power spectrum accuracy at the scale $k = 0.1 h^{-1}\text{Mpc}$ and $k = 0.2 h^{-1}\text{Mpc}$, see Table 5.7). Our results for FFA and FPA show that they do better than 2LPT ($\sim 5\%$ error of $P(k)$ at $k = 0.1 h^{-1}\text{Mpc}$ at $z = 0.5$) and T2LPT ($\sim 10\%$), while having a similar accuracy as compared to 3LPT ($\sim 1\%$), A2LPT ($\sim 1\%$), A3LPT ($\sim 2\%$) and MUSCLE 2LPT ($\sim 1\%$). As expected, the particle-mesh code COLA gives the best results, especially at later time ($z = 0$).

When we applied the FPA to chameleon gravity we saw that the spatial resolution of simulations has a great impact on the resulting power spectra (on small scales). In our code, we used a fixed-size mesh. However, when entering the screening regime where high resolution is key, the use of an adaptive mesh would be a better approach. Note that the limitations of the approximations on small scales must be taken into account. This limits the highest possible resolution to $k \sim 1 h^{-1}\text{Mpc}$ that is still reasonable to use.

For studying large scales ($k \lesssim 0.1 h\text{Mpc}^{-1}$) both pseudo-linear and non-linear prediction had very similar results. We saw that the pseudo-linear solution to chameleon equations generally predicts a greater effect of the fifth force than the non-linear solution on smaller scales. On small scales ($k \gtrsim 1 h\text{Mpc}^{-1}$) the difference between the pseudo-linear and non-linear solutions became more apparent in the screening regime. The scale when this transition happens tells us where the results of linear prediction are still sufficient and when the linear prediction breaks down.

The overall success of FFA and FPA when predicting the movement of particles reveals that linear predictions of potentials can lead to good results. This could also be applied to a non-linear solver for the chameleon equations where the linear prediction is relatively close to the non-linear one on large scales and at early times. For now, at each time-step we recomputed the chameleon field. But in principle we can compute the chameleon field only once in a while – depending on the background chameleon values and the number of regions in the screened regime – and evolve the chameleon field according to the linear theory in between.

To sum up, we showed that simple methods like FFA and FPA, which are very easy to implement even for modified theories of gravity, can predict results at BAO scales that are comparable with significantly more complex methods such as second-order Lagrangian perturbation theory. This makes their further study worthwhile, including implementations for other modified gravity models. ~~Cosmological Surveys There are many projects and missions which study properties of the dark energy, either as a main scientific goal or as a complementary program. Among the big surveys are e.g. Sloan Digital Sky~~

Surveys (SDSS, **SDSS**) which aims to create the most detailed three-dimensional maps of the Universe. From the beginning of regular surveys in 2000 till 2014 there were seven finished surveys in total (SDSS-I/II results **SDSS-I/II**, SDSS-III results **BOSS results**), while there are three ongoing surveys from 2014 (SDSS-IV, [2017AJ....154...28B](#)) and a planned panoptic spectroscopic survey (SDSS-V, [2017arXiv171103234K](#)) which will start collecting data in summer 2020. Other surveys are e.g. Wilkinson Microwave Anisotropy Probe (WMAP, **WMAP**, results **WMAP results**); Planck (**planck**, results **planck cosm**). There are also several planned surveys almost ready to start collecting data Euclid, LSST or WFIRST. Some parts of this chapter are based on the author's work **mastersthesis vrastil**. BOSS The Sloan Digital Sky Survey's (SDSS-III) Baryon Oscillation Spectroscopic Survey (BOSS) is a six-year program (Fall 2009 – Spring 2014) that uses the wide field 2.5-m telescope at Apache Point Observatory, see . The BOSS is designed to measure the scale of baryonic acoustic oscillations (BAO, see) in the clustering of matter over a larger volume than the combined efforts of all previous spectroscopic surveys of large-scale structures. BOSS uses 1.5 million luminous galaxies to measure BAO to redshifts $z < 0.7$. Observations of neutral hydrogen in the Ly α forest in more than 150,000 quasar spectra constrain BAO over the redshift range $2.15 < z < 3.5$ BOSS. Sloan Foundation 2.5m Telescope. *Credit:*

There are two double spectrographs, each covering the wavelength range 361 nm – 1014 nm with resolution $R = \lambda/\Delta\lambda$ ranging from 1300 at the blue end to 2600 at the red end. Both spectrographs have a red channel with a 4k \times 4k, 15pixel CCD from Lawrence Berkeley National Laboratory (LBNL). Both spectrographs have a blue channel with a 4k \times 4k, 15pixel CCD from e2v. The instrument is fed by 1000 optical fibers (500 per spectrograph), each subtending 2'' on the sky.

Using the acoustic scale as a physically calibrated ruler, BOSS determines the angular diameter distance with a precision of 1% at redshifts $z = 0.3$ and $z = 0.57$ using the distribution of galaxies and measurements of $H(z)$ to 1.8% and 1.7% at the same redshifts. At redshifts $z \sim 2.5$ the angular diameter distance and $H^{-1}(z)$ is measured to an accuracy of 1.9% using Ly α forest.

BAO measurements with the CMB-calibrated physical scale of the sound horizon and SN data yields of $H_0 = (67.3 \pm 1.1) \text{ km} \cdot \text{s}^{-1} \text{ Mpc}^{-1}$ with 1.7% precision **BOSS results**, see . This measurement assumes standard pre-recombination physics but is insensitive to assumptions about dark energy or space curvature. When we allow more general forms of evolving dark energy, the BAO+SN+CMB parameter constraints are always consistent with flat Λ CDM values at 1σ . While the overall χ^2 of model fits is satisfactory, the Ly α forest BAO measurements are in moderate ($2 - 2.5\sigma$) tension with model predictions. Models with early dark energy that tracks the dominant energy component at high redshift remain consistent with expansion history constraints, and they yield a higher H_0 and lower matter clustering amplitude, improving agreement with some low-redshift observations. BAO measurements and model predictions of $H(z)$ and $D_M(z)$ as a function of redshift, with physically informative scalings. The top panel shows $H(z)/(1+z)$, the proper velocity between two objects 1 comoving Mpc apart. The bottom panel shows $c \ln(1+z)/D_M(z)$,

a scaling that matches a constant line $H(z) = (1+z)H_0$ in the top panel to the same constant line in the bottom panel for a flat universe. Filled circles and squares show the BOSS CMASS and Ly α forest measurements of $H(z)$ and $D_M(z)$, respectively; we show the Ly α forest quasar cross-correlation as crosses to distinguish from the Ly α forest auto-correlation measurements. Filled triangles in the bottom panel show the BOSS LOWZ and MGS measurements of $D_V(z)$ converted to $D_M(z)$. Open squares show the value of $H_0 = 67.3 \pm 1.1$ km·s $^{-1}$ Mpc $^{-1}$ determined from the combination of BAO and SN Ia data. The grey swath in both panels is the prediction from the Planck Λ CDM cosmology including 1σ parameter errors; in the top panel, one can easily see the model transition from deceleration to acceleration at $z \approx 0.6$. The dashed line shows the Λ CDM prediction using the best-fit WMAP parameters, which has lower $\Omega_m h^2$. Dotted curves show models that match the best-fit Planck values of ω_b , w_b , and $D_M(1090)/r_d$ but have $\Omega_k = 0.01$ (blue), $w = -0.7$ (green), or $w = -1.3$ (red). The x -axis is set to $\sqrt{1+z}$ both for display purposes and so that a pure matter universe ($\Omega_m = 1$) appears as a decreasing straight line on the top panel.

Note: Reprinted from BOSS results. eBOSS The Extended Baryon Oscillation Spectroscopic Survey (eBOSS, 2016AJ....151...44D) is the new cosmological survey within a SDSS-IV six-year program started in 2014 July. eBOSS will conduct novel cosmological observations of galaxies, and in particular quasars, using the same 1000-fiber optical spectrographs as those in BOSS at Apache Point Observatory. These observations will be conducted simultaneously with the Time-Domain Spectroscopic Survey (TDSS, 2015ApJ...806..244M) designed for variability studies and the Spectroscopic Identification of eROSITA Sources (SPIDERS, 2010SPIE.7741E..1NF) program designed for studies of X-ray sources.

eBOSS will map the large-scale structures over the relatively unconstrained redshift range $0.6 < z < 2.2$, see for comparison with the BOSS range. eBOSS will expand the selection of luminous red galaxies (LRG) beyond that probed by BOSS and obtain better than a 1.0% precision distance estimate when combined with the $z > 0.6$ tail of the BOSS galaxy population. With observations of a new sample of emission-line galaxies (ELG) eBOSS will produce a 2.0% precision distance estimate at higher redshifts. eBOSS will obtain a 1.8% precision distance estimate in the redshift range $0.9 < z < 2.2$ using quasars that have luminosities and areal densities well-suited to the sensitivity of the BOSS spectrographs. Finally, eBOSS will sharpen the BOSS Ly α forest measurements by a factor of 1.44 with a new selection of $z > 2.1$ quasars, providing stronger leverage on the history of dark energy. Planned eBOSS coverage of the Universe. *Credit:*

With four classes of spectroscopic targets (LRG, ELG, quasar, Ly α forest quasar), eBOSS will enable the first high precision distance measurements in the epochs when dark energy emerged as the dominant dynamical component of the Universe. In addition to BAO distance measurements, eBOSS will provide new tests of GR on cosmological scales through redshift-space distortions (RSD), new tests for non-Gaussianity in the primordial density field, and new constraints on the summed mass of all neutrino species. DES The Dark Energy Survey (DES) is designed to probe the origin of the accelerating universe and to help uncover the nature of dark energy by measuring the 14-billion-year history of cosmic

expansion with high precision. DES is an optical near-infrared survey of 5000 deg² of the South Galactic Cap up to absolute magnitude $r \sim 24$ in the *grizy* spectrum. DES's instrument consists primarily of a new camera, Dark Energy Camera (DECam), specifically designed to be sensitive to the highly redshifted light from distant galaxies. DECam is mounted on a classic telescope, the Blanco 4-m telescope at the Cerro Tololo Inter-American Observatory (CTIO) in La Serena, Chile. The imaging system is supported by a combination of microwave and optical data links that will provide the recorded data to the survey members. Starting in August of 2013 and continuing for five years, DES has begun to survey a large swath of the southern sky out to vast distances in order to provide new clues to these most fundamental questions DES.

DECam operating at night, while an observer watches. *Credit:* The survey data allow to measure the dark energy and dark matter densities and the dark energy equation of state through four independent methods: galaxy clusters (counts and spatial distributions at $0.1 < z < 1.3$), weak gravitational lensing tomography (on several redshift shells to $z \sim 1$), galaxy angular clustering, and supernova distances (at $0.3 < z < 0.8$).

The main tool is the DECam, 74 2k × 4k 570 Mpx digital camera built at Fermilab in Batavia. It provides a 2.2° field of view image at 0.27"/pixel. It covers the wavelength range 400 – 1100 nm with five filters (*grizy*). The electronics will allow an entire digital image to be read out and recorded in 17 seconds, time that it takes the telescope to move to its next viewing position.

From the first two years of observation, a mass map from weak gravitational lensing shear measurements over 139 deg² has been reconstructed DES mass. There is a good agreement between the mass map and the distribution of massive galaxy clusters identified using a red-sequence cluster finder. These measurements are consistent with simulated galaxy catalogs based on Λ CDM N -body simulations, suggesting low systematics uncertainties in the map.

In [2019PhRvL.122q1301A](#) the DES collaboration presented their cosmological constraints for w CDM: $\Omega_m = 0.300^{+0.023}_{-0.021}$, $\Omega_b = 0.064^{+0.013}_{-0.009}$, $\Omega_\Lambda = 0.700^{+0.021}_{-0.023}$, $w = -0.80^{+0.09}_{-0.11}$ and $\sigma_8 = 0.786^{+0.029}_{-0.019}$. Constraints on the dark energy equation of state w and Ω_m for w CDM are also shown in .

Constraints on the dark energy equation of state w and Ω_m in a w CDM model with fixed curvature ($\Omega_k = 0$) and marginalized neutrino mass density. They compared constraints from the DES data alone (black contours) to the best available external data (green contours), but also showed the impact of including a low-redshift SNe Ia data set (Low z) to anchor the DES SNe Ia (blue contours). Each component of the DES analysis was fully blinded. Reprinted from [2019PhRvL.122q1301A](#). Euclid Euclid is an ESA (European Space Agency) high-precision space mission in ESA's Cosmic Vision 2015 – 2025 scientific program designed to map the geometry and evolution of the universe and to study properties of dark matter and dark energy. Its primary goal is to place high accuracy constraints on dark energy, dark matter, gravity, and cosmic initial conditions using two independent cosmological probes – weak gravitational lensing and baryonic acoustic oscillation – out to redshift $z \sim 2$. Galaxy clusters and the Integrated Sachs-Wolfe effect will be used as secondary cosmological probes. Along with these tasks will Euclid's visible and near-infrared imaging

and spectroscopy of the entire extragalactic sky produce legacy science for various fields of astronomy, e.g. galaxy evolution, large-scale structures, or the search for high-redshift objects. The Euclid mission has been adopted with the mission's time-frame for liftoff starting in mid-2022 from the Guiana Space Centre, Europe's Spaceport in French Guiana. The overview of the Euclid system design and scientific requirements can be found in [2011arXiv1110.3193L](#). Structural and thermal model of the Euclid satellite. *Credit:* Vera C. Rubin Observatory The Vera C. Rubin Observatory project, previously known as the Large Synoptic Survey Telescope, will conduct the 10-year Legacy Survey of Space and Time (LSST, lsst). LSST is a ground-based telescope being built in northern Chile on the Cerro Pachón mountain in the northern Chilean Andes. The system will produce a 6-band (300–1100 nm) wide-field deep astronomical survey over 20,000 deg² of the southern sky. Combining the wide-field of view with short exposures, the LSST will take more than 800 images each night and cover the whole observable sky twice each week. Each patch of the sky will be visited about 1000 times during ten years. The LSST will provide an unprecedented depth (single-visit 24.5 mag, co-added 27.5 mag) and unique details of the Universe while producing 30 terabytes of data nightly. This data will be used for locating dark matter and to characterize the properties of the dark energy. Other major tasks for the LSST will be detecting and tracking potentially hazardous asteroids or studying the structure of the Milky Way. The project is in the construction phase and will begin its full science operations in 2022. The exterior of the summit facility building is nearly complete, see . Inside, major components of the telescope have begun to arrive from their places of manufacture around the globe, including the mirror washing and coating equipment, and the Secondary Mirror (M2) and its support system.

On January 6, 2020, it was announced that the LSST will be named the NSF (National Science Foundation) Vera C. Rubin Observatory (Rubin Observatory) after an astronomer who provided important evidence of the existence of dark matter. NSF also announced on January 6, 2020, that the telescope at the Rubin Observatory will be named the Simonyi Survey Telescope in recognition of the significant private donation made through the Corporation early in the construction phase in support of the design, development, and fabrication of the telescope's primary mirror. Construction on the Vera C. Rubin Observatory. Most of the large pieces of equipment have arrived on the summit, and the installation of the Telescope Mount Assembly (TMA) began in early 2020. *Credit:*

The LSST Data Management (DM) is responsible for creating the software, services, and systems which will be used to produce LSST's data products. DM is required to generate and process a set of data products and to make them available to scientists and the public .

Telescope and camera The LSST telescope consists of three aspheric mirrors – an 8.4-m primary M1, a 3.4-m convex secondary M2 (the largest convex mirror ever made), and a 5.0-m tertiary M3. The primary mirror is highly annular having an outer clear aperture of 8.36 m and an inner diameter of 5.12 m, giving an effective collecting area of a 6.67-m filled aperture. The camera body and its associated readout electronics are located in the 1.8-m

~~diameter hole in the secondary mirror. The hole in the tertiary mirror is used to mount equipment for the maintenance of the LSST optical alignment. The primary and tertiary mirrors form a continuous surface without any vertical discontinuities. The M1-M3 monolith (see) was completely formed and polished in February 2015 and in early 2019 it was shipped to the summit facility on Cerro Pachón. The LSST Primary/Tertiary Mirror (M1M3) in the Richard F Caris Mirror Lab at the University of Arizona for optical testing. In May 2019, the mirror reached its new home in the Andes Mountains of Northern Chile.~~*Credit:*

~~The LSST camera with the size of 1.6 meters by 3 meters and the weight of 2800 kilograms will be the largest digital camera ever constructed. It will produce data of extremely high quality with minimal downtime and maintenance. It is a large aperture, wide-field optical (0.3—1°) imager designed to provide a 3.5° field of view with sampling better than 0.2''. The image surface is flat with a diameter of approximately 64 cm. Used detectors are 16 Mpixel silicon detectors providing a total of approximately 3.2 Gpixels with readout in 2 sec (15 sec integration). The camera has 6 filters (*ugrizy*) and is located in the middle of the telescope.~~

~~The focal plane consists of 189 arrays ($\sim 16 \text{ cm}^2$ each, 3200 cm^2 focal plane) of $4\text{k} \times 4\text{k}$ CCDs which should ensure a wide field of view while filling the focal plane without any large gaps (less than a few hundred) — the fill factor is 93%. High-resistivity silicon substrate and high applied voltages with small pixel sizes will produce low point spread function ($\text{PSF} \ll 0.7''$). Other focal plane requirements include high quantum efficiency (QE) from 320 to 1080 nm, fast f/1.23 focal ratio, high throughput fast readout (2 sec), or low read noise .~~

~~Dark Energy Science Collaboration~~ The LSST Project Team has been assembled to design and build the telescope, camera, and data management systems but it is not a scientific collaboration in the usual sense. While scientists working on the LSST Project are interested in the scientific questions that LSST data can address, they are not officially involved in the scientific analyses of those data and have no privileged access to LSST data or software. Therefore, a number of quasi-independent scientific collaborations, which provided advices on technical issues and helped articulate the scientific case for the LSST, have created the LSST Dark Energy Science Collaboration (DESC) in 2012 during a meeting at the University of Pennsylvania.

~~DESC prepares a variety of cosmological analyses for the LSST survey. In advance of LSST's first observations, the DESC helps prepare for the LSST science analysis, make synergistic connections with ongoing cosmological surveys, and provide the dark energy community with state-of-the-art analysis tools. The primary goal of the DESC is the study of dark energy and related topics in fundamental physics with data from the LSST. For more information see the DESC's white paper [desc:white](#).~~

~~Planck~~ The Planck mission ([planck](#)) was a European Space Agency mission with significant participation from NASA. It was launched into space on May 14, 2009, and was orbiting the second Lagrange point of our Earth-sun system, about 1.5 million km (930,000 miles) away. Planck was measuring the Cosmic Microwave Background (CMB) over a broad range of far-infrared

wavelengths, and to unprecedented accuracy. Its ultimate goal was to determine the geometry and contents of the Universe, and which theories describing the birth and evolution of the Universe are correct. Planck operated beyond its nominal operational lifetime. It was turned off on 23 October 2013, after nearly 4.5 years soaking up the relic radiation from the Big Bang and studying the evolution of stars and galaxies throughout the Universe's history.

The Planck satellite. *Credit:* The Planck spacecraft was 4.2 meters high and had a maximum diameter of 4.2 meters, with a launch mass of around 1.9 tonnes. The spacecraft comprised a service module, which housed systems for power generation and conditioning, attitude control, data handling and communications, together with the warm parts of the scientific instruments, and a payload module. The payload module consisted of the telescope, the optical bench, with the parts of the instruments that needed to be cooled – the sensitive detector units – and the cooling systems.

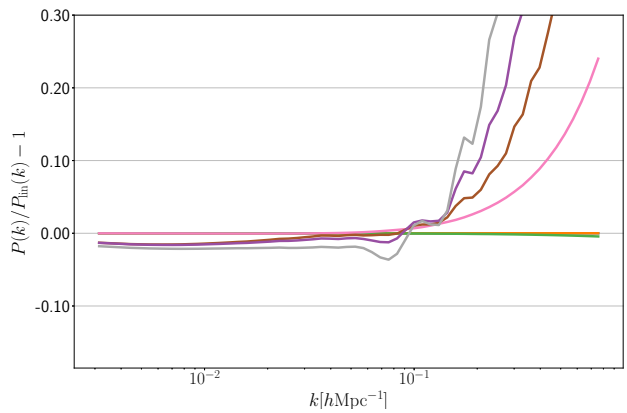
Since the end of the mission in October 2013, the Planck Collaboration has subsequently released all their data which now constitute the Planck Legacy Archive (PLA) containing all public products originating from the Planck mission. On 17 July 2018 ESA and the Planck Collaboration have released to the public a new and improved version of the data acquired by the Planck satellite, which constitutes the final official release from Planck.

The data from Planck have allowed cosmologists to set very tight constraints on many parameters of the standard model, including the Hubble constant, the densities of baryonic matter, dark matter and dark energy, and the spectral index (for Planck results, see [planck cosm](#)). Nancy Grace Roman Space Telescope The Nancy Grace Roman Space Telescope (formerly known as WFIRST, the Wide Field Infrared Survey Telescope) is a NASA large space mission designed to settle essential questions in dark energy, exoplanets, and infrared astrophysics. It is designed to perform wide-field imaging and slitless spectroscopic surveys of the near-infrared sky. The current Astrophysics Focused Telescope Assets (AFTA) design of the mission makes use of an existing 2.4 m telescope to enhance sensitivity and imaging performance. It is the top-ranked large space mission in the New Worlds, New Horizons (NWNH) Decadal Survey of Astronomy and Astrophysics. The main instrument is a wide-field multi-filter NIR imager and spectrometer. With the 2.4 m telescope, a coronagraph instrument has been added to the payload for direct imaging of exoplanets and debris disks. WFIRST was approved for development and launch in 2016 and the mission should start in the mid 2020s [WFIRST report](#).

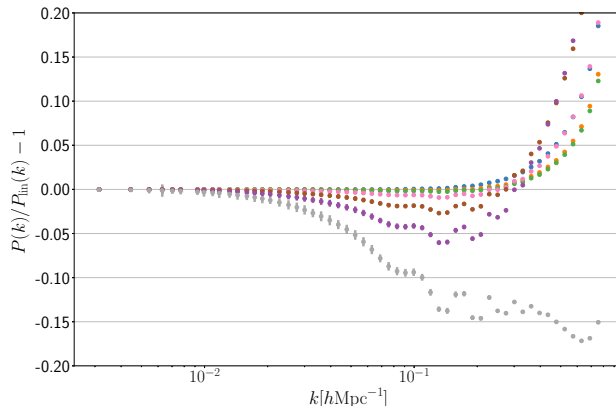
Primary Mirror Assembly. *Credit:* The mission will feature strategic key science programs plus a large program of guest observations. The main focus is on the dark energy and fundamental cosmology (determine the expansion history of the Universe and the growth history of its largest structures). The next scientific goal is discovering of exoplanets – by microlensing photometric survey of the Galactic bulge and by a direct high-contrast imaging and spectroscopic survey of the nearest stars. Data for general astrophysics science will be gathered by surveys at high Galactic latitudes and Galactic bulge. A relatively huge priority is assigned to the guest observer science program.

The payload features a 2.4 m telescope, which feeds the wide-field instrument (wide-field channel and an integral field unit spectrograph channel) and the coronagraph instrument. The wide-field channel covers a wavelength range of 0.76–2.0 and a spectroscopy mode covering 1.35–1.89. The wide-field focal plane uses $18\text{--}4\text{k} \times 4\text{k}$ HgCdTe detector arrays. The integral field unit channel uses an image slicer and spectrograph to provide individual spectra of each slice covering the 0.6–2.0 spectral range. The coronagraph instrument provides high-contrast imaging and spectroscopy. Direct imaging is provided over a band pass of 430–970 nm, while spectroscopy is provided by the spectrograph over the spectral range of 0.6–0.97 with a spectral resolution of $R \sim 70$ **WFIRST report**.

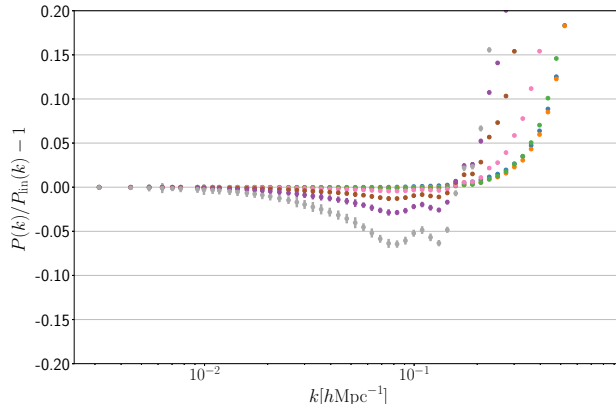
As WFIRST will be a NIR mission it will require visible band photometry for photo-z determination. LSST will be the premier ground-based facility to provide those data. As for Euclid, the baryon acoustic oscillation spectroscopic survey will be helpful for calibrating photo-z determinations for LSST. The comparison of shear determinations between WFIRST and LSST measurements will be useful for understanding shape measurement systematics with both facilities.



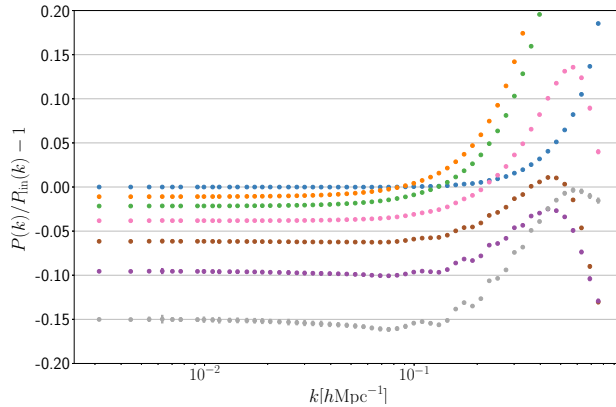
(a) Λ CDM (nl)



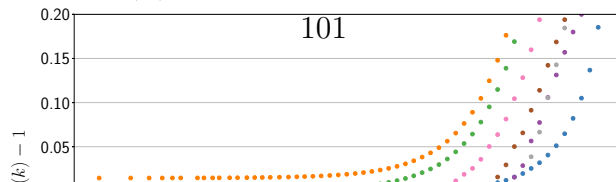
(b) Zel'dovich approximation



(c) Truncated Zel'dovich approximation



(d) Frozen-flow approximation



101

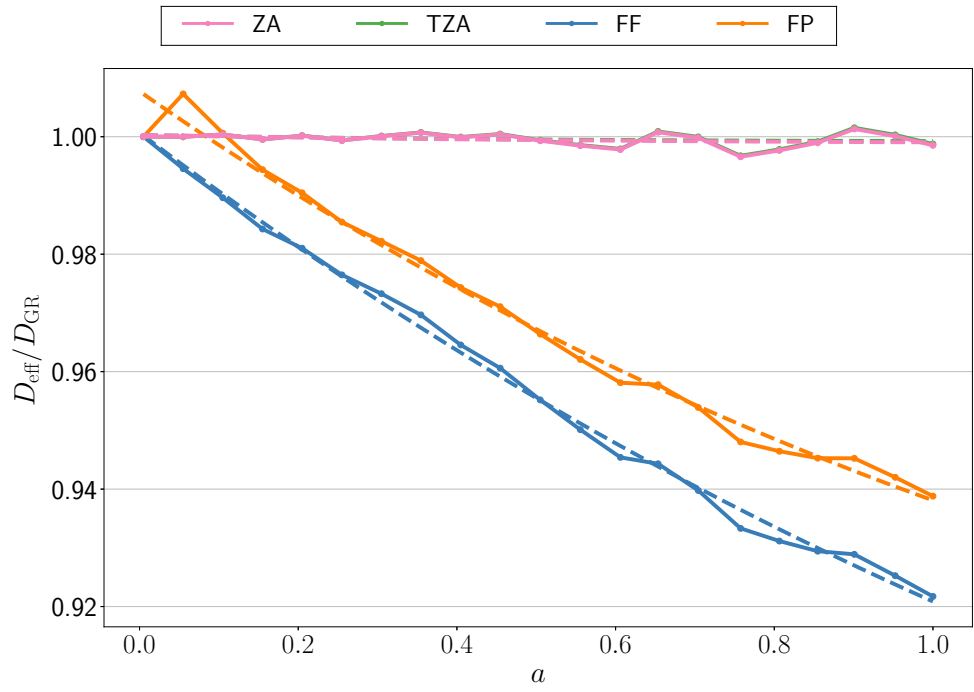


Figure 5.3: Effective growth factor D_{eff} for different approximation schemes based on the ratio of power spectrum on large scales compared to the linear prediction.

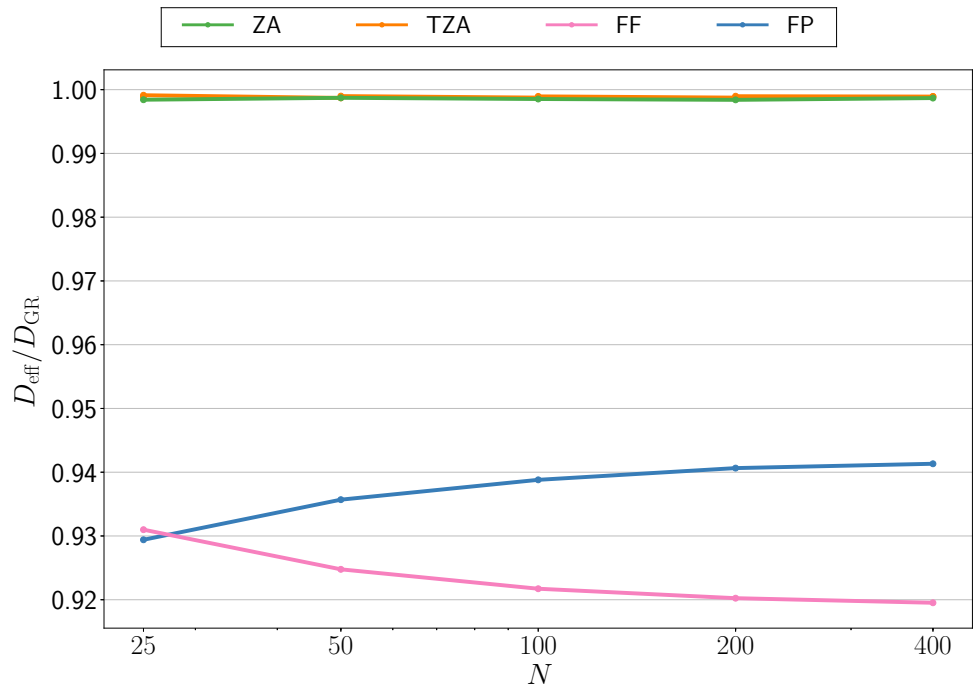


Figure 5.4: Effective growth factor D_{eff} at $z = 0$ for FFA and FPA as a function of the number of time-steps.

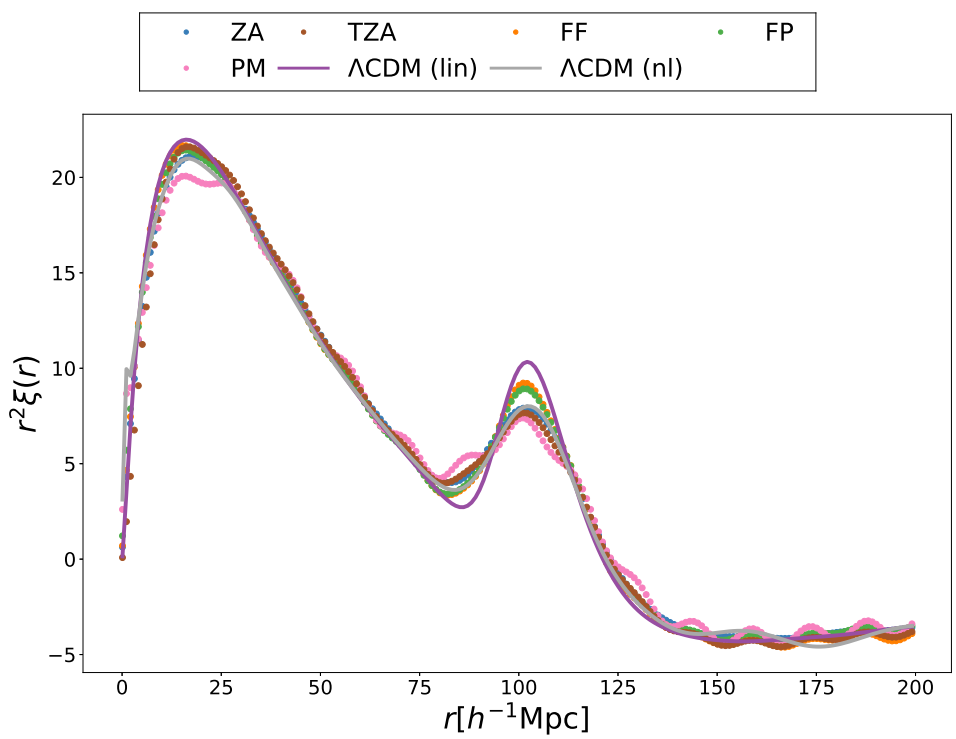


Figure 5.5: Two-point correlation function for different approximation schemes at $z = 0.5$

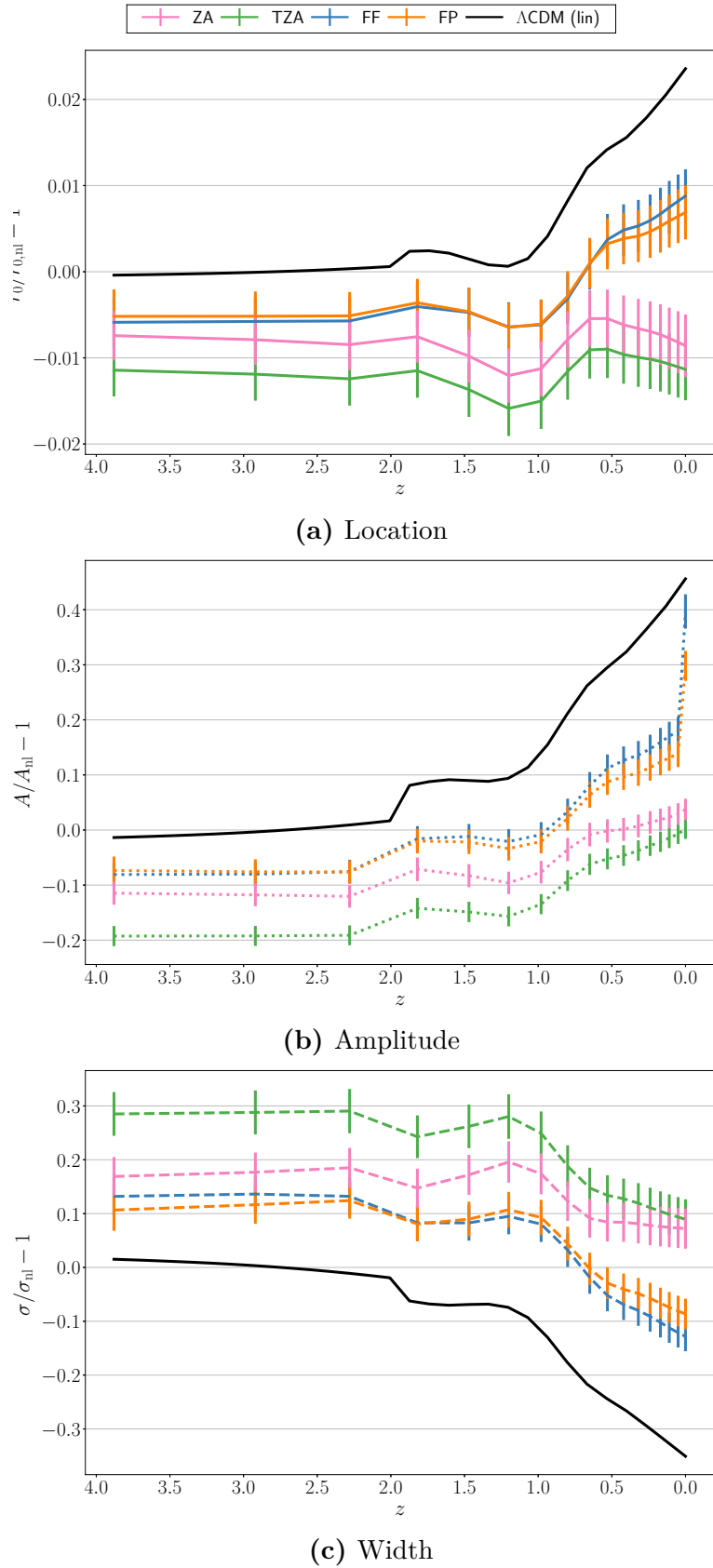
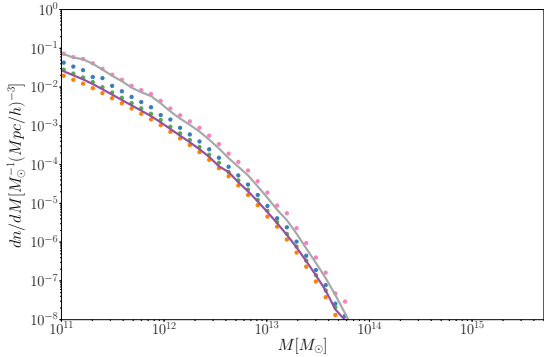
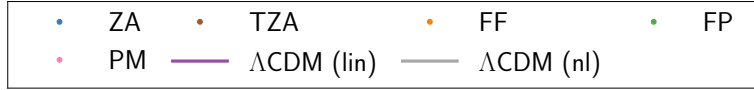
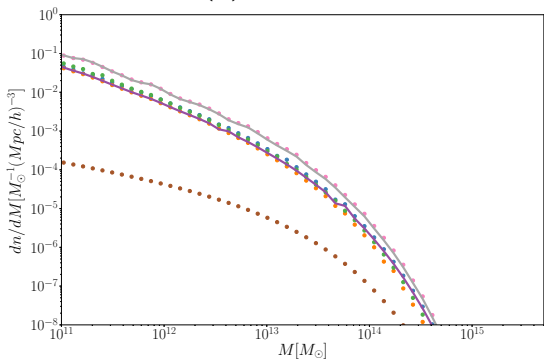


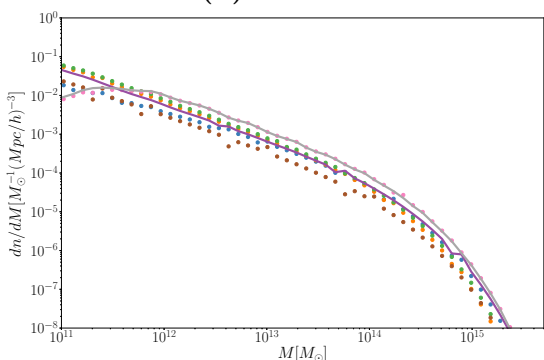
Figure 5.6: Location, amplitude and width of the BAO peak (relative to the non-linear prediction) as a function of the redshift.



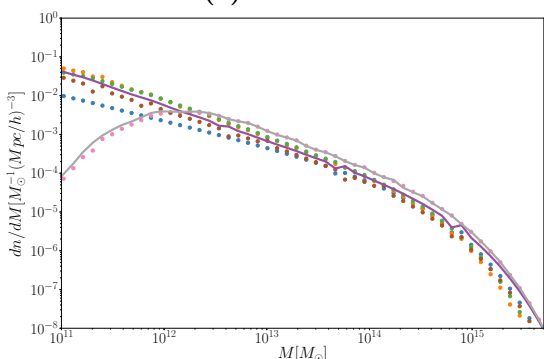
(a) $z = 3.88$



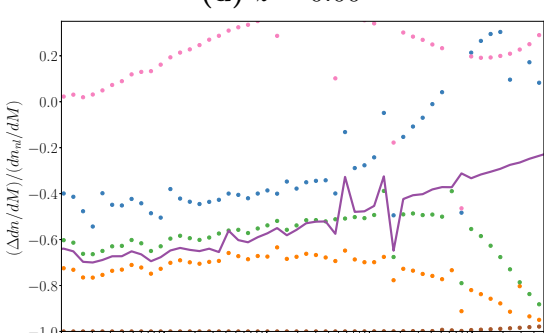
(b) $z = 1.82$



(c) $z = 0.53$



(d) $z = 0.00$



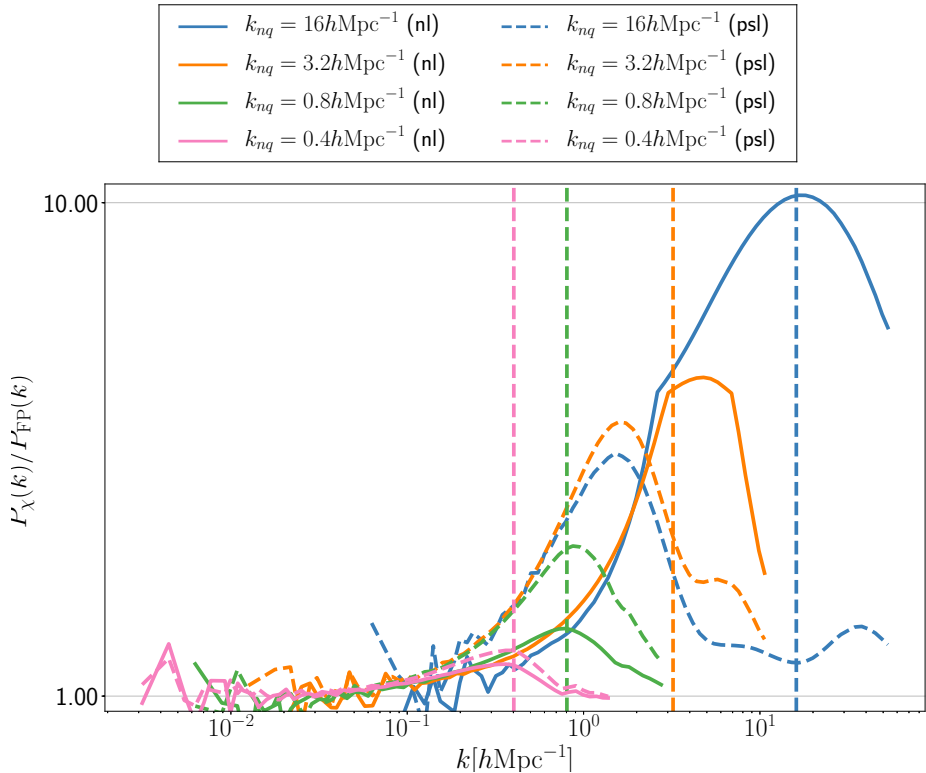


Figure 5.8: Ratio of the power spectrum of chameleon gravity to FPA with different resolutions of simulations. All simulations have $n = 0.5$, $\Phi_{\text{scr}} = 10^{-5}$. Dotted lines show the pseudo-linear prediction of the chameleon field whereas solid lines show results for the full non-linear multigrid solver for the chameleon field. Dashed vertical lines show locations of corresponding Nyquist frequencies.

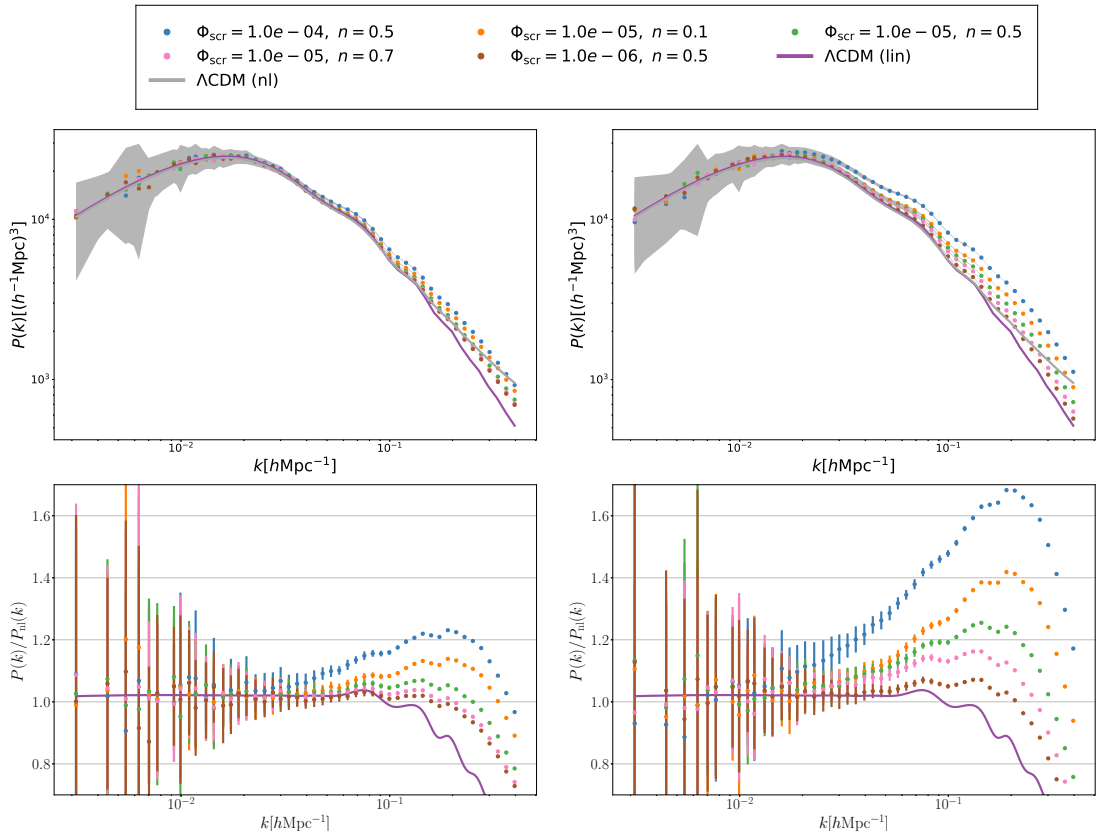


Figure 5.9: Matter power spectrum $P(k)$ at redshift $z = 0$ for different chameleon parameters. On the left are results using FPA whereas on the right results using FFA. Grey areas represent variations across different runs. Higher screening potential leads to greater enhancement of the power spectrum due to the fifth force.

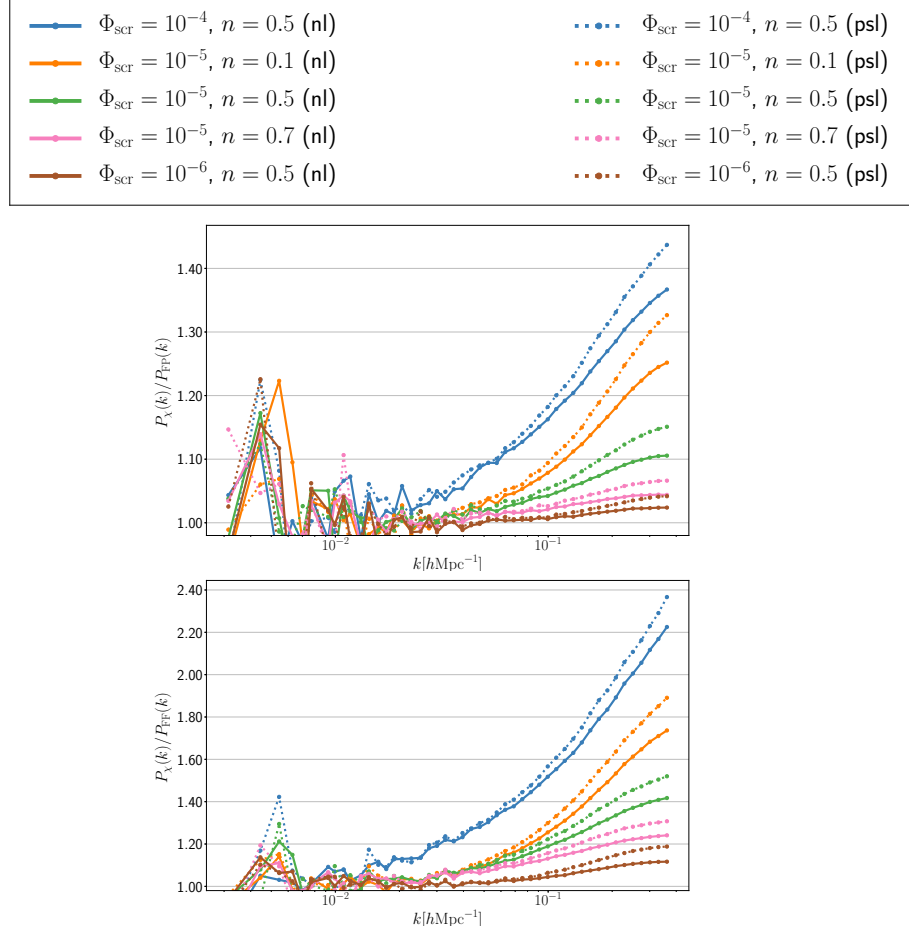


Figure 5.10: Ratio of the power spectrum of chameleon gravity to FPA (left) and FFA (right) with different chameleon parameters. Dotted lines show the pseudo-linear prediction of the chameleon field whereas solid lines show results for the full non-linear multigrid solver.

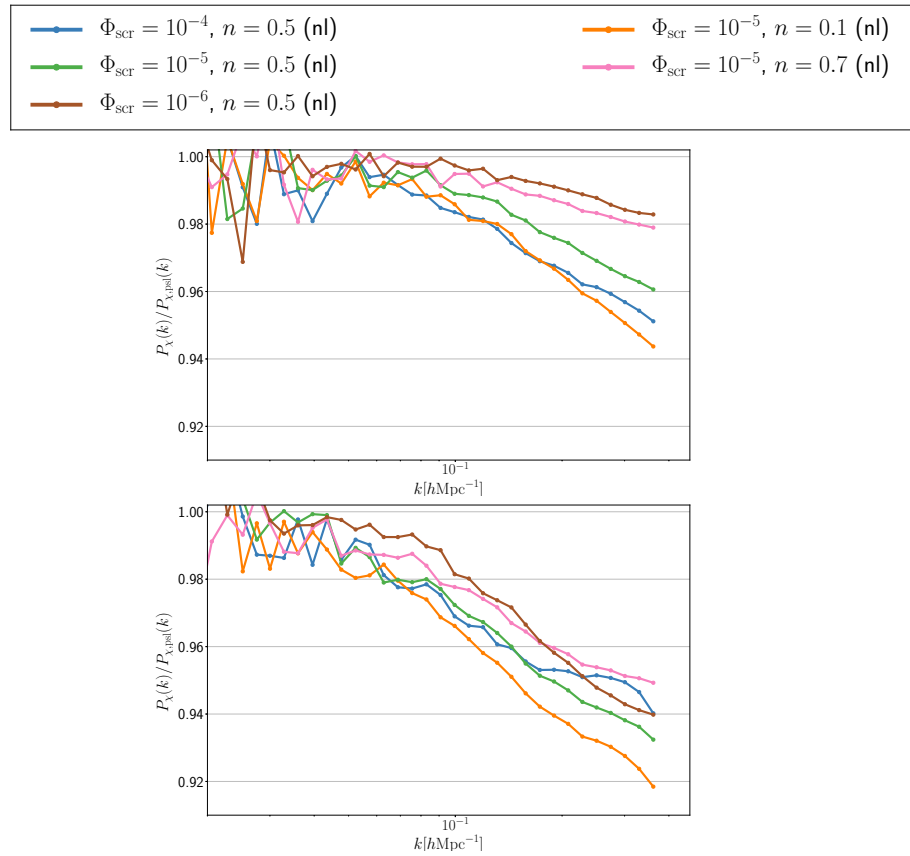


Figure 5.11: Ratio of the power spectrum of chameleon gravity to pseudo-linear prediction using FPA (left) and FFA (right) with different chameleon parameters.

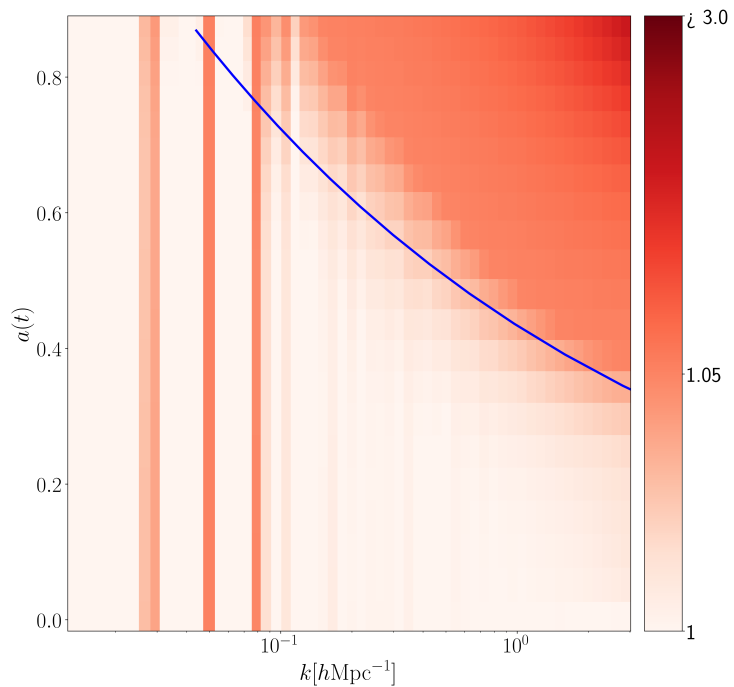


Figure 5.12: Ratio of the FPA power spectrum in chameleon gravity ($n = 0.5$, $\Phi_{\text{scr}} = 10^{-5}$) to the simulation run with standard gravity as a function of time. The blue solid line is a chameleon mass (2.61).

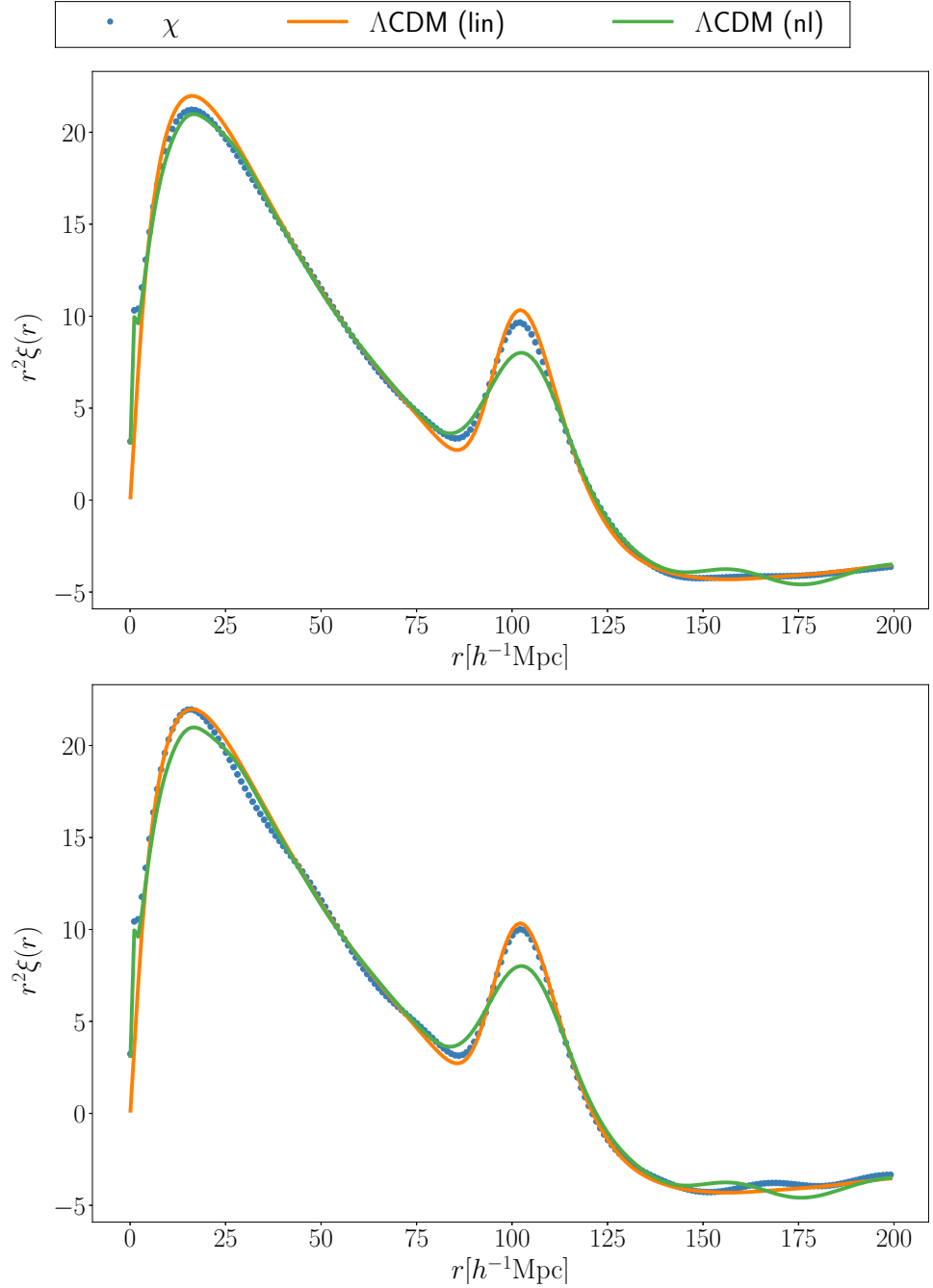
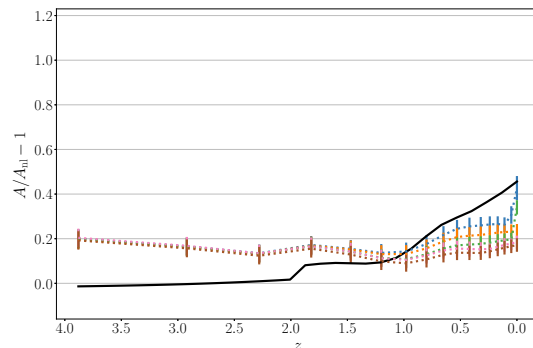
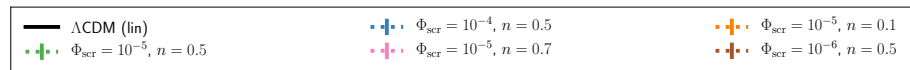
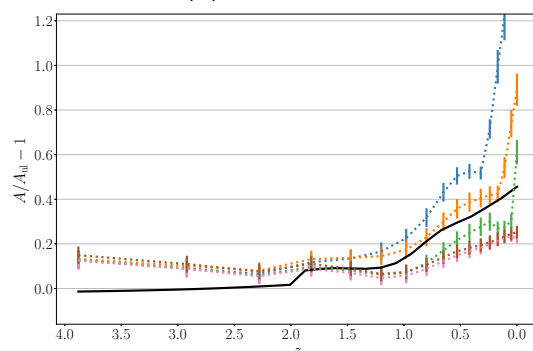


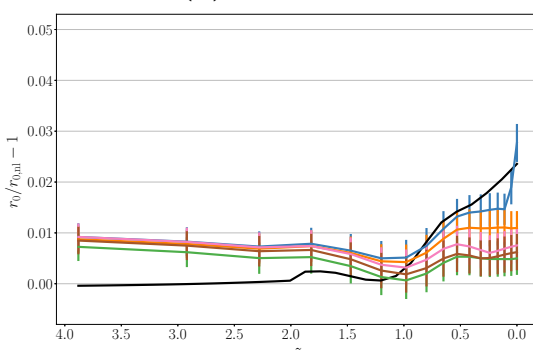
Figure 5.13: Correlation function for chameleon gravity ($n = 0.5$, $\Phi_{\text{scr}} = 10^{-5}$) at $z = 0.5$. On the top are shown results using FPA whereas on the bottom using FFA.



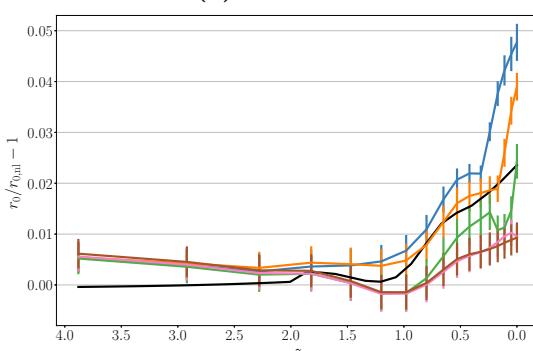
(a) Amplitude



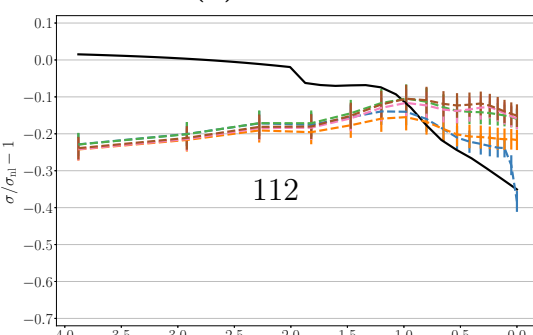
(b) Amplitude



(c) Location



(d) Location



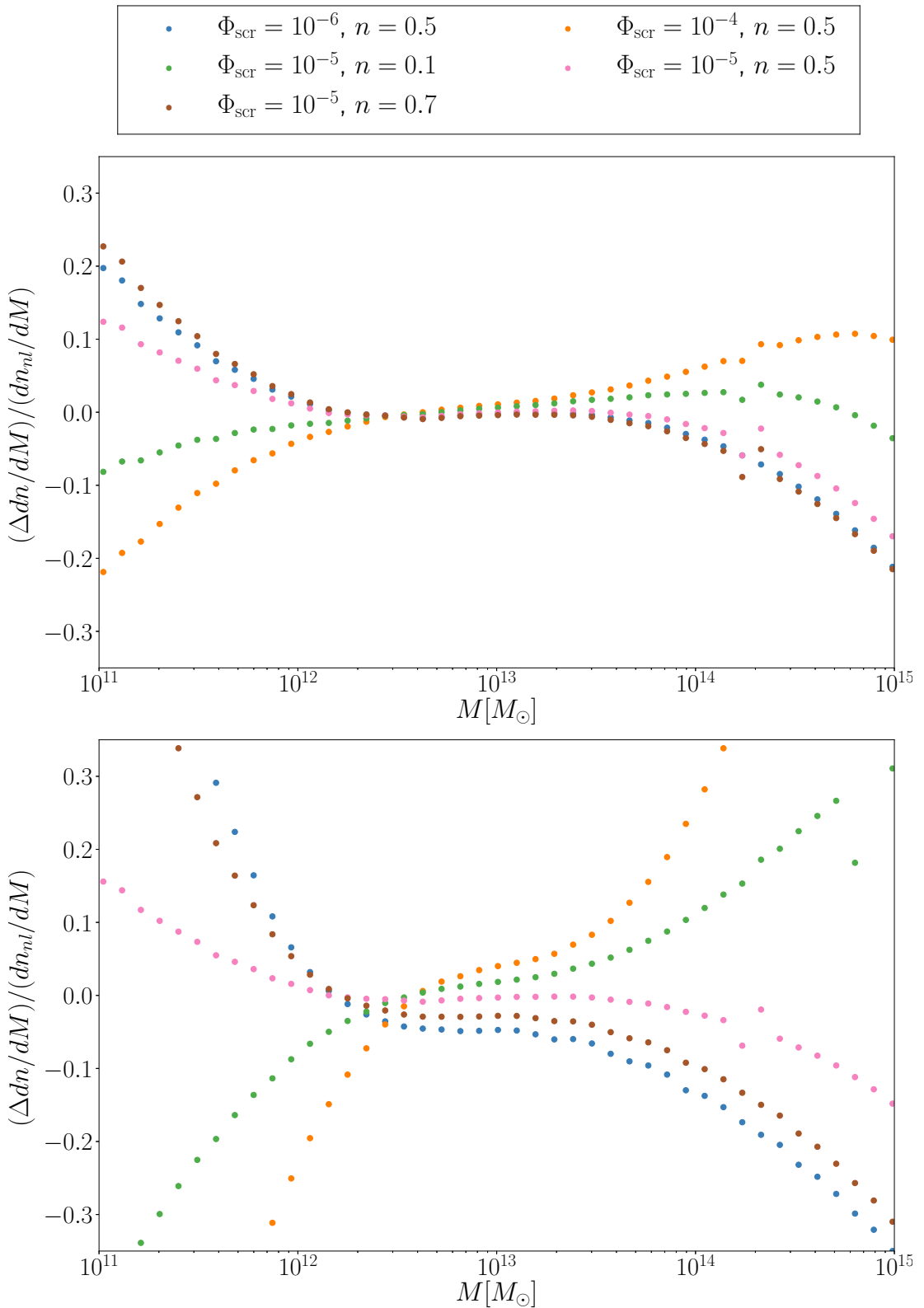


Figure 5.15: Halo mass function (relative) for non-linear chameleon gravity with different chameleon parameters. On the top are shown results using FPA whereas on the bottom using FFA.

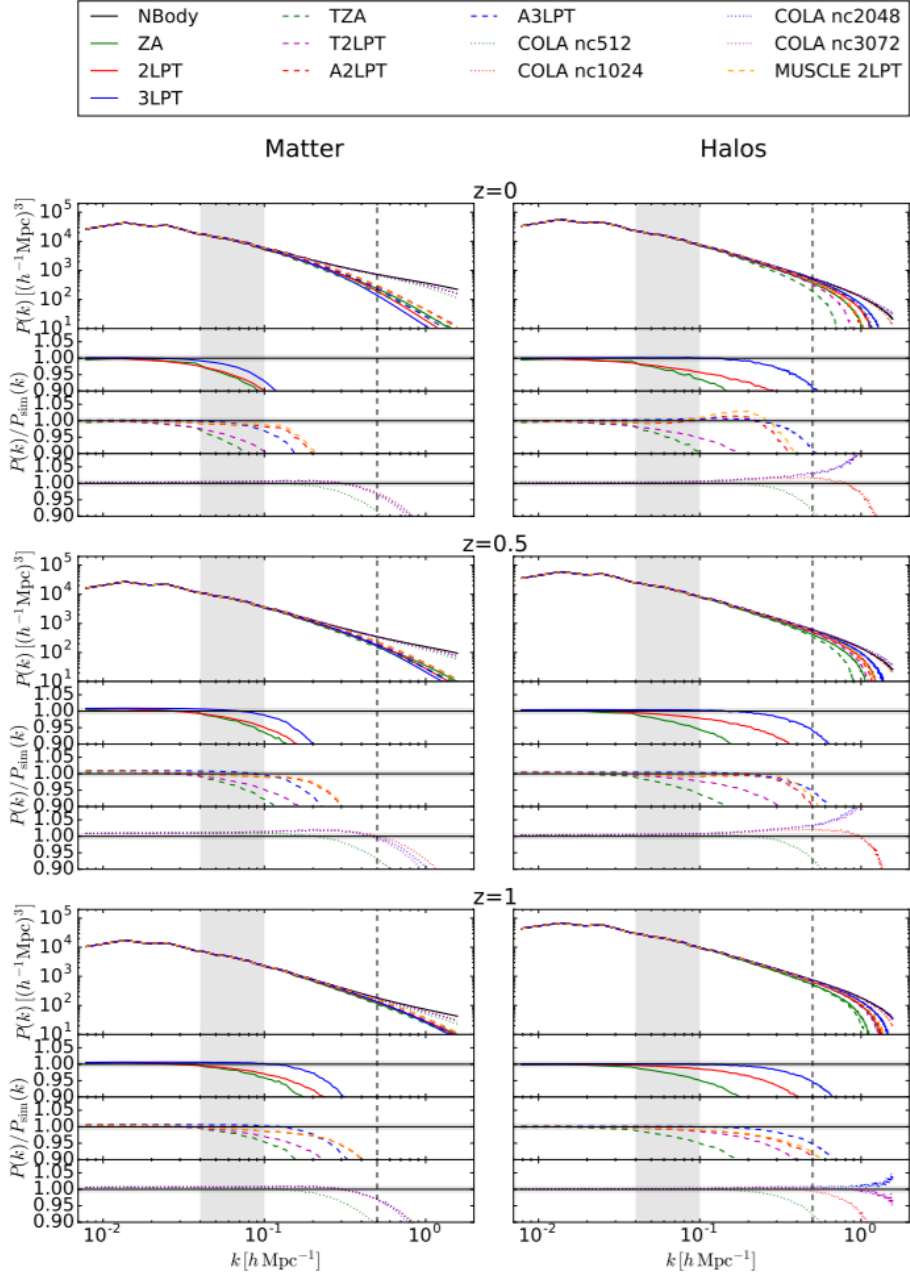


Figure 5.16: Power spectrum at $z = 0$, 0.5 , and 1 (top, middle, and bottom panels, respectively) in real space and ratio with the N -body's one for the matter field (left panels) and the halo catalogs (right panels). The vertical dashed line locates the $k = 0.5 \text{Mpc}^{-1}$ where the one-halo term becomes significant. The vertical shaded area locates the region of the BAO peak, while the horizontal one locates the 1% accuracy region. Note: Reprinted from **2017JCAP...07..050M**.

5. Outlook

In the thesis, we explored different ways to study modified gravities. The work was focused on quasi-linear regimes as the full non-linear behavior of modified gravities is hard to study due to its numerical difficulties. We showed what behavior one can expect on scales ranging from stars to that of superclusters. The implemented methods were tested on the example of the chameleon gravity and showed interesting results. These prepared techniques can now be used to explore other modified gravities.

In chapter 2 we studied the properties of the chameleon gravity in spherical systems – stars and in NFW halos both on scales of galaxies and clusters of galaxies. Although the results showed that the Hu-Sawicki $f(R)$ theory is screened in this system, other modifications of gravity do not have to be and it is worth checking. Our code and implemented techniques can be used with slight modifications for studies of a broader class of theories. Implementing other models of $f(R)$ gravity exhibiting chameleon mechanism should be fairly straightforward and therefore we would like to explore this type of modification in a similar way as we did for the Hu-Sawicki model.

We would like to study the generic $f(R)$ models with negative and positive powers of curvature of **2003PhRvD..68l3512N** which can in principle unify the inflation and cosmic acceleration. The model is given by

$$f(R) = R - \frac{a}{(R - \Lambda_1)^n} + b(R - \Lambda_2)^m. \quad (5.1)$$

Another class of models we would like to explore was proposed by **2007JETPL..86..157S**. This class of modifications is given by

$$f(R) = R + \lambda R_0 \left[\left(1 + \frac{R^2}{R_0^2} \right)^{-n} - 1 \right]. \quad (5.2)$$

All of these models can be studied in dense objects surrounded by a vacuum (or decreasing density) such as stars and halos as we did in this work. Another approach, which can be tested in laboratory conditions on Earth, is quite the opposite. We can study the behavior of the chameleon in a vacuum chamber surrounded by a dense environment. This could be implemented easily in our code and is therefore worth studying. However, we showed that the effective screening potential is very low on scales of galaxies and can range from 10^{-10} up to completely screened values of the order 10^{-40} , depending on the parameter n . For a wide range ($0.1 < n < 1$) we do not expect this will lead to measurable results but for the low values ($n < 0.1$) it could lead to some measurable effects.

The main field for studying modified gravities remains on cosmological scales where it mimics the cosmological constant. In the work, we dealt with approximations which can greatly help to study quasi-linear regimes. Although the non-linear results for used approximation schemes do not look very promising compared to simple particle-mesh codes such as **COLA** they proved that linear approximation can be used successfully and we can still obtain results in mildly non-linear regimes. This can be used for studies

of modified gravity where solving the full non-linear equations is computationally very demanding and probing the huge space of different modifications almost impossible. We showed that linear approximation of chameleon equations can still lead to observable non-linear results.

This approach we want to pursue further, i.e. to use particle-mesh codes such as COLA, HACC, or GADGET without demanding short-range interactions and implement modified equations for theories such as chameleon. To speed up the execution time we would use the linear predictions for these theories which we saw can still lead to non-linear results. This will further push the scales where we can study the chameleon behavior down and it will increase current precision at the BAO scale.

The next step we can make in studying the non-linear regime with modified gravities is to use N -body code with short-range forces, use the linear predictions for chameleon gravity to avoid the lengthy computation of the chameleon field and therefore obtain a good approximation of the background value of the field. To solve the equations on small scales quickly we would use the introduced technique for spherical systems. As the halo finders are a standard part of the simulations, obtaining some approximate density profile of forming halos would not be too expensive. Consequent solving of the one-dimensional chameleon non-linear equations does not pose any substantial demands on computing time.

Conclusion

The thesis was dealing with the topic of modified gravity and how we can discover its resulting deviations from general relativity. In chapter 1 we summarized linear equations for the evolution of the Universe. We described how we can use the evolution process to studies of cosmological parameters of the Universe. We described basic cosmological observables and their usefulness when distinguishing between different cosmologies.

Chapter 2 was focused on modifications of the general relativity. We described successes and failures of the standard cosmological model and presented main issues with the cosmological constant. We described how we can modify the theory of gravity and focused on one of the most studied extensions – the $f(R)$ gravity. We studied the Hu-Sawicki $f(R)$ theory from a different angle of view than most authors – as the chameleon gravity in the Einstein frame. We studied the chameleon behavior numerically and we checked the linear predictions with our numerical solutions. We studied the chameleon behavior in spherical systems (stars, galaxies, clusters) and concluded that the chameleon mechanism hides the fifth force on scales smaller than superclusters for the Hu-Sawicki model and that the chameleon needs to be studied on large cosmological scales through N -body simulations. Our original method of solving modified gravity in spherical systems represents an important contribution because it can be applied to other models than Hu-Sawicki $f(R)$. With these methods we can check the behavior of other theories in spherical systems and also check their behavior in laboratory conditions on the Earth.

In chapter 3 we described general techniques when dealing with cosmological N -body simulations and how we implemented them in our own code for N -body simulations – with both standard and modified gravity. We described our own contribution to the CCL code and how the CCL can help scientists worldwide to speed up their work on cosmology.

In chapter 4 we introduced different approximations that can be used to study the Universe quickly and intuitively. Most of the previous studies focused on the Einstein-de Sitter Universe whereas in this work we generalized the equations to the Λ CDM cosmology. We described how we implemented these approximations in studies of modified gravity which has not been done before and is one of the original result of this work.

Key results of the thesis are presented in chapter 5. We described original results of our cosmological N -body simulations using approximate schemes. We focused on aspects that have drawn less attention in the past – slower growth of structure formation (modified growth function), study of the correlation function, predictions of the shape of the peak of baryonic acoustic oscillations in real space and the ability to predict certain non-linear features of full N -body simulations. We showed that these approximations can be used to study scales around the baryon acoustic oscillation scale, $k \sim 0.1 \text{ } h\text{Mpc}^{-1}$ but not much further. We also tested these methods on the chameleon gravity and showed what probes are suited the best for distinguishing between different parameters of the chameleon gravity. Unlike matter power spectra and baryonic acoustic

oscillation, the halo mass function does not seem to be a good way to study the chameleon gravity. In ?? we then discussed other possible applications of approximate methods described in this work and we outlined further course of our studies.

In ?? we reviewed the present-day and future experiments designed to study our Universe. We showed what constraints on our Universe have already been observed and what accuracy of future experiments we can expect.

Author's publications

In the List of publications all author's publications are listed (in alphabetical order by the authors' last names). The list includes the author's previous work in the Cherenkov Telescope Array collaboration (**2016arXiv161005151C**; **2017arXiv170903483A**; **2017ApJ...840...74A**; **2019scta.book.....C**). While working on the CTA, the author's main interest were the atmospheric simulations of cosmic showers (**2017EPJWC.14401014V**). The purpose of these simulations is to improve the calibration of the atmospheric properties as well as a calibration of the detector response. One of the main contributions to the systematic uncertainties of the CTA measurements stems from the uncertainty on the atmospheric density profile, of molecules and aerosols, which these simulations help to reduce.

The author's work inside the Dark Energy Science Collaboration (DESC) focused mainly on improving the Core Cosmology Library (**2019ascl.soft01003C**; **2019ApJS..242....2C**). Initially, the author helped to create a documentation of the library, wrote many examples of usage of the CCL, and presented with other authors the CCL and its capabilities at several sessions to new users. The author also helped to improve several automatization processes regarding the releasing of the library and helped to improve its compatibility across different operating systems and environments.

The author's main work, *Fast approximate methods for modified gravity cosmological simulations* (**2020MNRAS.493.2085V**), summarizes results regarding the cosmological N -body simulations described in this work (chapter 3 – chapter 5). It is the result of several-year research regarding the cosmological simulations. During this time, the author wrote his own code for cosmological simulations, implemented methods for solving highly non-linear equations, and developed complex pipelines for processing and analyzing data of these simulations.